

# **Quantum transport in hexagonal boron nitride-carbon nanotube heterostructures**

**Inauguraldissertation**

zur  
Erlangung der Würde eines Doktors der Philosophie  
vorgelegt der  
Philosophisch-Naturwissenschaftlichen Fakultät  
der Universität Basel

VON

**Gulibusitan Abulizi  
aus China**

Basel, 2018

Originaldokument gespeichert auf dem Dokumentenserver der Universität Basel  
[edoc.unibas.ch](http://edoc.unibas.ch)

Genehmigt von der Philosophisch-Naturwissenschaftlichen Fakultät  
auf Antrag von

Prof. Dr. Christian Schönenberger  
Prof. Dr. Kasper Grove-Rasmussen  
Dr. Carola Meyer

Basel, 12.12.2017

Prof. Dr. Martin Spiess  
Dekan

# Contents

<b>1. Introduction</b>	<b>1</b>
<b>2. Theoretical background</b>	<b>3</b>
2.1. From graphene to CNTs . . . . .	3
2.2. Hexagonal boron nitride . . . . .	5
2.3. Electrical contacts to CNTs . . . . .	6
2.4. CNT quantum dots . . . . .	6
2.4.1. Quantized energy levels . . . . .	7
2.4.2. Coulomb blockade and single electron tunneling . . . . .	7
2.4.3. Coulomb diamonds . . . . .	9
2.4.4. Double quantum dots . . . . .	11
2.5. CNTs coupled to superconductors . . . . .	12
2.5.1. Superconductivity . . . . .	12
2.5.2. Proximity effect and Andreev reflection . . . . .	14
2.5.3. Crossed Andreev reflection and elastic co-tunneling . . . . .	15
2.5.4. Multiple Andreev reflections . . . . .	16
2.5.5. Andreev bound states . . . . .	17
2.5.6. Josephson effect . . . . .	18
2.5.7. Quasiparticle transport and resonant Andreev tunneling . . . . .	19
<b>3. Devices fabrication and measurement set-up</b>	<b>23</b>
3.1. Standard device fabrication procedure . . . . .	23
3.2. Fabrication of hBN-CNT heterostructures . . . . .	25
3.2.1. hBN substrate for CNT QDs . . . . .	25
3.2.2. hBN capped CNTs with top finger gates . . . . .	27
3.2.3. hBN encapsulated CNTs with 0D side contacts . . . . .	29
3.2.4. hBN tunnel barriers to CNTs . . . . .	32
3.3. Cryogenic measurement set-up . . . . .	35
<b>4. Clean carbon nanotube quantum dots on hexagonal boron nitride</b>	<b>37</b>
4.1. Introduction . . . . .	37
4.2. SEM imaging contrast mechanism . . . . .	37
4.3. Tunneling spectroscopy of a clean CNT QD on hBN . . . . .	40
4.4. Electrical tunability of a dual-gated CNT QD with hBN top gate dielectric	42
4.5. Conclusions . . . . .	45

<b>5. Characterization of carbon nanotube devices with hexagonal boron nitride tunnel barriers</b>	<b>47</b>
5.1. Full characterization of a CNT parallel DQD . . . . .	48
5.1.1. Introduction . . . . .	48
5.1.2. Device and measurement set-up . . . . .	49
5.1.3. Bias spectroscopy and avoided crossings . . . . .	50
5.1.4. Conclusions . . . . .	54
5.2. Towards clean and large scale hBN . . . . .	55
5.2.1. Introduction . . . . .	55
5.2.2. Challenges with hBN film quality and transfer methods . . . . .	56
5.2.3. Integration of monolayer hBN into CNT devices . . . . .	58
5.2.4. Conclusions . . . . .	62
<b>6. Hexagonal boron nitride encapsulated carbon nanotubes with zero-dimensional contacts</b>	<b>63</b>
6.1. Introduction . . . . .	63
6.2. Device structure and measurement set-up . . . . .	64
6.3. Experimental results . . . . .	64
6.3.1. Edge profile and contact material selectivity . . . . .	64
6.3.2. A large single QD . . . . .	66
6.3.3. A large parallel DQD . . . . .	67
6.4. Conclusions . . . . .	68
<b>7. Induced superconductivity in end-contacted carbon nanotubes</b>	<b>69</b>
7.1. Introduction . . . . .	69
7.2. Device structure and measurement set-up . . . . .	69
7.2.1. Characteristics in an intermediate coupling regime . . . . .	70
7.2.2. Characteristics in a strong coupling regime . . . . .	75
7.2.3. Conclusions . . . . .	79
<b>8. Summary and outlook</b>	<b>81</b>
<b>Bibliography</b>	<b>94</b>
<b>A. Fabrication recipes</b>	<b>95</b>
<b>B. Additional data to Chapter 5</b>	<b>99</b>
<b>C. Additional data to Chapter 7</b>	<b>101</b>
<b>Curriculum Vitae</b>	<b>105</b>
<b>Publications</b>	<b>107</b>
<b>Acknowledgements</b>	<b>109</b>

# 1 Introduction

---

Carbon nanotubes (CNTs) are a versatile fundamental building block for classical small scale electronics [1] and quantum electronics [2], and for the investigation of novel quantum states [3]. However, the ideal properties of CNTs are usually masked by electrical potential fluctuations induced by the substrate. In this context, realization of disorder-free and clean CNT devices with outstanding quality is crucial for the fundamental studies of various interesting phenomena, such as Fabry-Perot interference [4, 5], Klein tunneling [6], tunable quantum dots (QDs) [6–8], spin-orbit interactions [9, 10], valley spin-blockade [11], and the formation of Luttinger liquids [12], Wigner crystals [13], and Wigner molecules [14] in one-dimensional (1D) systems.

CNTs grow cleanly with low intrinsic disorders [15], but the standard silicon/silicon dioxide (Si/SiO<sub>2</sub>) wafer substrate supported CNT devices made using conventional technologies, suffer from disorders and contaminations, for instance, induced by the substrate [16] and polymer residues [17, 18]. This forces the electronic system to break into localized and uncontrolled zero-dimensional (0D) QDs at low temperatures [19–21]. If one wants to access the ideal 1D electronic properties of CNTs, it is essential to improve the overall device quality. In this perspective, the CNT research community has developed “clean” or so-called “ultraclean” fabrication schemes, including suspension of CNTs [7, 15, 22], growing CNTs in the last processing step [23], and mechanically transferring CNTs from a growth substrate onto a target substrate by means of stamping techniques [8, 11, 24]. However, each approach comes with certain disadvantages. For example, suspended CNT devices suffer from limitations in the scalability, geometry, and in the choice of the contact and gate materials. It is difficult to find a superconductor or a ferromagnet that is suitable for the growth of CNTs by chemical vapor deposition (CVD) at high temperatures around 1000°C. Stamping techniques [25, 26] are more versatile, but depend strongly on the interface characteristics of the contacts. In contrast, devices on a substrate offer a much larger variety of design options and suitable materials, but the stability and quality of the electronic structures are usually compromised. Standard cleaning techniques, such as dry etching, cannot be deployed because they also remove the carbon structures [27], while the thermal coupling to the substrate is too large for in-situ current annealing.

For graphene, a new approach has recently led to “clean” nanostructures, namely, the use of thin layers of hexagonal boron nitride (hBN) as insulating substrates or gate dielectrics. In comparison to the standard Si/SiO<sub>2</sub> substrate, hBN is a two-dimensional (2D) material that has a great deal of attractive properties [28, 29]. For instance, it is chemically inert and has atomically flat surfaces with less dangling bonds and charge traps, which are ideal for isolating the whole active device structure from its noisy environment. This has allowed the implementation of substrate supported graphene in

high-mobility transistors [30] and enabled the fabrication of highly efficient monolayer tungsten diselenide ( $\text{WSe}_2$ ) light emitting diodes [31]. Using hBN instead of  $\text{SiO}_2$  has led to larger charge puddles in graphene [28] and a reduction of electronic instabilities, e.g., in graphene QDs [29]. Like graphene, hBN can be mechanically cleaved by simple methods [30], resulting in thicknesses down to single atomic layers. To date, significant efforts have been made to fabricate hBN-graphene multi-layer heterostructures [32], 1D contacts to hBN encapsulated graphene [33], and combinations with other layered materials.

In this PhD project, we introduce a new production scheme, where we combine the 2D hBN with quasi-1D CNTs. This new approach aims to improve the device quality significantly, and eventually allow us to explore the electronic transport properties of CNTs in extended 1D geometries. In particular, we investigate hBN as clean substrates for CNT QDs [34], insulators for top finger gates, tunnel barriers to CNTs [35], and to fully encapsulate the CNTs. Our results are very promising first steps in the fabrication of substrate-bound very clean CNT devices. This allows us to explore many advantageous properties [36] of CNTs in more versatile structures than possible in two-terminal devices with “ultra-clean” suspended CNTs.

This thesis is structured as follows. In **Chapter 2**, we introduce the theoretical background of the studied material systems, namely, the CNTs and hBN, with a focus on the basics of the CNT QDs. We discuss the superconductivity phenomena that may occur when a CNT is brought into contact with superconductors. **Chapter 3** describes the fabrication details of hBN-CNT heterostructures and demonstrates the low-temperature measurement set-up. The main results of this thesis are presented in **Chapters 4-7**. We investigate the scanning electron microscopy (SEM) imaging contrast for locating CNTs on hBN flakes in **Chapter 4**. We discuss the low-temperature characteristics of CNT QDs fabricated on hBN flakes and of the dual-gated CNT QD devices with hBN top-gate dielectrics. We demonstrate that very good electrical device quality and stability can be achieved simply by introducing hBN flakes into the system. In **Chapter 5**, we focus on the CNT devices with atomically thin hBN tunnel barriers. We first characterize a CNT parallel double-QD, where we study the avoided crossings observed in its finite bias spectroscopy. In the second part of **Chapter 5**, we turn to the discussion on challenges of integrating atomically thin hBN into a CNT device. In **Chapter 6**, hBN encapsulated CNTs with 0D normal metal side contacts are investigated, while devices with 0D superconducting side contacts are characterized in **Chapter 7**. We demonstrate that low contact resistance with high-yield can be realized with 0D side contacts. This system allows us to study induced superconductivity in hBN encapsulated CNTs, where different transport regimes are identified. In an intermediate coupling regime, we observe Coulomb blockade, quasiparticle transport, resonant Andreev tunneling, and Andreev bound states, while in a strong coupling regime, multiple Andreev reflections and the magnetic field dependence of the critical current are discussed. **Chapter 8** summarizes the experimental results and provides an outlook.

# 2 Theoretical background

---

This chapter provides the theoretical background of our experimental results, which will be discussed in this thesis. In this chapter, we first introduce the material systems, including CNTs and hBN, with a focus on their electronic structures. We then turn to the CNT QDs and their electronic transport properties in both single and double dot configurations. For the CNT devices with superconducting contacts, we introduce the basic concepts of superconductivity. We discuss several transport mechanisms that are involved in the metallic normal metal-superconductor (N-S) nanostructures and further extend our discussions to the superconductor-normal metal-superconductor (S-N-S) junctions. Transport processes that are relevant for the superconductor-quantum dot-superconductor (S-QD-S) structures are presented at the end of the chapter.

## 2.1. From graphene to CNTs

Graphene refers to a single layer of graphite, in which the carbon atoms are arranged in a 2D honeycomb structure with a lattice constant of  $a \approx 1.42 \text{ \AA}$  [37]. In graphene, each carbon atom is  $sp^2$  hybridized and forms three  $\sigma$  bonds within a plane and one weakly localized  $\pi$  bond in the  $p_z$  orbital, which is oriented out of the plane. As shown in Fig. 2.1(a), the primitive unit cell consists of two inequivalent carbon atoms A and B, with primitive lattice vectors  $\mathbf{a}_1$  and  $\mathbf{a}_2$ . In Fig. 2.1(b), the reciprocal lattice vectors  $\mathbf{b}_1$  and  $\mathbf{b}_2$  are given by the condition  $\mathbf{a}_i \cdot \mathbf{b}_j = 2\pi\delta_{ij}$ . The electronic band structure is obtained by applying a tight binding model considering only the nearest-neighbor hopping [37, 38]. In Fig. 2.1(c), we show the band structure of graphene, where the conduction and valence bands meet at six corner points of the Brillouin zone. These points are known as the charge-neutrality or Dirac points and can be divided into two sets of three points that are not equivalent and labeled as  $K$  and  $K'$ . The dispersion relation close to a Dirac point is given by

$$E(q) = \pm \hbar v_F |q|, \quad (2.1)$$

with  $q = k - K$  or  $q = k - K'$  being a 2D vector and  $v_F \approx 8.1 \times 10^5 \text{ m/s}$  being the Fermi velocity [36, 38]. Graphene is known as a zero-gap semiconductor or a semi-metal with zero density of states at the Fermi level. The high symmetry points,  $K$  and  $K'$ , give rise to a new degree of freedom called valley or iso-spin [38].

CNTs are quasi-1D materials, which are also made entirely out of carbon atoms [36]. In general, there are two types of CNTs: single- and multi-walled CNTs. The single-walled CNT can be seen as a single sheet of graphene rolled up into a hollow cylinder with a diameter of typically 1 – 2 nm. A multi-walled CNT consists of concentric

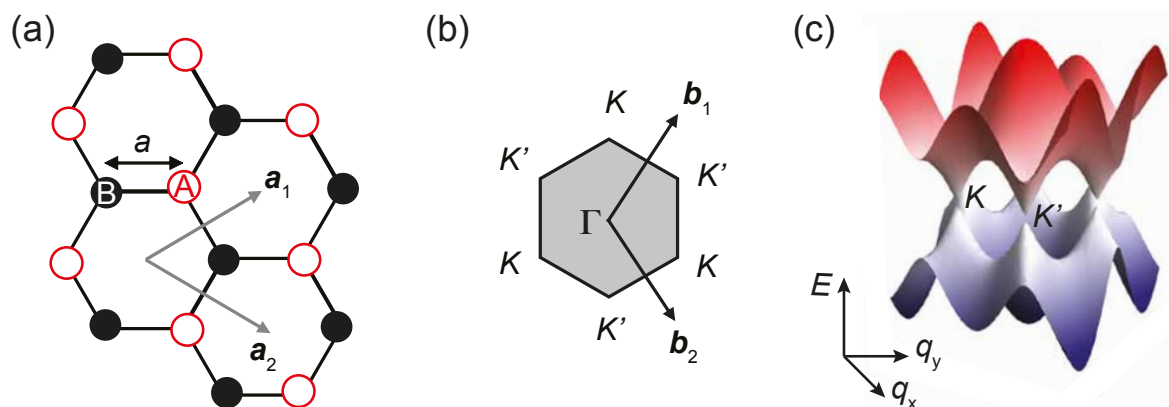


**Figure 2.1.** (a) Honeycomb lattice structure of graphene in a real space. The primitive unit cell consists of A and B atoms, with primitive lattice vectors,  $\mathbf{a}_1$  and  $\mathbf{a}_2$ . (b) The first Brillouin zone of graphene with high symmetric points,  $K$  and  $K'$ , at six corners. The reciprocal lattice vectors,  $\mathbf{b}_1$  and  $\mathbf{b}_2$ , are given by the condition  $\mathbf{a}_i \cdot \mathbf{b}_j = 2\pi\delta_{ij}$ . (c) The electronic band structure of graphene calculated from tight binding model. The energy dispersion is linear close to the points,  $K$  and  $K'$ . Images are adapted from Ref.[38].

hollow cylinders with a diameter of 10 – 20 nm and an interlayer spacing of typically 3.4 Å [39]. The electronic band structure of a single-walled CNT can be calculated by applying a so-called zone folding approximation, where an additional periodic boundary condition is introduced to the electronic wave function of graphene [36, 40]. In this approximation, the parallel component of momentum,  $k_{\parallel}$ , along the tube axis is unaffected, but the component along the circumference direction,  $k_{\perp}$ , is quantized and can only change in steps given by  $\Delta k_{\perp}\pi d = 2\pi$ , with  $d$  being the CNT diameter. This leads to 1D sub-bands with energies given by

$$E^l(k_{\parallel}) = \pm\hbar v_{\text{F}}\sqrt{(k_{\parallel})^2 + (k_{\perp}^l)^2}, \quad (2.2)$$

where  $l$  denotes the sub-band with quantized momentum component,  $k_{\perp}^l = k_{\perp}^0 + l\Delta k_{\perp}$ . Owing to the small diameter of a CNT, the excitation energy of a CNT is typically in eV range. Thereby, even at room temperature, only the lowest sub-band is occupied. It turns out that CNTs can be classified into one of these categories: they are either metallic or semiconducting. As shown in Fig. 2.2(a), if the lowest sub-band cuts through the Dirac point, i.e.,  $k_{\perp}^0 = 0$ , the linear dispersion relation with zero band gap is preserved, and the CNT is metallic. If  $k_{\perp}^0 \neq 0$ , and the lowest sub-band misses the Dirac point with an energy band gap of  $E_g = 2\hbar v_{\text{F}}k_{\perp}^0$ , the CNT is classified as semiconducting, as illustrated in Fig. 2.2(b). The origin of these either metallic or semiconducting character can be understood from the explicit formulation of the periodic boundary conditions [40]. We introduce a chiral vector,  $\mathbf{C} = n\mathbf{a}_1 + m\mathbf{a}_2$ . It describes the direction along which the CNT is rolled up, i.e.,  $|\mathbf{C}| = \pi d$ . The periodic boundary conditions are expressed with the chiral vector as

$$\psi(\mathbf{r} + \mathbf{C}) = e^{i\mathbf{C}(\mathbf{k}+\mathbf{K})}\psi(\mathbf{r}) = \psi(\mathbf{r}), \quad (2.3)$$



where  $\mathbf{C} \cdot \mathbf{K} = 0$ , only if  $(n - m) = 3l$ , with  $l$  being an integer number. With this condition, the CNT is classified as metallic. However, if  $(n - m) = 3l + 1$ , the lowest sub-band misses the Dirac point by  $\Delta k_{\perp}^0 = 2/3d$ . This leads to an energy band gap of  $E_g = 2\hbar v_F k_{\perp}^0 = 4\hbar v_F/3d \approx 0.7 \text{ eV}/d [\text{nm}]$ , thereby resulting in a semiconducting CNT.

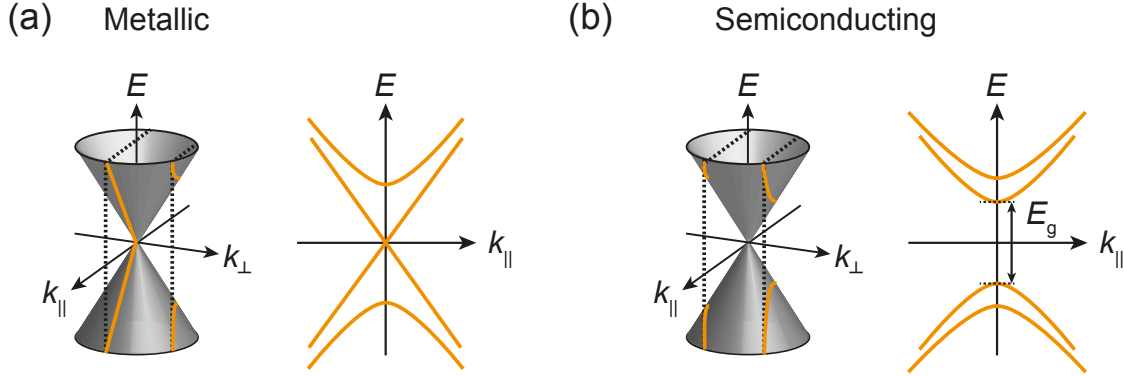


**Figure 2.2.** (a) Quantization of  $k_{\perp}$  along the circumference direction leads to the 1D sub-bands. If  $k_{\perp}^0 = 0$ , the lowest sub-band cuts through the Dirac point, and the CNT is metallic with linear dispersion relation. (b) If  $k_{\perp}^0 \neq 0$ , the lowest sub-band misses the Dirac point with an energy band gap of  $E_g$ , thereby resulting in semiconducting CNTs. Images are adapted from Ref.[36].

## 2.2. Hexagonal boron nitride

As a 2D layered material, hBN has an hexagonal lattice structure that is very similar to graphite [41]. Thereby, hBN is sometimes referred as “white graphite” [42]. A single layer of hBN is a structure analogue of a graphene sheet, where the carbon atoms at the A and B points are replaced by the boron and nitrogen atoms, respectively. The intralayer interaction in hBN is governed by the strong covalent bonds, but the interlayer binding is relatively weak with no directional bonds and generally dominated by weak van der Waals forces [43]. Thanks to the strong directional ionic bonding between neighboring atoms with an in plane hexagonal form, hBN is expected to be inert and free of dangling bonds or surface charge traps. In addition, hBN has an atomically smooth surface. For instance, the surface roughness of graphene on an hBN is three times lower than that of the graphene on a  $\text{SiO}_2$  [44]. In a 2D bulk form, hBN is known as an insulator with a large band gap energy of  $\sim 6 \text{ eV}$  [45] and considered as an excellent gate dielectric with a dielectric constant of 3 – 4 and breakdown fields of  $\sim 0.8 \text{ V/nm}$ , which are comparable to that of the  $\text{SiO}_2$  dielectric [46]. Besides, hBN has relatively high in plane thermal conductivity, which makes them an ideal material for enhancing the lateral heat spreading, when it is used as a dielectric support for the CNT- and graphene-based electronic devices [47, 48].

Similar to graphene, hBN with different number of layers can be obtained via a micro-mechanical peeling process that is well-known as the “scotch tape” method [49]. In parallel, atomically thin and large scale hBN films have been synthesized by CVD on

a variety of substrates, including Cu and Fe foils [50, 51]. The CVD growth condition of hBN on Cu is similar to that of graphene. Due to the similarity in the growth conditions, direct integration of hBN into graphene electronic devices with minimized transfer steps and contaminations has been possible, thereby enabling in-plane heterostructures with complex geometries and high qualities [52].

### 2.3. Electrical contacts to CNTs

Electrical contacts to CNTs is generally realized by lithography, which includes the optical and electron-beam lithographies. For a highly transparent contact and a perfect CNT, one expects a two-terminal resistance of  $h/4e^2$ , with the factor 4 corresponding to the four conductance channels resulting from the spin and valley degeneracies. However, in practice, the two-terminal resistance of a device is usually associated with a value that is much higher than the expected one. This discrepancy can be either due to formation of tunnel barriers at the CNT-metal interfaces or due to diffusive scattering events occurred especially in highly disordered CNTs [53]. Besides, lithography processes may leave resist residues and contaminations at the interfaces, thereby resulting in a higher two-terminal resistance. Schottky barriers may form at the CNT-metal interfaces, if semiconducting CNTs are considered [54]. Within the Schottky-Mott picture [55], Schottky barriers for both electrons and holes injections can arise, if the Fermi level lies in the middle of the CNT band gap. An ohmic contact to the valence band is expected, if the Fermi level is aligned below the CNT band gap, thereby leading to a p-type device behavior. The Schottky-Mott rule demonstrates that metals associated with high and low work function result in CNT devices with p-type and n-type characteristics, respectively, as confirmed by studies on different contact materials [54, 56]. Furthermore, the Schottky-Mott rule predicts that the contact resistance scales with the inverse diameter of the tube because of a diameter-dependent band gap, i.e.,  $E_g \sim 1/d$ , which has also been experimentally observed [57]. However, the Schottky-Mott picture does not apply to certain contact materials, for instance, platinum (Pt) and aluminum (Al) [58, 59]. To understand the deviations, one has to take into account other factors that are equivalently important. These include the wetting properties of the contact materials [60], the nature of chemical bonds formed at the CNT-metal interfaces [61], as well as the influence of the ambient environment on the metal work function [62]. As pointed out in Ref. [54], a conclusive understanding of the nature of the CNT-metal contacts has not evolved yet.

### 2.4. CNT quantum dots

At room temperature, the electronic mean free path of a CNT is determined by the electron-phonon scattering. However, at low temperatures, it is governed by the elastic scattering events [53]. For instance, at temperatures below  $\sim 50$  K, the electronic mean free path of a semiconducting CNT can reach up to a few  $\mu\text{m}$  long, and in a metallic CNT, it can be as long as  $10 \mu\text{m}$  [53]. Since our measurements are carried out at cryogenic temperatures on CNT segments, which are on the order of few hundred

nanometers long, we consider these CNTs as 1D ballistic conductors. At cryogenic temperatures, the electronic transport in these ballistic CNTs is dominated by quantum mechanical effects, e.g. electron tunneling through Schottky barriers. In this case, depending on the strength of the tunnel coupling between the CNT and the metallic leads, a variety of quantum mechanical phenomena may arise. In particular, if the CNT couples strongly to the metal leads, Fabry-Perot interference patterns can be observed in the transport spectroscopy [4, 7]. In contrast, if the coupling is weak, closed QDs may form in the CNT segment, thereby resulting in Coulomb blockade (CB) and single electron tunneling [7, 34, 63].

### 2.4.1. Quantized energy levels

A QD is a small object that has confinement in all three spacial dimensions. The electronic wave function along the circumference of a CNT is confined to a box-like state as a result of its small diameter that is on the order of few nanometers. However, a CNT QD can only be realized by introducing a confinement along the nanotube axis. In practice, such a confinement is achieved by depositing metal contacts onto the CNT. At room temperature, electrons or holes often acquire sufficient thermal energies to overcome the potential barriers formed at the CNT-metal interfaces, thereby entering or leaving the CNT. However, at low temperatures, this transport process is dominated by tunneling events, where an isolated QD forms as the tunneling resistance of the CNT-metal contact barriers is on the order of the resistance quantum, i.e.,  $R \geq h/e^2$ . Such a system can be treated as a particle-in-a-box problem [36, 64], and the momentum component along the tube axis needs to fulfill the boundary conditions of standing wave solutions expressed as

$$k_{\parallel} = \frac{n\pi}{L}, \quad (2.4)$$

where  $n = 1, 2, 3, \dots$  is a positive integer, and  $L$  corresponds to the confinement size. By introducing a confinement along the tube axis, the energy of the system is quantized, thereby giving rise to discrete energy levels with a mean level spacing of

$$\delta E = \frac{\hbar v_F}{2L}, \quad (2.5)$$

with  $\hbar$  being the plank constant and  $v_F$  being the Fermi velocity. This expression is derived for ideal metallic CNTs. However, for semiconducting CNTs, this expression holds only for the energy levels that are far away from the band gap of the CNT.

### 2.4.2. Coulomb blockade and single electron tunneling

At low temperatures, if the QD confinement size is small enough, removing or adding an electron (or a hole) from or into the dot can lead to a significant change in its electrostatic energy as a result of electron-electron interactions. This phenomenon is well-understood within the constant-interaction model [65], where a single constant capacitance,  $C$ , is assigned to the dot, and it is independent of the electronic states of the system. Let us consider a typical device set-up, which consists of a single QD with three terminals, as depicted in Fig. 2.3(a). Charge carriers can tunnel between the

source (S) and the drain (D) contacts through the QD. These two terminals, S and D, are connected to the dot via tunnel coupling with coupling strengths of  $\Gamma_S$  and  $\Gamma_D$ , and capacitive coupling with capacitances of  $C_S$  and  $C_D$ , respectively. A finite bias voltage,  $V_{SD} = V_S - V_D$ , is applied to measure the differential conductance,  $G = \delta I / \delta V_{SD}$ . In Fig. 2.3(a), the third terminal is capacitively coupled to the dot with a capacitance of  $C_{BG}$ , and it is used as a back-gate (BG) to tune the electrostatic potential of the dot by applying a voltage of  $V_{BG}$ . The capacitive coupling of the QD to these three terminals leads to a total capacitance,  $C = C_S + C_D + C_{BG}$ . The total ground state energy of the dot with  $N$  charge carriers is given by

$$E_{\text{tot}}(N) = \frac{1}{2C}[-|e|(N - N_0) + C_S V_S + C_D V_D + C_{BG} V_{BG}]^2 + \sum_{n=1}^N E_n, \quad (2.6)$$

with  $N_0$  being the number of electrons inside the dot at  $V_{SD} = 0$  V and  $V_{BG} = 0$  V. In this formula, the first term refers to the electrostatic energy of the system, and the last term corresponds to the sum over the occupied energy levels. The number of charge carriers,  $N$ , in the dot varies in discrete steps, but the voltage induced charges, i.e.,  $C_S V_S$ ,  $C_D V_D$ , and  $C_{BG} V_{BG}$ , are tuned continuously. At  $V_{SD} \approx 0$ , only the ground state transitions take place, and the electrochemical potential energy of the dot is defined as  $\mu(N) = E_{\text{tot}}(N) - E_{\text{tot}}(N - 1)$ . This corresponds to the energy required for adding the  $N^{\text{th}}$  charge carrier to the dot and is given by

$$\mu(N) = E_N + \frac{e^2}{C}[N - N_0 - \frac{1}{2}] - \frac{|e|}{C} C_{BG} V_{BG}. \quad (2.7)$$

This expression describes a ladder of electrochemical potential levels, as illustrated in Fig. 2.3(b). The spacing between the levels is given by the addition energy of

$$E_{\text{add}} = \mu(N + 1) - \mu(N) = \frac{e^2}{C} + \delta E, \quad (2.8)$$

where  $E_C = e^2/C$  is known as the charging energy, and  $\delta E$  corresponds to the quantized energy level spacing of the dot. This formula suggests that if we assume a level degeneracy of four for an ideal CNT by taking into account both spin and valley degeneracies, the energy cost for adding the first electron to an orbital shell is  $E_C + \delta E$ , while it only requires the charging energy,  $E_C$ , to add the second, third and fourth charge carriers.

Adding or removing the charge carriers is realized by changing  $V_{BG}$ , which tunes the electrochemical potential levels of the dot linearly, with a lever arm of  $\alpha = C_{BG}/C$ . This means that the electrochemical potential levels shifts up or down linearly with decreasing or increasing  $V_{BG}$ , respectively. When the electrochemical potentials of the dot are aligned with those of S and D, i.e.,  $\mu_{QD} = \mu_S = \mu_D$ , charge movement between S and D through the dot takes place, and the QD is on resonance. In other situations, the charge transport through the dot is not allowed, and the system stays in a CB state. If one measures  $G$  as a function of  $V_G$ , one obtains a series of Coulomb peaks, as shown in Fig. 2.3(b). In this figure, each Coulomb peak refers to a situation, where the QD is on resonance.

So far, we have treated the QD as an isolated object by assuming that the broadening of an energy level due to tunnel coupling is always smaller than any relevant energy

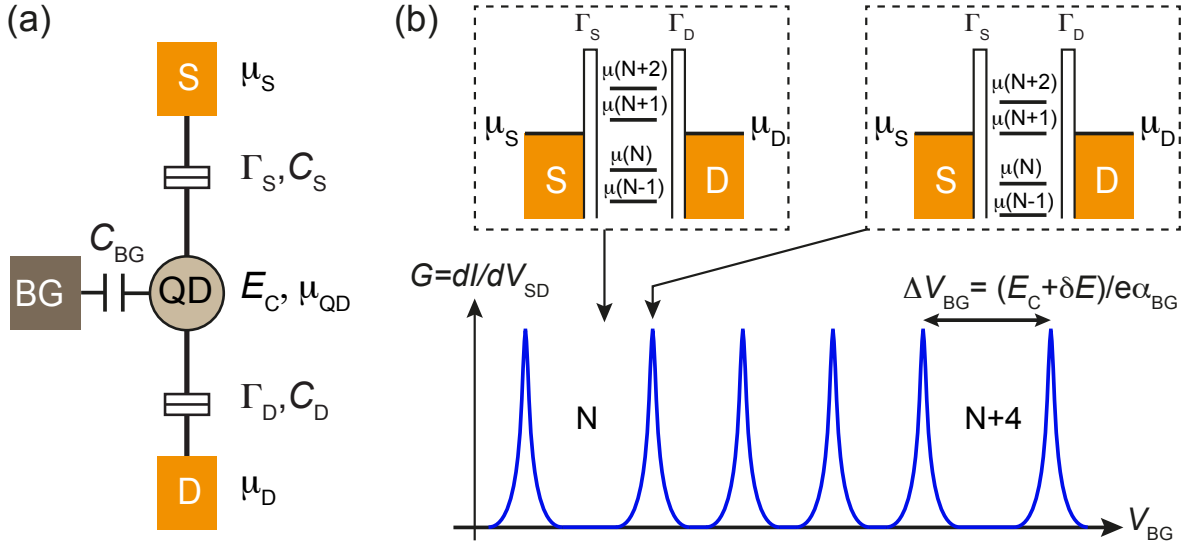


**Figure 2.3.** (a) Capacitive model of a QD connected to the source (S) and drain (D) electrodes via both tunnel ( $\Gamma_S$  and  $\Gamma_D$ ) and capacitive ( $C_S$  and  $C_D$ ) couplings. The BG electrode is capacitively coupled to the QD with a capacitance of  $C_{\text{BG}}$  to tune the electrochemical potential of the dot. (b)  $G$  as a function of  $V_{\text{BG}}$  at  $V_{\text{SD}} = 0$  for an ideal CNT QD with a four-fold pattern. Insets show the corresponding energy diagrams for the situations, where the QD is in CB and on resonance, respectively. Images are adapted from Ref.[66].

scales of the system under consideration, i.e.,  $\Gamma \ll k_B T \ll \delta E, E_C$ . In this so-called thermally broadened (or weak coupling) transport regime, the line shape of a Coulomb peak is given by [67]

$$G(\Delta E) = \frac{e^2}{h} \frac{1}{4k_B T} \frac{\Gamma_S \Gamma_D}{\Gamma_S + \Gamma_D} \frac{1}{\cosh^2[(\Delta E/2k_B T)]}, \quad (2.9)$$

where  $\Delta E = -e\alpha_{\text{BG}}(\Delta V_{\text{BG}} - V_{\text{BG}}^{(0)})$  with  $V_{\text{BG}}^{(0)}$  referring to the position of the resonance. This expression suggests that with increasing the temperature, the Coulomb peak amplitude maximum decays with  $1/k_B T$ , and its full width at half maximum (FWHM) broadens linearly with  $\sim 4k_B T$ .

In contrast, if the system is in a strong coupling (or lifetime broadened) regime, i.e.,  $k_B T \ll \Gamma \ll \delta E, E_C$ , the line shape of a Coulomb peak at  $T = 0$  K is given by the well-known Breit-Wigner formula [67]

$$G(\Delta E) = \frac{e^2}{h} \frac{\Gamma_S \Gamma_D}{\Gamma_S + \Gamma_D} \frac{\Gamma}{\Delta E^2 + (\Gamma/2)^2}, \quad (2.10)$$

where  $\Gamma = \Gamma_S + \Gamma_D$  is equivalent to the FWHM of the Coulomb peak. The asymmetry between  $\Gamma_S$  and  $\Gamma_D$  determines the Coulomb peak amplitude maximum.

### 2.4.3. Coulomb diamonds

In addition to  $V_{\text{BG}}$ , one can also apply  $V_{\text{SD}}$  to lift the CB, as schematically illustrated in Fig. 2.4. The drain is usually kept at ground, i.e.,  $\mu_D = 0$ , while  $V_{\text{SD}}$  is applied to S, i.e.,

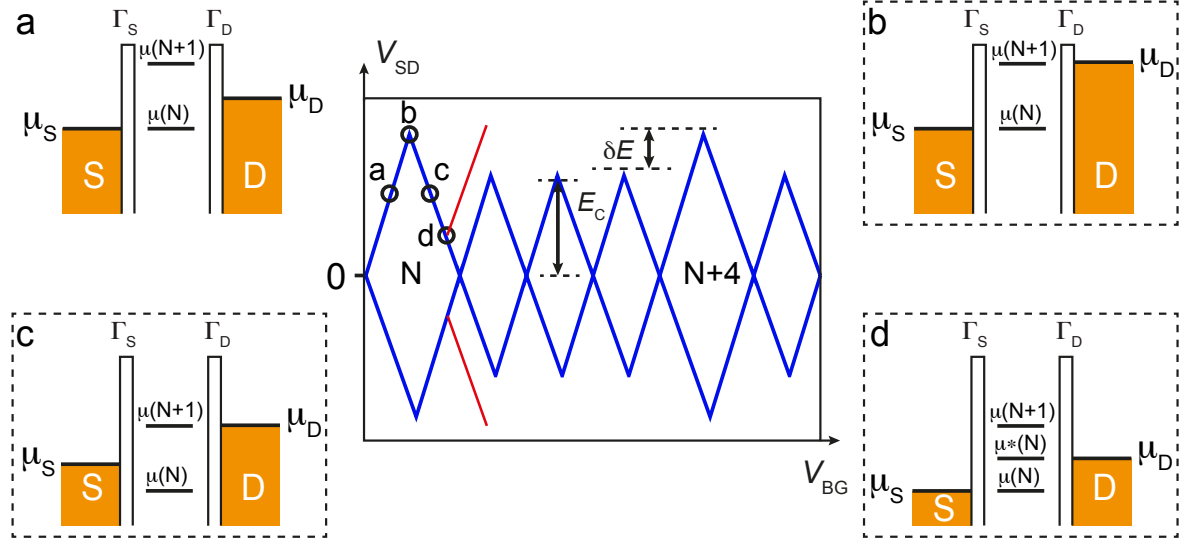


**Figure 2.4.** Charge stability diagram of an ideal CNT QD. The energy diagrams shown in black dashed rectangles correspond to the different biasing conditions marked by the black circles in the charge stability diagram. Situation d represents the charge transport through the first excited state. Images are adapted from Ref. [66].

$\mu_S = -|e|V_{SD}$ . As shown in Fig. 2.4, whenever the electrochemical potential level of the dot lies within the bias window, charge carriers can tunnel from one lead into the other through the QD level. By measuring  $G$  as a function of  $V_{SD}$  and  $V_{BG}$ , CB diamond [65] is obtained. In Fig. 2.4, we show the charge stability diagram of a QD formed in an ideal CNT, with a four-fold shell filling characteristic. Inside the diamonds, the number of charge carriers is fixed, and the system stays in CB states. However, outside of the diamonds, there is at least one QD level within the bias window, which lifts the CB. Along the diamond edges with positive (situation a in Fig. 2.4) and negative (situation c in Fig. 2.4) slopes, the dot level remains aligned with  $\mu_S$  and  $\mu_D$ , respectively. Since the change of the dot level is linear with respect to the applied voltages, one can calculate the slopes of the diamond edges. To stay along the diamond edges with a negative slope, the shift of the dot level induced by S has to be compensated by the gate voltage  $\Delta V_{BG}$ , i.e.,  $0 = -|e|\frac{C_{BG}}{C}\Delta V_{BG} - |e|\frac{C_S}{C}\Delta V_{SD}$ , thereby resulting in a negative slope of  $s_- = -\frac{C_{BG}}{C_S}$ . Similarly, for the positive slope, one obtains  $-|e|\Delta V_{SD} = -|e|\frac{C_{BG}}{C}\Delta V_{BG} - |e|\frac{C_S}{C}\Delta V_{SD}$ , which leads to a positive slope of  $s_+ = \frac{C_{BG}}{C - C_S}$ . The lever arm of BG can now be determined as  $\alpha_{BG} = \frac{s_+|s_-|}{s_+ + |s_-|} = \frac{C_G}{C}$ . This means that the positive and negative slopes of the diamond edges allow us to estimate  $\alpha$ ,  $C_S$ ,  $C_D$ , and  $C_{BG}$ . In addition, at the tip of the diamond, the diamond edges with negative and positive slopes cross, and this corresponds to a situation, where both  $\mu_S$  and  $\mu_D$  are aligned with the dot levels (situation b in Fig. 2.4). Thereby,  $V_{SD}$  refers to the spacing between the two dot levels, which is equivalent to  $E_{add}$ . For a Coulomb diamond pattern with four-fold shell filling structure, as shown in Fig. 2.4, the addition energy,  $E_{add} = E_C + \delta E$ , is associated with the size of the large diamond, and the size of the small diamonds corresponds to the charging energy,  $E_C$ .

As discussed above, at a small bias, only the ground state transitions between

$E_{\text{tot}}(N-1)$  and  $E_{\text{tot}}(N)$  take place. However, at a large source-drain bias of  $|eV_{\text{SD}}| > |\delta E|$ , the first excited state of the dot with energy,  $E_{N+1}$ , enters the bias window and allows the charge transport through the excited state [66]. This means that the  $N^{\text{th}}$  charge carrier can be excited into the first excited state,  $E_{N+1}$ , of the dot and then relax back into the ground state,  $E_N$ . The onset of this transition leads to an additional line, which is running parallel to the diamond edges and terminates at  $|eV_{\text{SD}}| < |\delta E|$ , as indicated by the solid red lines (situation d) in Fig. 2.4. In addition, there is possibilities to observe higher order tunneling processes with increasing the tunnel coupling strength,  $\Gamma = \Gamma_S + \Gamma_D$ . In a second order process, which is known as the elastic co-tunneling event [68], a charge carrier can enter the dot and a second charge carrier leaves the dot within the uncertainty time scale of  $\sim \hbar/E_C$ , thereby giving rise to a constant differential conductance,  $G \propto \Gamma_S \Gamma_D / E_C^2$ . As  $V_{\text{SD}}$  exceeds the energy level spacing,  $\delta E$ , the inelastic co-tunneling process [68] starts to appear and leads to a conductance step.

#### 2.4.4. Double quantum dots

We now extend the system from single dots to more than one dot. While single dots are often referred to artificial atoms, the coupled multiple dots can be described as artificial molecules. In this section, we discuss double QDs (DQDs) that are placed next to each other in series with both tunnel and capacitive couplings to the respective electrodes, as depicted in Fig. 6.4(a). For this system, two back-gates,  $V_{\text{BG1}}$  and  $V_{\text{BG2}}$ , are introduced to tune the electrochemical potentials of QD1 and QD2, respectively. For simplicity, we only discuss the charge stability diagram for the linear regime, where  $V_{\text{SD}}$  is considered to be infinitively small, and we assume  $\mu_{\text{S,D}} = 0$  at  $V_{\text{SD}} = 0$  V.

When the two individual QDs are fully decoupled, the charge stability diagram reveals perfectly vertical and horizontal lines. Analogous to a single dot, each line corresponds to the situation, where the number of charge carriers in the ground state changes by one. If the bias window is small enough, current flow is only possible at the crossing points, where the electrochemical potentials of both dots are aligned. However, in a realistic system, due to the presence of finite cross capacitances,  $V_{\text{BG1}}$  is capacitively coupled to the electrochemical potential of QD2 and vice versa. In addition, because of the interdot capacitance,  $C_t$ , the electrochemical potential of one dot is influenced by the change in occupancy of the other dot. As a result, for such a system, the charge stability diagram turns into a regular honeycomb pattern with two different slopes, which form the edges of the honeycomb [69], as schematically depicted in Fig. 6.4(b). Inside the honeycomb, the number of charge carriers is fixed. Each crossing point splits into triple points, where three different charge, states  $(n, m)$ ,  $(n, m+1)$ , and  $(n+1, m)$ , are energetically degenerate. The interdot capacitance,  $C_t$ , determines the distance between each set of triple points, while the spacing between the edges of the honeycomb indicates the strength of the cross capacitances.

If we now consider a finite tunnel coupling,  $\Gamma_t$  between the two individual dots, the triple points in the charge stability diagram further develop into avoided crossings, as shown inside the black dashed rectangle in Fig. 6.4(b). The interdot tunnel coupling allows the charge carriers to leave one dot and enter the other. At triple points, where the energy levels of both dots are aligned, the electronic states of these two individual dots hybridize and form the bonding and anti-bonding molecular orbitals, thereby

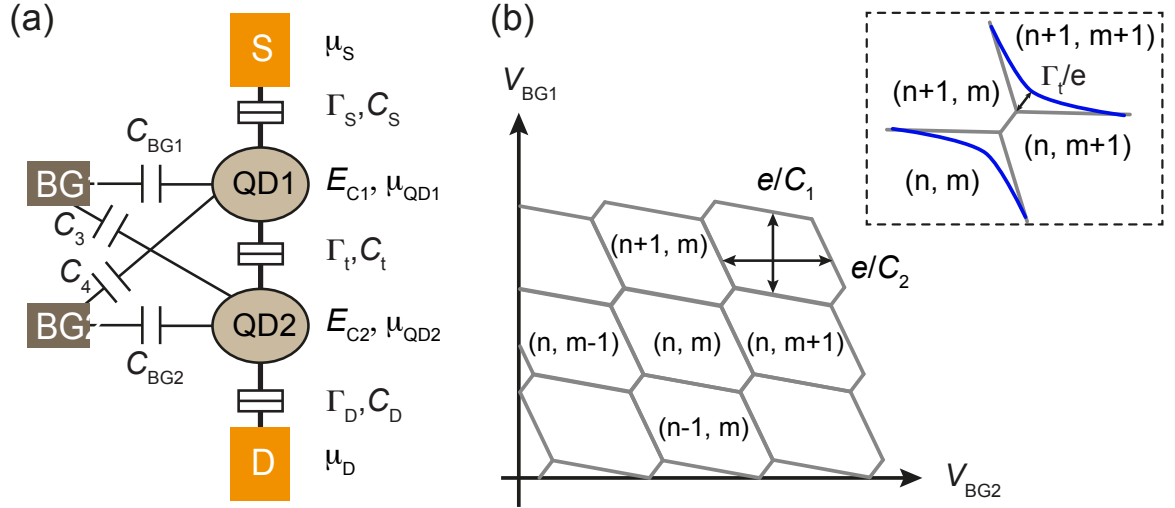


**Figure 2.5.** (a) Typical device set-up of a coupled DQD in series. (b) Charge stability diagram shows honeycomb pattern. The numbers,  $(n, m)$ , indicate the charge carrier occupation of QD2 and QD1. Inset shows a zoom-in view of the honeycomb structure for the cases of large (blue) and small coupling (gray) strengths.

leading to avoided crossing features. The interdot tunnel coupling strength governs the separation of the avoided crossing from the triple points. If  $\Gamma_t$  is very large, the honeycomb pattern of the charge stability diagram evolves into parallel lines, corresponding to a large dot tuned by both gates.

## 2.5. CNTs coupled to superconductors

### 2.5.1. Superconductivity

Two significant characteristics of a superconductor are the zero electrical resistance and the perfect diamagnetism. In 1911, Onnes discovered that some metals, for example, mercury and lead, display vanishing electrical resistance, when the measurement temperature is lower than a critical value,  $T_C$  [70]. Two decades later, Meissner and Oschensfeld demonstrated that an external magnetic field is expelled from a superconductor, as it enters the zero resistance state [71], and leaves no magnetic field in the interior of the superconductor. This indicates that a superconductor appears to be perfectly diamagnetic. There exists a critical magnetic field,  $B_C = \mu_0 H_C$ , above which the zero resistance state of the superconductor breaks down, because an energy cost is required for keeping the magnetic field out of the interior of the superconductor. In fact, the analysis by London and London [72] suggests that the magnetic field is not completely expelled but exists within a penetration depth of  $\sim 10^{-6}$  cm at the surface of the superconductor. A superconductor, with little or no magnetic field within it, stays in the Meissner state. There are two types of superconductors, i.e., Type I and Type II. The superconductivity of a Type I superconductor breaks down, if the external magnetic field is larger than a critical value,  $H_C$ . In contrast, a Type II superconductor starts to lose the superconductivity at a critical field,  $H_{C1}$ . However, a complete



breakdown of the superconductivity occurs at a higher critical field,  $H_{C2}$ .

A conceptual and mathematical foundation for conventional superconductivity was developed by Bardeen, Cooper, and Schrieffer [73], and it is known as the BCS theory. This theory relies on a fundamental theorem proposed by Cooper [74]. It states that a pair of electrons, which interact above the Fermi sea with a net attraction between the electrons, can form a bound state called Cooper pair despite the fact that their total energy is larger than zero [74]. This attractive interaction may arise owing to the virtual exchange of phonons and the screened Coulomb repulsion between electrons. One can visualize this Cooper pair attraction by imagining an electron moving within a material. Because of the Coulomb attraction between the electron and the positively charged ion cores in the material, a moving electron causes a lattice distortion of the cores of ions, thereby leaving a net positive charge in the vicinity, which in turn attracts a second electron. Here, a “paired” electron is the one with opposite momentum and spin, which is attracted to this force. It has been demonstrated by Cooper that the binding energy of the electron pair is a very sensitive function of the total momentum,  $K = k_1 + k_2$ , with  $k_1$  and  $k_2$  being the wave vectors of the paired electrons [74]. The binding energy is a maximum, when  $K = 0$ , and it decays very rapidly to zero otherwise. Cooper argued that an elementary excitation of the pair might lead to the splitting of the pair rather than increasing the kinetic energy of the pair. This suggests that the two electrons of a Cooper pair are entangled and have opposite momenta, i.e.,  $k_1 = -k_2$ , indicating a symmetric orbital wave function. However, the Pauli exclusion principle requires an asymmetry of the total wave function with respect to exchanging the two electrons. One has to take into account the spin singlet state,  $|S\rangle = \frac{1}{\sqrt{2}}(|\uparrow\downarrow\rangle - |\downarrow\uparrow\rangle)$ , and multiply it with the orbital part of the wave function to restore the asymmetry of the total wave function. Here, the spin singlet state is expressed with a Dirac notation. Thereby, a Cooper pair can be described as  $(k \uparrow, -k \downarrow)$ . We note that the two individual spins of a Cooper pair are in superposition and fully entangled.

A key conclusion of the BCS theory is that as long as there are net attractive interactions, the Fermi sea becomes unstable below a certain temperature,  $T_C$ . As a consequence, the condensation of Cooper pairs into a boson-like state continues until an equilibrium state is achieved. The BCS theory gives an approximation for this quantum-mechanical many-body state of the system, thereby its ground state becomes accessible to a mathematical treatment. It further demonstrates that an excitation from the ground state requires a minimum energy of  $2\Delta$ , which corresponds to the energy needed to break the Cooper pair. Here, the energy gap,  $\Delta$ , refers to the ordering parameter of the superconductor. Excitations in a superconductor take place at a finite temperature or a large bias, which create unpaired charge carriers called quasiparticles. The dispersion relation for these quasiparticles is given by

$$E(k) = \sqrt{\Delta^2 + \epsilon(k)^2} \quad (2.11)$$

with  $\epsilon(k) = \hbar^2 k^2 / 2m - E_F$  being the kinetic energy of a free electron with respect to the Fermi energy. This dispersion relation has an electron like branch,  $\epsilon > 0$ , and a hole like branch,  $\epsilon < 0$ ). In analogy to the semiconductor band diagrams, one can plot the energies of the quasiparticles as shown in Fig. 2.6(a). The quasiparticles can be seen as superpositions of electrons and holes. Far above the  $E_F$ , the quasiparticles are mostly

electron-like, but deep inside the Fermi sea, they are mostly hole-like. This suggests that for quasiparticles with large kinetic energies, i.e.,  $\epsilon \gg \Delta$ , the behavior of free electrons (or free holes) is recovered. The quasiparticle states are restricted to a narrow energy interval near the  $E_F$ . The density of states (DOS),  $g_S(E)$ , of the quasiparticles can be obtained according to  $g_S(E)dE = g_N(\epsilon)d\epsilon$ :

$$g_S(E) = g_N(\epsilon) \frac{d\epsilon}{dE} = \begin{cases} g_N(\epsilon) \frac{|E|}{\sqrt{E^2 - \Delta^2}}, & |E| \geq \Delta \\ 0, & |E| < \Delta \end{cases} \quad (2.12)$$

where one assumes a constant normal metal DOS, i.e.,  $g_N(\epsilon) \approx g_N(0)$ , which is within a few meV around the  $E_F$ . In Fig. 2.6(b), we show the quasiparticle DOS normalized to  $g_N(0)$ . One clearly see that for large energies,  $|E| \gg \Delta$ , the normal metal DOS is restored, but for  $|E| < \Delta$ , the DOS is zero and suggests that no quasiparticle state is available. When the energy gets close to  $\Delta$ , the DOS of the quasiparticle states starts to diverge. The BCS theory predicts that the energy gap of a superconductor scales with the temperature as  $\Delta(T) \approx \Delta(0)\sqrt{1 - T/T_C}$ . In this formula, the quantity,  $\Delta(0)$ , refers to the energy gap size at  $T = 0$ . For BCS superconductors with weak electron-phonon coupling, one can assume  $\Delta(0) \approx 1.74k_B T_C$ . Another important parameter in the BCS theory is the superconducting coherence length,  $\xi_0 = \hbar v_F / \pi \Delta$  [75]. This parameter is interpreted as the spatial extent of a Cooper pair and related to the characteristic Cooper pair size in the weak coupling BCS theory. A typical value for  $\xi_0$  varies from a few tens to a few hundred nanometers, suggesting a high degree of wave function overlap of the Cooper pairs in their ground states.

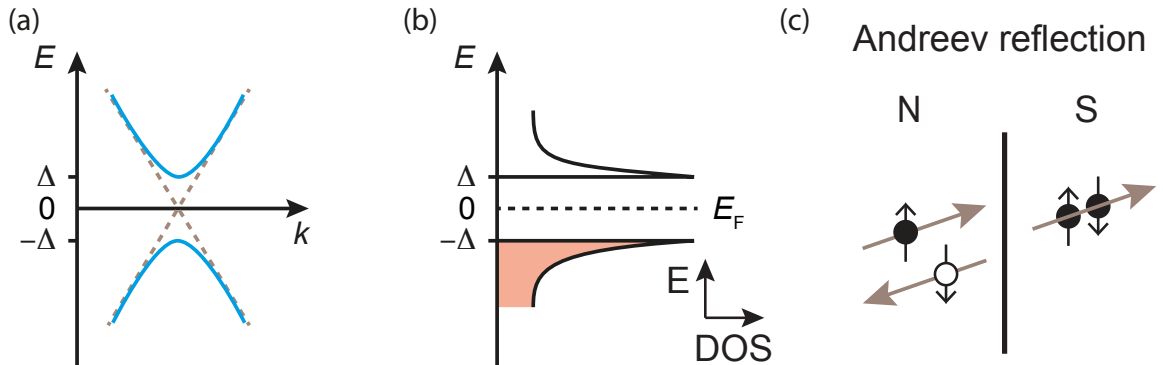


**Figure 2.6.** (a) Quasiparticle dispersion relation (solid blue lines) in comparison with the electron energy in the normal state (dashed gray lines) near Fermi energy. (b) Normalized quasiparticle DOS as a function of energy, sketched in a semiconductor band diagram fashion. (c) Schematic illustration of Andreev reflection of an electron at a normal metal-superconductor (N-S) interface.

### 2.5.2. Proximity effect and Andreev reflection

The proximity effect refers to the observation of superconducting-like behaviors in non-superconducting materials, when they are placed in electrical contact with superconductors [76]. The Andreev reflection plays a central role for the proximity effect, because it

offers a microscopic mechanism for the phenomena occurred at the interfaces between the normal metals (N) and superconductors (S) [77]. The Andreev reflection is a two-electron process, which can be described as follow. If we assume an electron with a sub-gap energy,  $|E| < \Delta$ , impinges on a fully transparent N-S interface, it is forbidden to transfer this incoming electron into the superconductor. This is because there is no quasiparticle states available for occupation due to the energy gap,  $\Delta$ , at  $E_F$  in the DOS of the superconductor. The N-S interface neither can simply reflect the incoming electron back into the normal metal, because it requires a moment transfer of  $\sim 2p_F$ . The N-S interface can only offer a maximum moment of  $\delta p = (dp/dE)_{p_F} \delta E = \Delta/\hbar v_F$ , which is orders of magnitude smaller than the required value. This means that the incoming electron can only be transferred into the superconductor, if one considers a second order process, i.e., the Andreev reflection. In this process, an incoming electron with energy,  $E$  and  $|k, \downarrow\rangle$ , can pair up with a second electron with energy,  $-E$  and  $| -k, \uparrow\rangle$ , to form a Cooper pair into the superconductor, as illustrated in Fig. 2.6(c). The corresponding time-reversal process is the reflection of a hole as an electron, and a Cooper pair leaks into the normal metal. For electrons or holes incident at  $E_F$ , the Andreev reflection is treated as a perfect retro-reflection. The transparency of the N-S interface has a significant influence on the Andreev reflection [78]. The Andreev reflection governs the sub-gap conductance at the N-S interface, by transferring two electrons from a normal metal into the superconductor to form a Cooper pair, or vice versa. For a clean N-S interface, one finds a sub-gap conductance that is twice the normal state conductance, thanks to the two-electron transfer during the Andreev process.

The most important feature of the proximity effect is the phase coherence of the Andreev process. In other words, the two electrons from a Cooper pair leaking can diffuse in phase for a certain time over a certain distance in the normal metal, thereby giving rise to a finite probability for them to form a Cooper pair into the superconductor. As pointed out in Ref.[76], an actual proximity effect is a result of an interplay between the Andreev reflection at the N-S interface and the long-range phase coherence in the normal metal.

### 2.5.3. Crossed Andreev reflection and elastic co-tunneling

We now consider a multi-terminal structure, where a superconductor S is connected to two spatially separated normal metal leads, N1 and N2, as depicted in Fig. 2.7(a). The spacing,  $d$ , between N1 and N2, is considered to be much smaller than the superconducting coherence length,  $\xi_0$ , i.e.,  $d \ll \xi_0$ . Since the Cooper pairs have a spatial extent on the order of  $\xi_0$ , there is a finite probability for an electron in N1 (or N2) to couple with an electron in N2 (or N1) and form a Cooper pair into S. The second electron leaves a reflected hole in N2 (or N1). This non-local Andreev reflection process is known as crossed Andreev reflection, and it corresponds to the splitting of a Cooper pair from a superconductor into two spatially separated normal metal leads [79], as shown in Fig. 2.7(a)(left). The time-reversal process refers to the non-local creation of a Cooper pair into a superconductor.

We note that the crossed Andreev reflection generally competes with another process, which is known as elastic co-tunneling. As pointed out in Ref.[80], the amplitude probability of the elastic co-tunneling process is approximately similar to that of the crossed

Andreev reflection. The elastic co-tunneling refers to a process, where an electron or a hole with a sub-gap energy has a finite probability to coherently tunnel from N1 (or N2) to N2 (or N1) by penetrating through S as a virtual quasiparticle, as depicted in Fig. 2.7(a)(right). This process is treated as a non-local normal reflection. In contrast, if  $d \gg \xi_0$ , the probability for an electron or a hole to coherently tunnel through S reduces to zero and leads to a suppression of the elastic co-tunneling event.

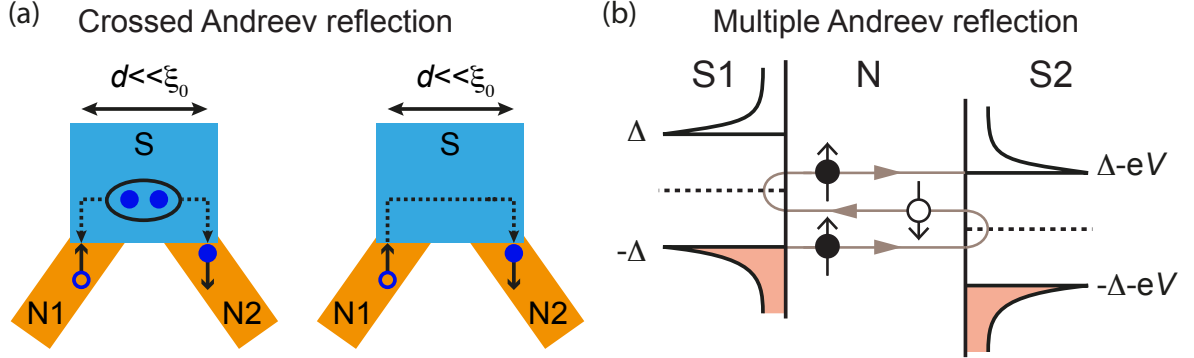


**Figure 2.7.** (a) Schematic illustration of the crossed Andreev reflection (left) and the elastic co-tunneling process (right). Images are adapted from Ref.[81]. (b) Illustration of the multiple Andreev reflection via successive Andreev reflections at both N-S1 and N-S2 interfaces. A quasiparticle is transferred from S1 to S2.

### 2.5.4. Multiple Andreev reflections

When two superconductors are connected by a “weak link”, e.g. a normal metal, the current voltage characteristic of the junction reveals interesting features, such as the subharmonic gap structures and the Josephson current. Some of these subharmonic gap structures are mediated by the multiple Andreev reflections [82–84]. In order to explain the multiple Andreev reflection, we recall the mechanism of the Andreev reflection at an N-S interface. We consider two identical superconductors, S1 and S2, which are connected to a normal metal, N, as schematically illustrated in Fig. 2.7(b). We assume that both N-S1 and N-S2 interfaces are fully transparent, and we ignore the Andreev reflection probabilities outside the superconducting gap. A small bias,  $eV < 2\Delta$ , is applied to shift the electrochemical potential of S1 with respect to that of S2. For simplicity, we consider only one electron incident from the left with an energy,  $-\Delta < E < -\Delta - eV$ . After the first Andreev reflection at the N-S2 interface, this incident electron is converted into a hole and travels to the left, which in turn Andreev reflected at the N-S1 interface and converted back into an electron moving to the right. Successive Andreev reflections at both N-S1 and N-S2 interfaces lead to a progressive rise of the charge carrier energy. This process continues until the charge carrier energy exceeds the superconducting gap energy. As a result, Cooper pairs are transferred from S1 into S2, which induces a supercurrent flow across the junction. At the same time, quasiparticles are transferred from S1 into S2, and this gives rise to the sub-gap conductance peaks in the current voltage characteristics at bias voltages,  $V = 2\Delta/ne$ , with  $n = 1, 2, 3, \dots$  corresponding to the number of Cooper pairs transferred across the junction.

The Andreev reflection as a phase coherent process allows the two electrons from a Cooper pair leaking maintain their phase correlation over a distance of the coherence length,  $\xi_E = \sqrt{\hbar D/2E}$ , where  $D$  corresponds to the diffusion constant of the normal metal [85, 86]. In a short junction limit, i.e.,  $L \ll \xi = \sqrt{\hbar D/\Delta}$ , the coherent proximity regions induced by both N-S1 and N-S2 interfaces overlap and induce a proximity gap in the electron spectrum of the normal metal, which is on the order of the superconducting energy gap. As a result, the phase coherence covers the entire normal region, and the multiple Andreev reflections are fully coherent [86, 87]. In contrast, in a long diffusive S-N-S junction with a small proximity gap that is of the order of the Thouless energy,  $\epsilon_T = \hbar D/L^2 \ll \Delta$ , one expects to observe incoherent multiple Andreev reflections [85]. The sub-gap conductance peaks are predicted to occur at bias voltages given by  $V = 2(\Delta \pm \epsilon_T)/ne$  [88]. We note that for an intermediate regime, i.e.,  $\xi < L < L_\phi$ , with  $L_\phi$  being the phase coherence, the interplay between the proximity effect and the multiple Andreev reflections takes place.

### 2.5.5. Andreev bound states

We now consider a situation, where an electronic excitation, let it be an electron or a hole, is traveling in the normal metal, N, from the left to the right, as schematically depicted in Fig. 2.8(a). After successive Andreev reflections at both N-S1 and N-S2 interfaces, a Cooper pair is transferred from one superconductor into the other, thereby leading to a supercurrent flow across the junction. If the total phase acquired within a full cycle is a multiple of  $2\pi$ , a standing wave pattern forms between S1 and S2, which is referred as an Andreev bound state. In the limit of a short junction, i.e.,  $L \ll \xi$ , one can neglect the dynamical phase, and the total phase acquired in a full cycle is given by [89]

$$\Delta\phi_1 = -\phi + 2\arccos(E/\Delta). \quad (2.13)$$

For the opposite process, where an electron is Andreev reflected and converted into a hole at the N-S1 interface, the total phase acquired in a full cycle yields

$$\Delta\phi_2 = \phi + 2\arccos(E/\Delta). \quad (2.14)$$

Considering the condition  $\Delta\phi_{1,2} = 2n\pi$  for a bound state, with  $n = 0, 1, 2, \dots$ , one can get the Andreev bound state energies for the left- and right-moving supercurrent as

$$E_{\pm} = \pm\Delta\cos(\phi/2). \quad (2.15)$$

We have only considered clean N-S interfaces, and the transmission probability is treated as  $\tau = 1$ . If one takes into account scattering events that take places at the N-S interfaces, the Andreev bound state energy is then given by

$$E_{\pm} = \pm\Delta\sqrt{1 - \tau\sin^2(\phi/2)}. \quad (2.16)$$

In Fig. 2.8(b), we plot the Andreev bound state energy as a function of  $\phi$  for different values of  $\tau$ . Apparently, for  $\tau \sim 0$ , the Andreev bound states lie close to the edges of the superconducting gap. In a mesoscopic system, these discrete Andreev bound states, which can carry a supercurrent, are responsible for the proximity-induced superconductivity [90].

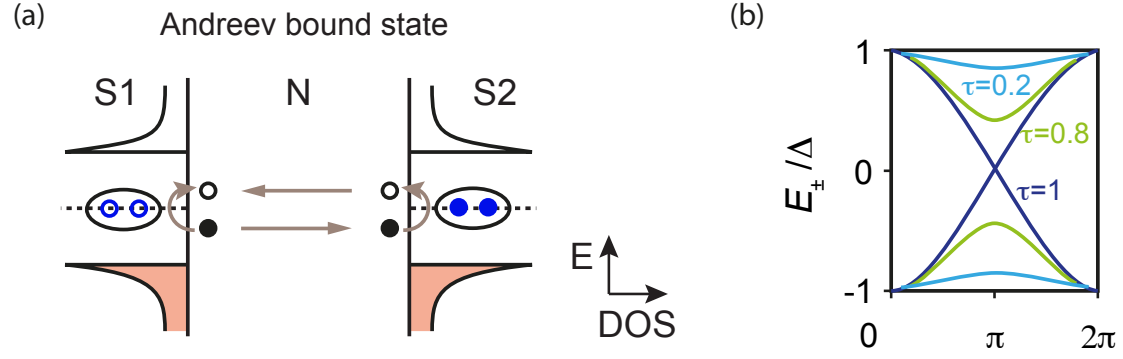


**Figure 2.8.** (a) Illustration of an Andreev bound state formed from constructive interference of multiple Andreev reflections at both N-S1 and N-S2 interfaces. (b) Sketch of the Andreev bound state energies for three different transmission probabilities. Figures are adapted from Ref.[89].

### 2.5.6. Josephson effect

Josephson effect occurs in a system, where two superconductors are placed in a weak contact, such that only the Cooper pair tunneling across the junction is allowed, and this leads to a so-called supercurrent [91]. To introduce the Josephson effect and to calculate the magnitude of the supercurrent, we follow the treatment presented in Ref. [89]. We consider two superconductors, S1 and S2, with ordering parameters,  $\psi_1 = \sqrt{n_1}e^{i\varphi_1}$  and  $\psi_2 = \sqrt{n_2}e^{i\varphi_2}$ , respectively. We assume that S1 and S2 are placed in contact with a coupling between them, and we introduce a potential difference,  $qV = U_1 - U_2$ , with  $q$  being the charge of the current carriers. The zero of energy is considered to be sitting halfway between  $U_1$  and  $U_2$ . In this case, the ordering parameters are related by

$$i\hbar\frac{\partial\psi_1}{\partial t} = \frac{qV}{2}\psi_1 - K\psi_2 \quad (2.17)$$

$$i\hbar\frac{\partial\psi_2}{\partial t} = \frac{qV}{2}\psi_2 - K\psi_1, \quad (2.18)$$

with  $K$  being a constant, which depends on the properties of the junction. If one expresses  $\psi_i$  in terms of  $n_i$  and  $\varphi_i$ , and then multiplies Eq. 2.17 by  $e^{-i\varphi_1}$  and Eq. 2.18 by  $e^{-i\varphi_2}$ , one can obtain the real and the imaginary parts of these equations. The real part reads

$$\frac{dn_1}{dt} = -\frac{2K}{\hbar}\sqrt{n_1n_2}\sin(\varphi) \quad (2.19)$$

$$\frac{dn_2}{dt} = \frac{2K}{\hbar}\sqrt{n_1n_2}\sin(\varphi), \quad (2.20)$$

with  $\varphi = \varphi_1 - \varphi_2$ . The imaginary part yields

$$\frac{d\varphi_1}{dt} = -\frac{qV}{2\hbar} + \frac{K}{\hbar}\sqrt{\frac{n_2}{n_1}}\cos(\varphi) \quad (2.21)$$

$$\frac{d\varphi_2}{dt} = \frac{qV}{2\hbar} + \frac{K}{\hbar}\sqrt{\frac{n_1}{n_2}}\cos(\varphi). \quad (2.22)$$

The supercurrent can be evaluated from the real part using  $I = -qA\frac{dn_1}{dt}$ , and this gives

$$I = I_C \sin(\varphi_2 - \varphi_1), \quad (2.23)$$

with  $I_C = 2qAK\sqrt{n_1 n_2}/\hbar$  being the critical current of the junction. If we assume  $n_1 \approx n_2$  and consider  $q = 2e$  for a Cooper pair, we get the phase difference from the difference of the imaginary part, which yields

$$\frac{d\varphi}{dt} = \frac{d}{dt}(\varphi_2 - \varphi_1) = \frac{qV}{\hbar} = \frac{2eV}{\hbar}. \quad (2.24)$$

We note that Eq. 2.23 and 2.24 refer to the DC and AC Josephson effects, respectively.

In our case, a CNT segment constitutes the “weak link”, which can lead to several transport regimes. So far, we have only focused on a regime, where the tunnel coupling strength between the CNT segment and the superconducting leads is the largest relevant energy, i.e.,  $\Gamma \gg \Delta, E_C$ . In this strong coupling regime, the CB effect is neglected, and the system is treated as an S-N-S junction. In the following section, we discuss the other extreme limit, i.e.,  $\Gamma \ll \Delta, E_C$ , where the CB effect results in the formation of QDs in the system, such that the Andreev processes are strongly suppressed, and only the quasiparticle tunneling processes are allowed. At the end of the section, we introduce the intermediate regime, i.e.,  $\Gamma \sim \Delta \ll E_C$ , where the resonant Andreev tunneling processes can occur.

### 2.5.7. Quasiparticle transport and resonant Andreev tunneling

We consider an S-QD-S structure, which consists a single QD formed between two superconductors, S1 and S2. A schematic illustration of the structure is shown in Fig. 2.9(a). The QD is characterized by  $E_C$ ,  $\delta E$ , and  $\mu_{\text{QD}}$ . We assume that a bias voltage is applied between S1 and S2, with S2 kept at the ground potential. A gate voltage,  $V_{\text{BG}}$ , is applied to tune the  $\mu_{\text{QD}}$  of the dot. In this figure,  $\Gamma = \Gamma_{\text{S1}} + \Gamma_{\text{S2}}$  is the total tunnel coupling strength,  $C_{\text{tot}} = C_{\text{S1}} + C_{\text{S2}} + C_{\text{BG}}$  is the total capacitance of the system,  $\Delta$  is the superconducting energy gap, and  $\mu_{\text{S1}}$  and  $\mu_{\text{S2}}$  are the electrochemical potentials of S1 and S2, respectively. We set  $\Gamma_{\text{S1}} = \Gamma_{\text{S2}} \ll \Delta < \delta E \ll E_C$ , so that the Andreev processes are strongly suppressed, and the transport is dominated by the Coulomb repulsion, which only allows the quasiparticle tunneling [92, 93].

In Fig. 2.9(b), we qualitatively sketch the expected charge stability diagram for the S-QD-S junction. In this figure, the solid red lines trace the boundaries of the CB diamonds, and the tips of the diamonds correspond to the onset of the quasiparticle tunneling. In the case of an N-QD-N junction, the diamond boundaries cross at  $V_{\text{SD}} = 0$ , thereby giving rise to zero-bias conductance peaks at the charge degeneracy points. However, compared to the N-QD-N junction, the impact of  $\Delta$  manifests itself in the diamond structure, such that the tips of the diamonds are separated in bias by  $4\Delta/e$ . The tips of the diamonds may shift horizontally in  $V_{\text{BG}}$  with respect to each other because of the capacitive coupling of the superconducting leads to the dot. A microscopic model for an S-QD-S junction is provided in Ref.[93], where the DC current is given by the resonant-tunneling-like expression [93, 95]

$$I(V) = \frac{e}{\hbar} \int dE g_{\text{S1}}(E + eV) g_{\text{S2}}(E) \cdot T_{\text{QD}}(E) \cdot [f_{\text{S1}}(E + eV) + f_{\text{S2}}(E)], \quad (2.25)$$

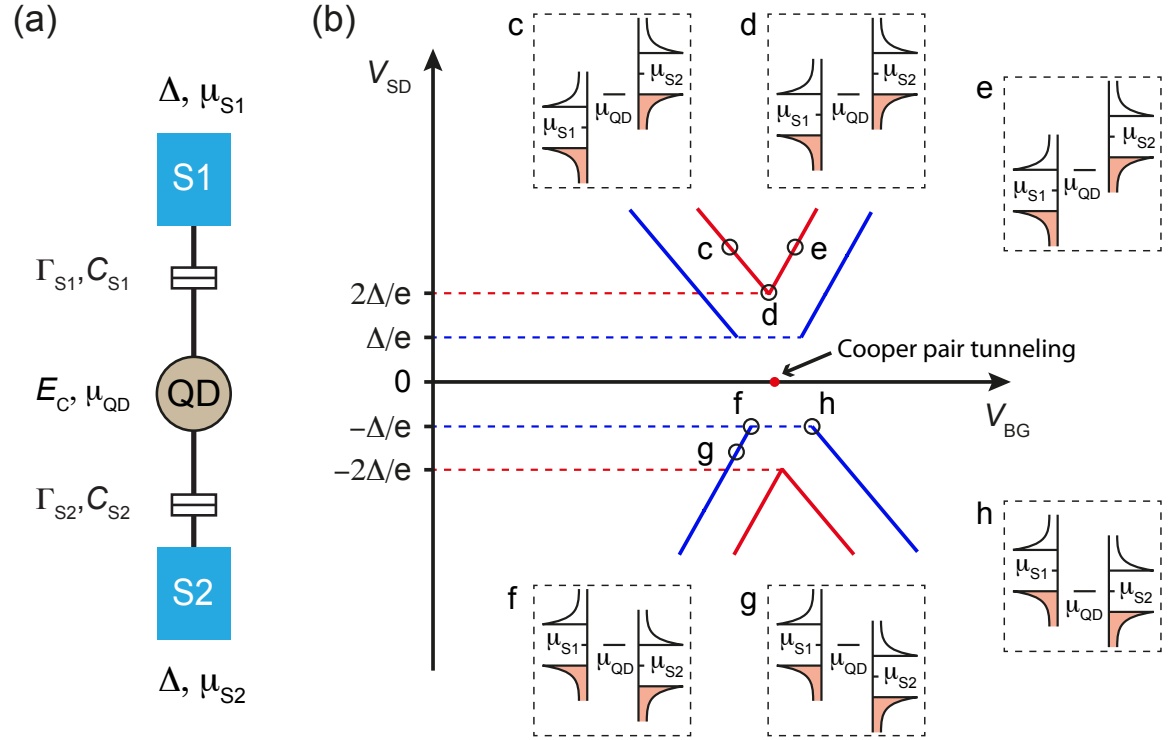


**Figure 2.9.** (a) Schematic illustration of an S-QD-S junction, where a QD is coupled to the superconducting leads, S1 and S2. (b) Charge stability diagram (solid red lines), which is expected for the junction in the quasiparticle tunneling limit. The solid blue lines correspond to the resonant Andreev tunneling. Energy diagrams in the black dashed rectangles show the alignment of the electrochemical potentials of  $\mu_{\text{S1}}$ ,  $\mu_{\text{QD}}$ , and  $\mu_{\text{S2}}$  for the selected positions in the charge stability diagram. Images are adapted from Ref.[94].

with  $g_{\text{S1}}(E + eV)$  and  $g_{\text{S2}}(E)$  being the quasiparticle DOS in S1 and S2, respectively. Here,  $f_{\text{S1,2}} = 1/[\exp(E/k_{\text{B}}T) + 1]$  corresponds to the Fermi distribution function in the respective superconducting leads. For sufficiently low temperatures, i.e.,  $k_{\text{B}}T \ll \Gamma$ , we treat the line shape of the dot resonance with the Breit-Wigner transmission function, as described by Ep. 2.10.

We now turn to the intermediate regime, i.e.,  $\Gamma \sim \Delta < \delta E, E_C$ . In this limit, the Andreev reflections are possible, despite the large  $E_C$ , which suppresses a double occupation of the dot level [93]. We consider that the QD is still weakly coupled to the superconducting leads, and the dot capacitance is small enough to preserve the CB effect. In this case, one expects to observe the resonant Andreev tunneling, as indicated by the solid blue lines in Fig. 2.9(b). To identify the resonant Andreev tunneling, we focus on the charge stability diagram, which is shown in Fig. 2.9(b). At zero bias, a single spin-degenerate resonant level of the dot is aligned with the electrochemical potentials of both superconducting leads, i.e.,  $\mu_{\text{QD}} = \mu_{\text{S1}} = \mu_{\text{S2}}$ , and coherent tunneling of Cooper pairs, as pointed out by the red dot in Fig. 2.9(b), can take place either through the Andreev bound states or through the resonant Andreev tunneling, thereby



leading to a peak in  $G$ . However, at a finite bias, the resonant Andreev tunneling process turns on, when the system fulfills any of the following conditions:  $\mu_{S1} = \mu_{QD} = \mu_{S2} - \Delta$  (point f in Fig. 2.9(b)),  $\mu_{S1} = \mu_{QD} = \mu_{S2} + \Delta$ ,  $\mu_{S1} + \Delta = \mu_{QD} = \mu_{S2}$ , and  $\mu_{S1} - \Delta = \mu_{QD} = \mu_{S2}$  (point h in Fig. 2.9(b)). These conditions correspond to the cases, where Cooper pairs are either created in or removed from the superconducting leads. Moreover, the resonant Andreev tunneling has both  $V_{BG}$  and  $V_{SD}$  dependence, which is traced as the solid blue lines in Fig. 2.9(b). As two electrons need to tunnel coherently through a single energy level of the dot, the resulting resonant Andreev tunneling refers to a 4<sup>th</sup> order process. In the limit of non-interacting electrons and  $k_B T \ll \Gamma$ , the resonance has a predicted line shape given by [96]

$$G(\Delta E) = \frac{2e^2}{h} \left( \frac{2\Gamma_{S1}\Gamma_{S2}}{\Gamma_{S1}^2 + \Gamma_{S2}^2 + 4\Delta E^2} \right)^2, \quad (2.26)$$

where  $\Delta E = -e\alpha_{BG}(\Delta V_{BG} - V_{BG}^{(0)})$  with the position of the resonance,  $V_{BG}^{(0)}$ . This predicted line shape has been experimentally measured in Ref.[97]. If we assume a symmetric tunnel coupling to the superconducting leads, i.e.,  $\Gamma_{S1} = \Gamma_{S2}$ , compared to the Lorentzian line shape expressed by Ep. 2.10, one expects that the amplitude of the Andreev tunneling decays much faster, when it is off resonance, thereby offering a signature for distinguish them from the CB resonances [96].



# 3 Devices fabrication and measurement set-up

---

In this chapter, we present the fabrication details of our CNT nanostructures made using hBN flakes of different thickness either as clean substrates, gate insulators, tunnel barriers, or to encapsulate the CNTs. The main text of this chapter is dedicated to describe the fabrication processes and to highlight the crucial steps, while the employed standard recipes are given in [Appendix A](#). At the end of the chapter, we briefly demonstrate the cryogenic measurement set-up used for characterizing the electronic transport properties of our CNT-based devices at low temperatures.

## 3.1. Standard device fabrication procedure

We first illustrate the fabrication scheme of our conventional CNT devices on a standard Si/SiO<sub>2</sub> wafer substrate. The substrate is exposed to a high temperature of  $\sim 950^\circ\text{C}$  during the CVD growth of CNTs and the electrical contacts are fabricated on top.

### Substrate preparation

Four different substrates are involved for the device fabrication. Detailed substrate characteristics can be found in [Appendix A](#). Despite the differences in their characteristics, all substrates are first cut into small pieces of  $1 \times 1 \text{ cm}^2$  size and then immersed and sonicated in acetone and isopropyl alcohol (IPA) at  $40^\circ\text{C}$  for 15 min in each solvent. Afterwards, 30 min of ultraviolet-ozone surface treatment is carried out to remove the solvent residues. At this stage, the substrates are ready for fabricating devices on them.

### CNT growth

We adopt the CVD technique to grow CNTs using iron-based catalyst particles in an oven at a high temperature [98, 99]. Both the iron molybdenum (Mo/Fe) and the iron ruthenium (Ru/Fe) catalysts [100] are used, and the growth process starts with sonicating the catalyst solution in a high power for 4 h to break the aggregated particles into homogeneously dispersed nanoparticles. The catalyst solution is immediately spin-coated onto a clean Si/SiO<sub>2</sub> substrate, which is then placed in the middle of a CVD oven. The oven is heated up to the growth temperature of  $\sim 950^\circ\text{C}$  for the Mo/Fe catalyst and  $\sim 850^\circ\text{C}$  for the Ru/Fe catalyst under a constant argon/hydrogen (Ar/H<sub>2</sub>) flow. The growth is carried out in argon and methane for 10 min. Afterwards, the oven is cooled to  $\sim 250^\circ\text{C}$  under a constant Ar/H<sub>2</sub> flow, and the sample is taken out from the oven and stored in vacuum at the end.

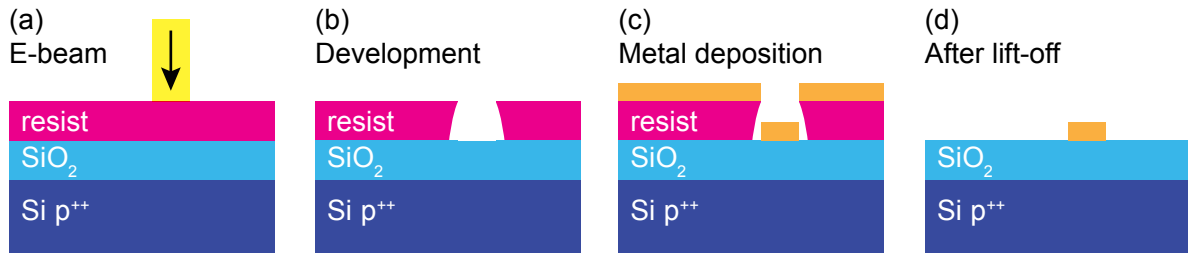


**Figure 3.1.** A schematic illustration of a standard EBL. (a) The resist layer is exposed to an electron-beam to pattern the desired structure. (b) After development, a patterned resist mask remains. (c) Metal deposition. (d) After lift-off, the desired metal structure remains on the substrate.

### Alignment markers

After growing the CNTs, we pattern the substrate with alignment markers by standard electron-beam lithography (EBL) [101], as illustrated in Fig. 3.1. The alignment markers serve as a coordinate system for locating the CNTs. The EBL process starts with spin-coating a layer of 300 nm thick electron-beam resist onto the substrate and then baking at 180°C for 3 min to evaporate the remaining solvents and to harden the resist. We use a high resolution positive electron-beam resist [102], ZEP 520A (ZEP) or polymethylmethacrylate (PMMA) with a molecular weight of 950K. The resist layer is exposed to a highly focused electron-beam (e-beam) to pattern it with a desired structure, see Fig. 3.1(a). This e-beam exposure breaks the long polymer chains of the resist into short segments. Thereby, a chemical developer, n-amyl acetate for ZEP or a 1:3 mixture solution of methyl isobutyl ketone (MIBK) and IPA or PMMA, selectively dissolves the light-weighted short polymer segments, and leave the remaining resist as a mask for the metal deposition, see Fig. 3.1(b). Right after the development process, we place the sample in an electron-beam evaporator to deposit 5 nm thick titanium (Ti) as an adhesion layer and 45 nm thick gold (Au) on top, as shown in Fig. 3.1(c). The lift-off process is carried out in n-methyl-2-pyrrolidone (NMP) at 70°C for ZEP or in acetone at 50°C for PMMA to dissolve the resist and to leave the desired metal structure on the substrate, see Fig. 3.1(d). One can assist the lift-off process by a turbulent flow created with a syringe or a pipette.

### CNT localization and electrical contacts

We use SEM to take images of the CNTs with respect to the alignment markers. We obtain an optimal SEM imaging contrast for individual CNTs by using the in-lens detector with an acceleration voltage of  $\sim 0.6$  keV and 30  $\mu\text{m}$  aperture. We select the CNTs that appear less visible and straight with a length of  $\sim 2$   $\mu\text{m}$  long. At this stage, we cannot distinguish between the single-walled and multi-walled, metallic and semiconducting, and disordered and defect-free CNTs.

We follow the standard EBL to fabricate electrical contacts on top of the CNTs. The four alignment markers shown in Fig. 3.2(a) are placed 10  $\mu\text{m}$  away from each other, and we achieve 100 nm alignment precision. We note that if a device fabrication involves more than one type of contact materials, several EBL steps are required. In some cases,

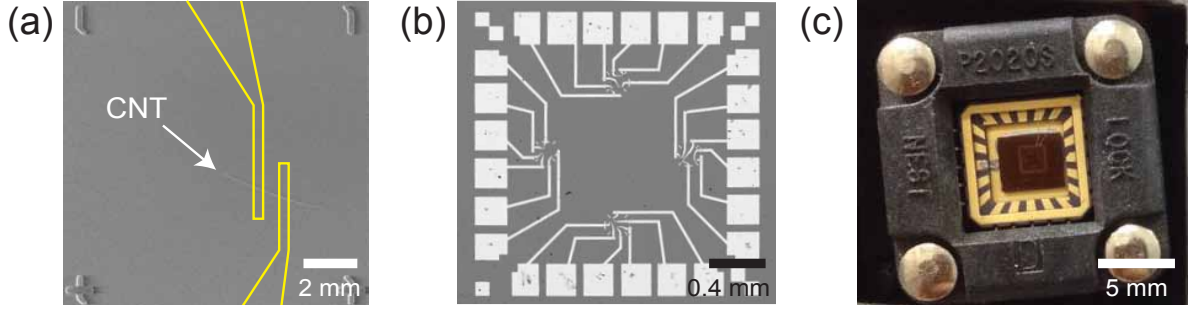


**Figure 3.2.** (a) SEM image of a selected CNT with electrical contact design for a two-terminal device. The four alignment markers are used as a coordinate system to uniquely determine the position of the selected CNTs. (b) A grayscale optical microscopy image of a chip with 12 two-terminal CNT devices. (c) A photo image of a chip carrier mounted in a chip socket of a cryostat. The chip is first glued into the chip carrier and contacted by wire bonding. There are 20 pins in total.

an additional EBL is performed to fabricate side gates, bottom gates, or top gates. In Fig. 3.2(b), for the bonding pads, outer leads, and normal metal contacts, we deposit 60 nm thick palladium (Pd).

After the fabrication of electrical contacts to the selected CNTs, we cut the  $1 \times 1 \text{ cm}^2$  size substrate into 4 pieces of  $4 \times 4 \text{ mm}^2$  size. We fabricate 12 CNT devices on each substrate in order to achieve a good yield of working devices. We measure the room temperature two-terminal resistance of the device and its dependence on the back-gate voltage. This provides a fast feed back to identify the metallic (or quasi-metallic) and semiconducting CNTs [36]. The  $4 \times 4 \text{ mm}^2$  size substrate is glued into a chip carrier, and the devices are wire bonded to the individual pins of a chip carrier. One of the chip carrier pins is wire bonded to the bottom of the chip carrier, which is connected to the back-gate. The chip carrier is placed in a chip socket of a cryostat, see Fig. 3.2(c). The sample is ready for cooling down to the base temperature of a cryostat. We note that we only cool down CNT devices that show room temperature two-terminal resistance that is less than few  $\text{M}\Omega$ .

## 3.2. Fabrication of hBN-CNT heterostructures

In this section, we introduce the fabrication schemes of our hBN/CNT heterostructures, where hBN is used for the following four purposes:

- clean substrates;
- insulators for top finger gates;
- tunnel barriers;
- to encapsulate the CNTs.

### 3.2.1. hBN substrate for CNT QDs

Here, we describe the fabrication details of a CNT QD realized on top of an hBN flake. The fabrication technique used on hBN flakes is easily applicable to more complex

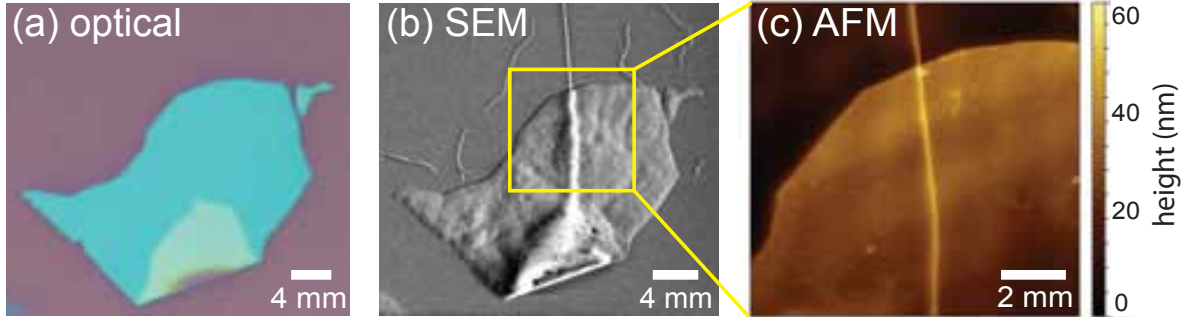


**Figure 3.3.** (a) Optical, (b) SEM, and (c) AFM image of a CNT ( $\sim 8$  nm radius) on an hBN flake ( $\sim 28$  nm thickness) on a  $\text{SiO}_2$  substrate.

devices, similar as on standard wafer substrates. This suggests that hBN flake can be used as a substrate for a variety of nanostructures.

### hBN exfoliation

We deposit hBN flakes by mechanical exfoliation of commercially available hBN powder using the well-known “scotch tape” method [49]. First, we place a sufficient amount of hBN powder on the adhesive side of the scotch tape. Afterwards, the scotch tape is refolded, pressed firmly, and then gently unfolded. This leaves two mirrored areas of hBN flakes on the tape. We repeat this process several times until a large portion of the scotch tape is uniformly covered by hBN flakes. At the end, we place the scotch tape onto a clean  $1 \times 1 \text{ cm}^2$  size substrate, press firmly, and then gently peel away. We use a highly p-doped Si substrate with 300 nm thick thermally grown  $\text{SiO}_2$  as a capping layer. Flakes with different number of layers are exfoliated onto the substrate.

### CNT growth on hBN flakes and localization of CNTs

After exfoliating hBN flakes onto a clean Si/ $\text{SiO}_2$  substrate, we follow the CNT growth procedure as presented in Section 3.1 to grow CNTs on hBN flakes. We pattern the sample substrate with alignment markers, which will be used to locate not only the CNTs but also the hBN flakes. Figure 3.3(a) shows the optical microscopy image of a  $\sim 28$  nm thick hBN flake after CNT growth. The contrast and color allow for an initial screening for suitable flakes on a marker field before the device fabrication. The CNTs are not visible using an optical microscope and can only be found by SEM or atomic force microscopy (AFM) imaging, as demonstrated for the same hBN flake in Fig. 3.3(b) and Fig. 3.3(c), respectively. The images show a CNT with a radius of  $\sim 8$  nm on the  $\sim 28$  nm thick hBN flake. The CNT radius and hBN thickness are determined from the corresponding AFM images. Since AFM imaging is slow and restricted to rather small scan ranges, we have optimized the SEM parameters with the goal of obtaining simultaneous image contrast for both, hBN flakes and CNTs. For flakes thinner than  $\sim 40$  nm, we regularly find CNTs on hBN flakes suitable for device fabrication.

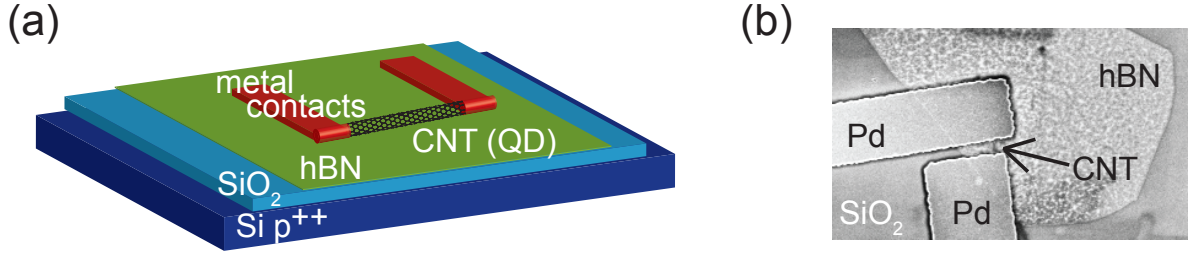


**Figure 3.4.** (a) Schematic and (b) SEM image of a CNT QD structure on hBN.

### Electrical contacts to CNTs on top of hBN flakes

The fast and reliable SEM imaging of CNTs on hBN flakes allows the fabrication of electrical contacts by standard EBL. We use the ZEP electron-beam resist to obtain polymer free CNTs and reliable CNT contacts [27] and thermal evaporation of  $\sim 80$  nm Pd to fabricate two-terminal devices on CNTs on top of hBN flakes. The structure of our devices is shown schematically in Fig. 3.4. With our fabrication approach we obtain a low device yield mainly due to the limited number of hBN/CNT heterostructures that are available for depositing electrical contacts. We can significantly increase the final device yield by increasing the number of hBN flakes on the substrate.

In this context, we investigate CVD grown multi-layer hBN films as substrates for our CNT QD devices. The hBN film is commercially available, and we are motivated by its large size, as this allows us to boost the probability of finding CNTs on hBN. We transfer the film from its growth substrate onto a Si/SiO<sub>2</sub> substrate using a wet-etching method [103]. Our study shows that using hBN film as a substrate significantly increases the number of working devices. However, the surface roughness and the number of structural defects, such as holes and wrinkles, dramatically increase during its transfer onto a Si/SiO<sub>2</sub> substrate. As a result, at low temperatures multiple uncontrolled QDs form in the system. We believe that improvement of our transfer technique is essential for exploring the potential of hBN films as a clean substrate for our CNT devices.

### 3.2.2. hBN capped CNTs with top finger gates

We aim to fabricate a disorder-free and locally-tunable 1D system in our CNTs by utilizing narrow finger gates on top and hBN flakes as gate insulators. This allows us to locally deplete the semiconducting CNTs to form tunnel barriers and charge puddles, i.e., QDs. We demonstrate that CNTs can be transferred from the growth substrate onto a target substrate by means of a stamping technique [104], while freshly cleaved hBN flakes can be deterministically transferred by a all-dry viscoelastic stamping process [105] onto the target substrate to cover the CNTs. We note that narrow finger gates on hBN flakes by standard EBL is difficult to achieve.

#### CNT stamps preparation and stamping process

The device fabrication starts with making a mesa structure of  $50 \times 50 \mu\text{m}^2$  in size and  $4 \mu\text{m}$  in height on a clean Si/SiO<sub>2</sub> substrate by following T. Hasler's optimized recipe for stamping CNTs [104]. We use an undoped Si substrate with a capping layer of 170 nm

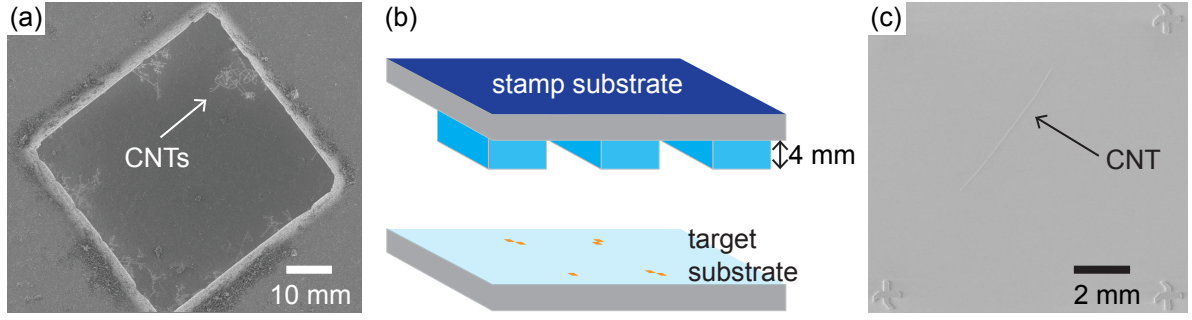


**Figure 3.5.** (a) SEM image of a  $50 \times 50 \mu\text{m}^2$  size Mesa square after the CNT growth. (b) Schematic illustration of the CNT stamping process. (c) SEM image of a stamped CNT on a target substrate.

thick thermally grown  $\text{SiO}_2$ . A bilayer of PMMA and hydrogen silsesquioxane (HSQ) is spin-coated onto the substrate. We note that PMMA is used not only as a protective coating layer but also as a sacrificial layer for wafer thinning. HSQ is exposed to an e-beam to transfer the desired mesa structure into the resist layer. Development of HSQ in tetramethylammonium hydroxide (TMAH) removes the unexposed areas of HSQ and leaves exposed areas on the substrate. We etch away the unprotected areas of PMMA with  $\text{O}_2$  plasma in a reactive ion etcher. This is followed by a chemical wet-etching of  $\text{SiO}_2$  in hydrogen fluoride (HF) and then a sulfur hexafluoride ( $\text{SF}_6$ ) plasma etching of Si in a reactive ion etcher. The desired mesa structure is obtained by removing the PMMA and HSQ in acetone. Undiluted Mo/Fe catalyst is spin-coated 5 times onto the mesa structure, and we grow CNTs in a CVD oven with methane as a source gas at  $950^\circ\text{C}$  for 10 min. Figure 3.5(a) shows an SEM image taken after the CNT growth on a mesa structure. This method results in a large amount of CNTs.

We stamp the CNTs onto a target substrate with the help of a mask aligner. The target substrate is a heavily p-doped Si wafer with 300 nm thick  $\text{SiO}_2$  on top. We pattern the target substrate with 5 nm/45 nm thick Ti/Au alignment markers by standard EBL. The CNT stamp and the target substrate are placed on a mask aligner and roughly aligned using the Ti/Au alignment markers and pressed firmly together, see Fig. 3.5(b). The alignment markers are used to locate the CNTs after stamping the CNTs onto the target substrate, see Fig. 3.5(c). We note that each time a reasonable amount of CNTs (6 – 10) can be successfully stamped onto a  $200 \times 200 \mu\text{m}^2$  writing field area. Standard EBL is performed to contact the CNTs with 20 nm thick Pd leads, and we characterize the room temperature two-terminal resistance of our devices. Devices with resistances smaller than  $1 \text{ M}\Omega$  are selected to place hBN flakes on top to cover the CNTs.

### Transfer of hBN flakes

Polypropylene carbonate (PPC) is spin-coated onto a clean Si/ $\text{SiO}_2$  substrate, and hBN flakes are mechanically exfoliated on PPC from a scotch tape. We search for hBN flakes with suitable size ( $\sim 10 \times 10 \mu\text{m}^2$ ) and thickness (20 – 60 nm) under an optical microscope. We note that the optical color contrast of the flakes on PPC is different from that on 300 nm thick  $\text{SiO}_2$ . The hBN/PPC complex is first peeled away from the substrate using a scotch tape frame and then placed onto a  $4 \times 4 \times 2 \text{ mm}^3$  size



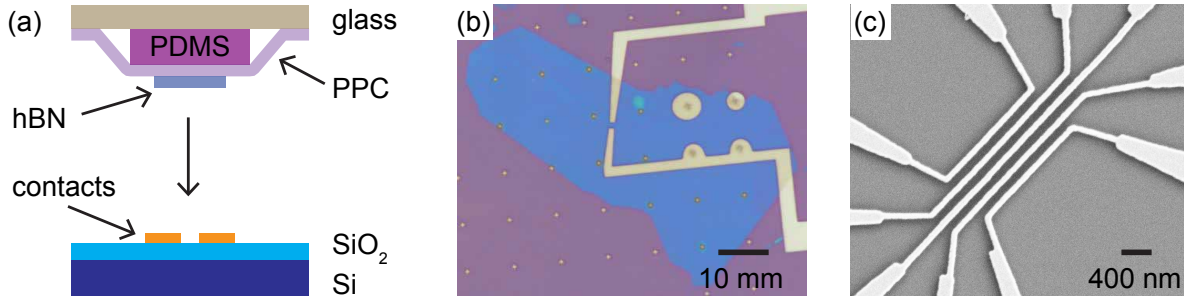


**Figure 3.6.** (a) Schematic illustration of the hBN flakes placing process.. (b) A real-color optical microscopy image of a two-terminal CNT device covered by an hBN flake. (c) SEM image of a five finger gates fabricated on a Si/SiO<sub>2</sub> substrate with an optimal dose parameter.

polydimethylsiloxane (PDMS) block, which is placed on a glass slide, see Fig. 3.6(a). We fix the target substrate on the stage of the optical microscope, align it with respect to the selected hBN flake, and then bring them in contact. The sample is heated up to 90°C and remains at this temperature for  $\sim 1$  min. Then, the heater is switched off and the glass slide is slowly retracted. The PPC melts, and the hBN/PPC complex is released on the target substrate. We remove the PPC in chloroform afterwards. Figure 3.6(b) shows an optical microscopy image of a two-terminal CNT device that is covered by a large hBN flake. In this figure, the distance between the source and drain contacts is  $\sim 1.2 \mu\text{m}$ .

### Fabrication of finger gates on hBN flakes

We aim to fabricate five finger gates on the hBN flake by standard EBL. We first start with fabricating finger gate structures on a standard wafer substrate using 300 nm thick PMMA or ZEP. Figure. 3.6(c) shows the SEM image of five finger gates fabricated on a Si/SiO<sub>2</sub> substrate with an optimal dose parameter. Afterwards, we use this optimal dose parameter to fabrication finger gates on an hBN flake. We find that the electron-beam dose parameter is extremely sensitive to the thickness variation of the hBN flake. This means that one needs to optimize the writing parameter for each individual flakes. In our approach, we only rely on the optical contrast of hBN on PPC to roughly select flakes thinner than 40 nm. As a result, we often obtain devices with at least one finger gate being electrically shorted by the neighboring gate.

### 3.2.3. hBN encapsulated CNTs with 0D side contacts

Here, we focus on the fabrication of hBN encapsulated CNTs that are coupled to normal metals and superconductors by 0D side contacts. Figure 3.7(a) show the schematic cross section view of the device. One technical advantage of the 0D side contacts in our controlled “mixed-dimensional” heterostructures is the very large yield and reproducibility of the contact properties.

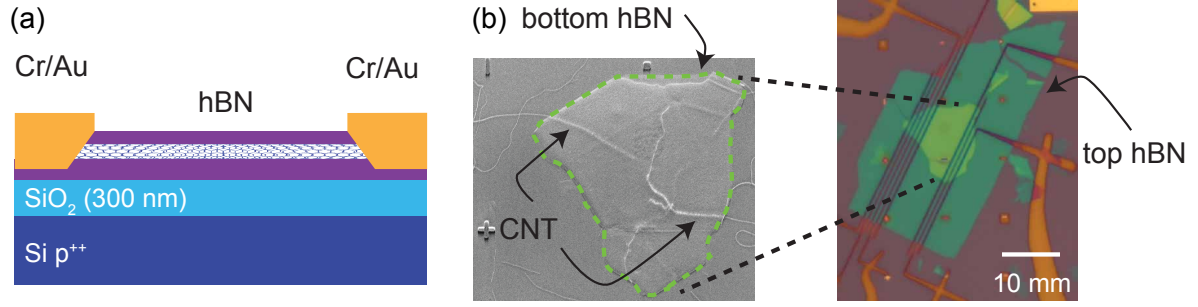


**Figure 3.7.** (a) Schematic cross section view of an hBN encapsulated CNT device with 0D side contacts. (b) SEM image (left) of a mechanically exfoliated hBN flake with few CNTs transferred on top of it using PPC. Optical image (right) of the device using the hBN flake as the bottom layer for the encapsulation of the CNTs.

### hBN substrate preparation

We aim to prepare a substrate that is densely covered by freshly cleaved hBN flakes. We first pattern a  $1 \times 1 \text{ cm}^2$  size substrate with 5 nm/45 nm thick Cr/Au alignment markers and bond pads by EBL. We deposit hBN flakes by mechanical exfoliation of hBN crystals using a scotch tape. We repeat the exfoliation several times to attain a large amount of hBN flakes on the substrate. We use the alignment markers to locate the CNTs and the hBN flakes. A thermal annealing in an oven at  $370^\circ\text{C}$  for 3 h in a forming gas ( $\text{H}_2$  and  $\text{N}_2$ ) ambient is performed to remove the polymeric residues.

### PPC-assisted transfer of CNTs onto hBN flakes

The next step is to locally place the CNTs onto the hBN flakes, and there are three applicable techniques to achieve this. The first technique is the direct growth of CNTs on hBN flakes as discussed in Section 3.2.1. This is a simple, fast, and clean approach. The second technique is stamping CNTs from the growth substrate onto the target substrate by following the steps demonstrated in Section 3.2.2. Both techniques produce CNTs that are free from polymer residues, but the drawback is the low device yield due to the extremely low probability to have a CNT that is laying on an hBN flake. In order to overcome this issue, we have developed a third method, where we transfer the CNTs from the growth substrate onto the target substrate with PPC.

We first grow CNTs on a Si/SiO<sub>2</sub> substrate and then spin coat a thick layer of PPC film and bake it at  $80^\circ\text{C}$  for 5 min. Afterwards, we attach a frame that is made out of an adhesive tape around the edges of the PPC film. We peel away the PPC film and place it onto the target substrate. The film is attached to the target substrate by heating at  $120^\circ\text{C}$  for 3 min. The adhesive tape is removed with a tweezer, and the PPC film is dissolved in chloroform. After the removal of PPC, we search and locate hBN flakes with preferably one or two CNTs laying on top. The SEM image of an hBN flake after the PPC-assisted transfer of CNTs is shown in Fig. 3.7(b) (left). We note that this approach is very efficient in transferring CNTs onto the hBN flakes. A comparison between the SEM images of a CNT growth substrate taken before and after the PPC-assisted transfer of CNTs reveals that most of the CNTs are attached to the PPC film and successfully transferred onto the target substrate.

## CNT encapsulation

We can control the density of CNTs on hBN flakes by tuning the density of hBN flakes that are exfoliated on the substrate. On a  $1 \times 1 \text{ cm}^2$  size wafer substrate, we often find 5 – 10 individual hBN flakes with only one or two CNTs laying on each individual flake. This allows us to select the most suitable hBN/CNT complex for encapsulation. Here, a suitable hBN/CNT complex means that the hBN flake has a thickness in the range of 20 – 40 nm, and the CNTs on hBN flakes appear less visible and straight under SEM with a length of  $\sim 5 \mu\text{m}$ . We encapsulate the CNT by placing an hBN flake on top, and this is done by following the hBN capping layer placing process described in Section 3.2.2. In Fig. 3.7(b) (right), we show the optical microscopy image of an hBN/CNT/hBN heterostructure with the bottom and top hBN flakes clearly visible.

In parallel, CVD grown multi-layer hBN films are investigated as a top layer for the encapsulation. The multi-layer hBN film is transferred from its growth substrate Cu foil onto the target substrate using a wet-etching method. Our study shows that the selected hBN/CNT complex is poorly covered by the hBN film, as confirmed by the SEM images taken after the encapsulation. Fabrication of 0D side contacts to the heterostructure results in devices with no measurable conductances at room temperature.

## 0D side contacts to the encapsulated CNTs

After the CNT encapsulation, 300 nm thick PMMA is spin-coated, and we pattern the PMMA resist layer with electrical contact structures using EBL. After the development of PMMA in a 7 : 3 mixture solution of isopropyl alcohol/water (IPA/H<sub>2</sub>O) at  $\sim 5^\circ\text{C}$  for 1 min, we place the sample in a reactive ion etcher to locally etch away the hBN/CNT/hBN heterostructure either with fluorocarbon/oxygen (CHF<sub>3</sub>/O<sub>2</sub>) plasma or with sulfur hexafluoride/argon/oxygen (SF<sub>6</sub>/Ar/O<sub>2</sub>) plasma. Directly after the plasma etching, we deposit 10 nm/60 nm thick Cr/Au in an electron-beam evaporator or sputter 70 nm thick molybdenum silicide (MoSi) with Ar plasma. We note that the reactive ion etching cuts the encapsulated CNT into segments. A direct deposition of a normal metal or a superconductor results in electrical contacts only along the circumference of the CNT. The diameter of a single-wall CNT is on the order of 1 nm. Thereby, metalization of the end of an encapsulated CNT results in 0D side contacts.

It is known that Pd is a good electrical contact material for both metallic and semi-conducting single-wall CNTs [58, 106], when it is deposited directly on top of the CNTs. However, Pd does not form electrical contacts in this scheme. Our studies on the fabrication of 0D side contacts to the encapsulated CNTs using a variety of electrical contact materials, such as Pd, palladium/lead/indium (Pd/Pb/In), titanium/aluminum (Ti/Al), Cr/Au, Cr/Al, and MoSi, show that only Cr/Au and MoSi make electrical contacts to the encapsulated CNTs. This limits us to use only Cr/Au as normal metal contacts and only MoSi as superconducting contacts. We are aware that there are very little studies on the superconducting properties of a bulk or a thin film of MoSi [107–109].

### 3.2.4. hBN tunnel barriers to CNTs

Here, we present the fabrication details of our CNT devices with large scale CVD grown monolayer hBN films as tunnel barriers. Figure 3.8 shows the schematic cross section view of our devices with tunnel contacts. A CNT with direct clean metal contacts (e.g. Pd) forms QDs of the size determined by the contact separation, or, in disordered CNTs, by defects and potential fluctuations. By placing hBN film as a tunnel barrier to the CNT, we expect to observe a large QD that is not confined by the metal contacts. We use wet-etching [103] and electrochemical bubbling methods [110] to transfer the films onto the target substrate to form a tunnel barrier to the CNT.

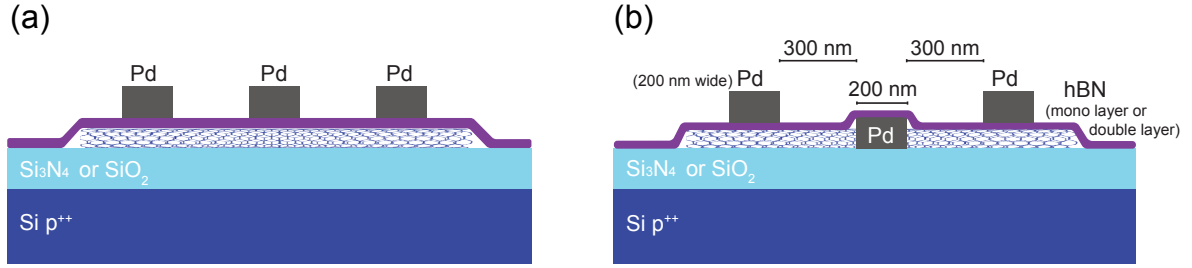


**Figure 3.8.** Schematic cross section view of CNT devices with hBN tunnel barriers. (a) Three-terminal tunnel contacts to a CNT. (b) A three-terminal device with two tunnel contacts and one normal contact.

#### Sample preparation

The sample fabrication starts with patterning the target substrate with 5 nm/45 nm thick Ti/Au alignment markers by EBL. We use a heavily p-doped Si wafer that is capped either by 300 nm thick SiO<sub>2</sub> or by 200 nm thick Si<sub>3</sub>N<sub>4</sub>. We stamp the CNTs onto the target substrate. A small amount of catalyst particles are stamped onto the target substrate as well. The presence of these catalyst particles nearby a CNT is problematic for placing atomically thin hBN tunnel barriers. An alternative approach is the direct growth of CNTs on a wafer substrate, which is prepatterned with 40 nm thick Re alignment markers. In practice, any metal that is compatible with the CNT growth conditions, especially the high growth temperature of  $\sim 1000^\circ\text{C}$ , can be used for the alignment markers. We note that SEM contrast of Re is much weaker than that of Ti/Au and makes it difficult to locate the CNTs. After locating the CNTs with respect to the alignment makers using SEM imaging, we transfer the hBN film from its growth substrate Cu or Fe foil onto the target substrate to cover the CNTs. We employ the wet-etching [103] and the electrochemical bubbling methods [110] to transfer the film, as described in Fig. 3.9 and Fig. 3.10, respectively. We select CNTs of several micrometers long and fabricate tunnel contacts to the CNTs by thermal evaporation of  $\sim 20$  nm thick Pd on the hBN film.

#### Wet-etching method

We adopt the wet-etching technique to transfer the CVD grown hBN film from its growth substrate Cu foil onto the Si/SiO<sub>2</sub> substrate. The wet-etching method is further

divided into the wet and dry transfer processes, as shown in Fig. 3.9. The hBN film, which is commercially available, is grown on both sides of the Cu foil, and we first describe the wet transfer process. We spin-coat  $\sim 1 \mu\text{m}$  thick PMMA on one side of the Cu foil to protect the film and etch away the hBN film on the other side of the foil in a reactive ion etcher using  $\text{CHF}_3/\text{O}_2$  plasma. Afterwards, the Cu foil is etched away by chemical wet-etching in a  $\sim 2\%$  ammonium persulfate solution. The remaining hBN/PMMA complex is rinsed with distilled water to wash off the etchant residues. We place the hBN/PMMA complex onto the Si/SiO<sub>2</sub> substrate by fishing it out directly from the distilled water and let it dry in ambient conditions. A heat treatment is carried out to soften the PMMA, thereby increasing the adhesion between the film and the substrate. At the end, we immerse the sample in acetone to remove the PMMA. A thermal annealing in a furnace at  $250^\circ\text{C}$  with forming gas ( $\text{H}_2$  and  $\text{N}_2$ ) for 3 h is carried out to remove the PMMA residues.

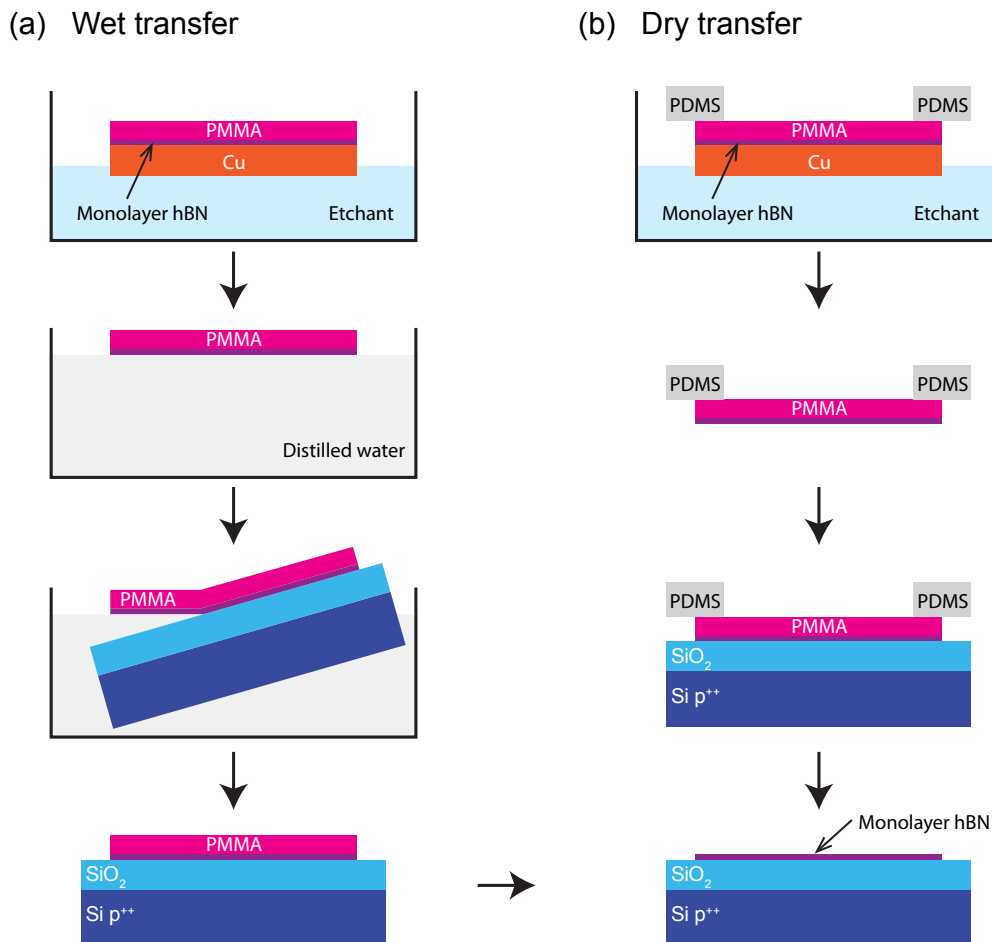


**Figure 3.9.** Schematic illustration of the wet-etching method used for transferring the CVD grown hBN film from the Cu foil. (a) Wet and (b) dry transfer process.

The wet transfer process can lead to water layers being trapped between the hBN film and the substrate. In order to avoid this, we introduce the dry transfer process, where we use PDMS frame to support the hBN/PMMA complex. It allows us to remove the hBN/PMMA/PDMS complex from the etchant with tweezers and rinse it with distilled

water. We place the complex and the target substrate inside a glove box. The target substrate is first heated at 200°C for 12 h to remove the solvent residues from its surface and then cooled down to the room temperature. Afterwards, we place the complex onto the target substrate and slowly increase the hotplate temperature to 140°C while pressing hard on the PDMS frame with tweezers. The sample is then removed from the glove box and immersed in acetone to remove the PMMA and PDMS. A complete removal of PMMA is difficult to achieve [111]. Acetone and chloroform treatments of PMMA lead to contaminated hBN surfaces with polymer residues. Thermal annealing of the sample at temperatures in the range of 300 – 400°C in vacuum [112] or in an Ar/H<sub>2</sub> flow [113] and the removal of PMMA by catalytic activity of platinum (Pt) metals [114] appear to help, but they do not lead to ultra-clean hBN films.

### Electrochemical bubbling method

For hBN films grown on Fe foils, we employ the electrochemical bubbling method based on the electrolysis of water between the layers to separate the materials. Here, the hBN film is grown on a 100  $\mu\text{m}$  thick Fe foil by our collaborator [51]. A schematic illustration of the electrochemical bubbling transfer process is shown in Fig. 3.10. First, the foil is spin-coated with  $\sim 1 \mu\text{m}$  thick PMMA. Afterwards, the hBN/Fe/hBN/PMMA complex and a Pt metal plate are placed in a 1 M NaOH aqueous solution and used as the cathode and anode of an electrolysis cell, respectively. The reaction of water reduction takes place at the negatively charged Fe foil to produce a large amount of H<sub>2</sub> bubbles at the interface between the film and the foil. This leads to the detachment of the hBN/PMMA complex from the Fe foil in few minutes. After rinsing with distilled water, a target substrate is dipped into the distilled water to fish out the floating hBN/PMMA complex. The sample is heated to increase the adhesion between the film and the substrate. PMMA is removed by immersing the sample in acetone and rinsing in

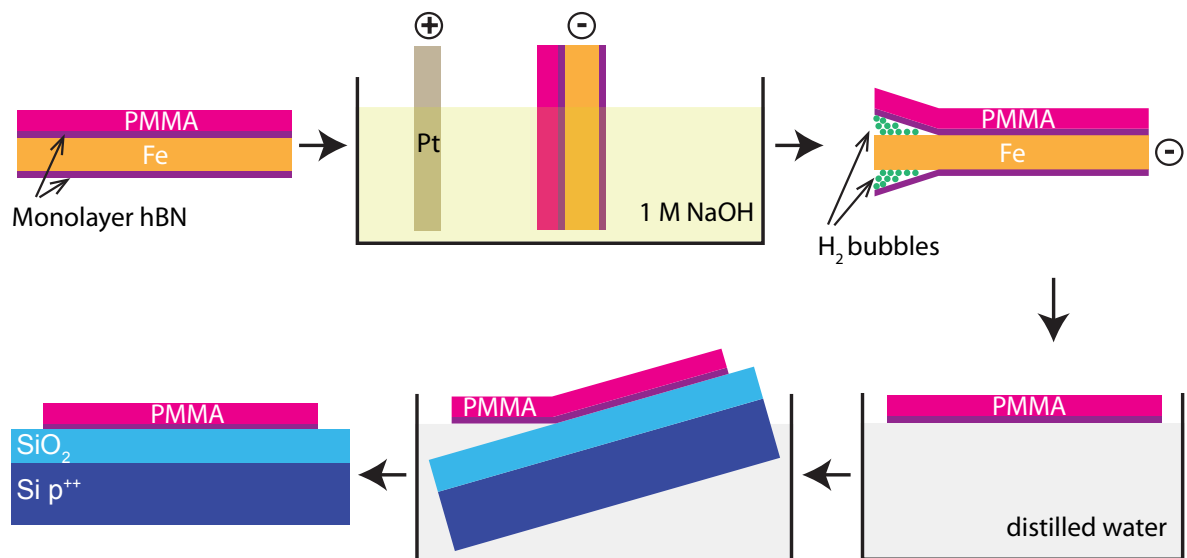


**Figure 3.10.** Schematic illustration of the electrochemical bubbling method used for transferring CVD grown hBN film from the Fe foil.

IPA. In comparison to the wet-etching method, the electrochemical bubbling is faster, and the hBN film transferred using this method is free of metal residues. However, we find that the electrochemical bubbling method is aggressive enough to break the atomically thin hBN film, thereby creating a large amount of structure defects, such as holes and wrinkles.

### 3.3. Cryogenic measurement set-up

Characterization of the electronic transport properties of our CNT-based nanostructures requires an electronic temperature that is well below the relevant energy scales of our devices, for example, the charging energy  $E_C$ , the level spacing  $\delta E$ , the lifetime broadening  $\Gamma$ , the superconducting energy gap  $\Delta$ , and the characteristic critical temperature  $T_C$ . Several cryogenic measurement set-ups with base temperatures varying from 4.2 K to 10 mK are employed for the electronic transport measurements. One can achieve a base temperature of 4.2 K by placing the device into a liquid  $^4\text{He}$  bath, since this is the boiling point of the liquid  $^4\text{He}$  at one atmosphere. Pumping on a liquid  $^4\text{He}$  bath leads to a lower base temperature of  $\sim 1.5$  K by evaporative cooling that is determined by the respective vapor pressure. A further decrease of the base temperature to  $\sim 230$  mK can be achieved with a  $^3\text{He}$  cryostat by pumping on the liquid  $^3\text{He}$  bath, as the isotope  $^3\text{He}$  has a larger vapor pressure in comparison to that of  $^4\text{He}$ . Even lower base temperature of  $\sim 10$  mK can be attained with a  $^3\text{He}/^4\text{He}$  dilution refrigerator that uses a mixture of  $^3\text{He}$  and  $^4\text{He}$  isotopes. In the mixing chamber, when cooled below  $\sim 870$  mK, the mixture undergoes a spontaneous phase separation to form a  $^3\text{He}$  rich phase (the concentrated phase) and a  $^3\text{He}$  poor phase (the dilute phase) that are separated by a phase boundary [115]. An osmotic pressure difference created by an elaborate pumping and cooling scheme constantly drives more  $^3\text{He}$  from the concentrated phase through the phase boundary to the dilute phase. This process is exothermic and removes heat from the mixing chamber environment, thereby providing the cooling power of the refrigerator. Superconducting magnet is available in the cryostat and allows us to study the transport characteristics of the device in a magnetic field up to 8 T.

At sufficiently low temperatures, the interaction between the charge carriers and the phonons (lattice vibration) can be so weak that the electrons and the phonons decouple from each other and obtain different temperatures [115]. The device placed in a cryogenic environment is connected to the electronic measurement instruments that are at room temperature. The phonon lattice of the device, which is cooled to the base temperature of a cryostat, cannot fully absorb the heat coming from the room temperature environment through the measurement lines. The high frequency thermal noise and the electromagnetic noise propagate through the measurement lines and perturb the microscopic system to be studied. Therefore, filters are necessary for the measurement lines. We use commercially available  $\pi$ -filters from Syfer at room temperature and specifically designed tape-worm filters at cryogenic temperatures [116] with a cut-off frequency  $f > 1$  MHz and  $f > 10$  MHz, respectively. In addition, the measurement lines are thermally anchored by Cu wires. Figure 3.11 shows a schematic illustration of a typical cryogenic measurement set-up.

We apply a dc and an ac bias,  $V_{SD} + \delta V$ , and measure the differential conductance

$G = \delta I / \delta V$  of the device using standard lock-in techniques. The dc bias  $V_{SD}$  is provided by a low noise DC voltage source, Yokogawa YK 7651, and a small ac bias  $\delta V \sim 10 \mu\text{V}$  with a frequency  $f \sim 17 - 400 \text{ Hz}$  is supplied by a lock-in amplifier, Stanford SR 830. We superimpose  $\delta V$  on  $V_{SD}$  using a transformer with 1 : 4 winding ratio, and a voltage divider with a division ratio of 1 : 1000 attached directly before the  $\pi$ -filter on the break-out box. We read out the current with a low noise current-to-voltage (I/V) converter with a transimpedance of  $10^6 - 10^7 \text{ V/A}$ . The output voltage of the I/V converter is connected to the lock-in amplifier to measure  $\delta I$ . We apply a dc voltage through a resistor  $R \sim 1 \text{ M}\Omega$  to the back-gate using either Yokogawa YK 7651 or an 8-channel low noise digital to analog voltage source, DAC SP 927. The resistor in series limits the current in case of a gate leak. We use a computer to control the measurement set-up using Labview programs, RS232 serial ports, and General Purpose Interfaces (GPIB).

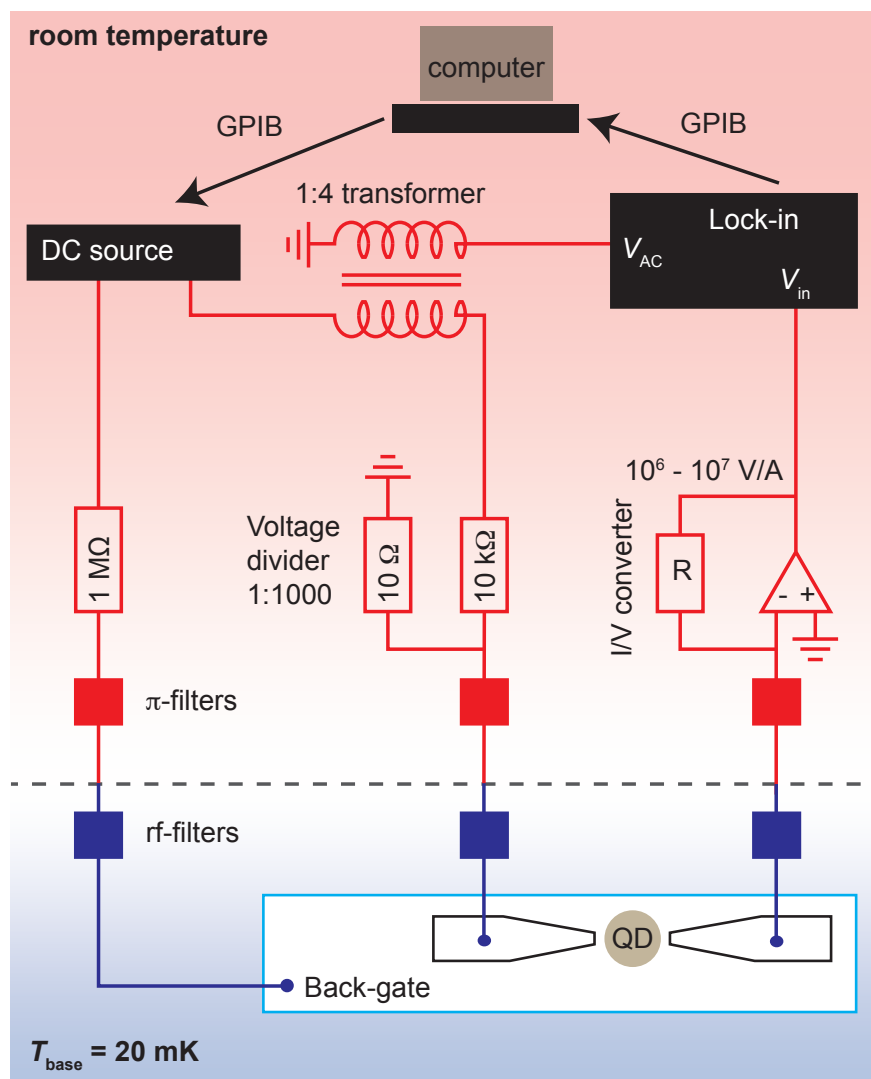


**Figure 3.11.** Schematic illustration of a typical cryogenic measurement set-up for a voltage biased differential conductance measurement using a standard lock-in technique. This figure is adapted from Ref.[117].



# 4 Clean carbon nanotube quantum dots on hexagonal boron nitride

---

## 4.1. Introduction

To date, the use of hBN as a clean substrate or a high-quality gate dielectric for more complex nanostructures has not been demonstrated. Specifically, our experiments on CNTs grown on hBN flakes show that CNTs are difficult to locate on hBN flakes, because optical microscopy lacks the required resolution, scanning electron microscopy (SEM) images can be of poor quality, and imaging by atomic force microscopy (AFM) is rather demanding because of the large lateral and vertical scales involved, while requiring nanometer resolution to image CNTs [34].

In this chapter, we study the SEM imaging contrast for locating CNTs on hBN flakes. We report that for a range of hBN thicknesses and SEM settings, rapid feed-back and large scale SEM imaging of CNTs on hBN flakes are possible, also shedding light on the contrast mechanisms when imaging nano-objects on dielectrics. Based on this result, we fabricate CNT QD devices made using hBN flakes either as clean substrates or top finger gate dielectrics and report the low-temperature transport characteristics, i.e., the formation of a “clean” QD. We demonstrate that the electronic structure of our CNT QD devices indicates a very good electrical device quality and stability. This work has been partially published in Ref.[34].

## 4.2. SEM imaging contrast mechanism

The SEM contrast of hBN and CNTs depends crucially on the SEM electron acceleration voltage  $U_{acc}$ . Figures 4.1(a)-4.1(e) show a series of SEM images at different  $U_{acc}$  of a  $\sim 1$  nm radius CNT lying partly on  $\text{SiO}_2$  and partly on hBN. We use an in-lens detector, an aperture of  $30 \mu\text{m}$ , and a primary electron (PE) beam current of  $\sim 1$  nA. The hBN thickness in this image increases in two steps, first to  $\sim 35$  nm (arrow i in Fig. 4.1(e)) and then to  $\sim 80$  nm (arrow ii).

For the lowest acceleration voltage shown in Fig. 4.1(a), the hBN flake is barely visible, while the CNTs have the largest contrast of all investigated voltages (the flake position can be found by comparing to the other sub-figures). With increasing  $U_{acc}$ , the hBN flake becomes continuously easier to distinguish. For low  $U_{acc}$ , the hBN bulk contrast is small and the flakes are mainly visible at the edges, consistent with a topographically determined emission of secondary electrons (SEs). The SEM contrast of the CNTs is more complex. For  $U_{acc}$  up to  $\sim 2$  kV the contrast is similar for CNTs on hBN and directly on  $\text{SiO}_2$ . It is positive up to around  $U_{acc} = 1$  kV and negative at higher

voltages. On hBN the contrast vanishes at  $U_{\text{acc}} \approx 2.2$  kV, while on  $\text{SiO}_2$  it becomes positive again for  $U_{\text{acc}} > 4$  kV and remains roughly constant up to  $U_{\text{acc}} = 20$  kV, the maximum investigated voltage. The CNT contrast  $(I_{\text{CNT}} - I_{\text{sub}})/(I_{\text{CNT}} + I_{\text{sub}})$  is plotted in Fig. 4.1(f) as a function of  $U_{\text{acc}}$  for the cross sections indicated in Fig. 4.1(b), with the maximum intensities from the CNT and the substrate,  $I_{\text{CNT}}$  and  $I_{\text{sub}}$ , respectively.

The apparent CNT widths from the same image cross sections are plotted in Fig. 4.1(g). The width is similar on both materials at the lowest voltages, but about four times larger on hBN than on  $\text{SiO}_2$  around  $U_{\text{acc}} = 0.7$  kV. It also depends qualitatively different on  $U_{\text{acc}}$ : on hBN it increases with  $U_{\text{acc}}$  at low voltages and then decreases at higher values. On  $\text{SiO}_2$  the width continuously decreases with  $U_{\text{acc}}$  and becomes roughly constant at higher voltages. When the contrast is negative, the width changes differently. From these measurements, we find an optimal  $U_{\text{acc}}$  between 0.6 kV and 1.0 kV for simultaneously imaging hBN flakes and CNTs.

On flakes thinner than  $\sim 10$  nm, the apparent CNT diameter and contrast is almost identical on hBN and on the bare  $\text{SiO}_2$ . This is illustrated in Fig. 4.2(a), which shows an SEM image of several CNTs on a 6 nm thick hBN flake. The CNT on the right side of the flake has a radius of  $\sim 5.5$  nm. Though thin flakes lead to a better SEM contrast, the detrimental effects of the  $\text{SiO}_2$  below the hBN will have an increased impact on an actual device. The contrast changes with the hBN thickness can be directly seen in Fig. 4.2(b), with the corresponding AFM image in Fig. 4.2(c). Two CNTs cross on top of the hBN flake, but both are visible in the SEM image only at the edges of the flake (bulk thickness  $\sim 30$  nm) and on the  $\text{SiO}_2$ . The CNT spanning the whole flake has a radius of  $\sim 8$  nm. At the edges of the flake, the hBN thickness increases continuously while the SEM contrast of the CNT is continuously diminished. We note that the first hBN step in Fig. 4.1 is also roughly 30 nm, but the SEM still shows a clear contrast for the CNT, suggesting a dependence of the contrast on the CNT diameter (CNT radius in Fig. 4.1 is  $\sim 1$  nm, in Fig. 4.2(b)  $\sim 8$  nm). Generally, it is easier to find CNTs that completely span a given hBN flake. These tubes probably grow vertically and then fall across the flake. However, we regularly find CNTs starting and ending on larger hBN flakes, suggesting that CNTs also grow directly on top of the flakes.

The contrast mechanism for SEM imaging of CNTs on insulating substrates [118, 119] can be understood qualitatively in a simple picture: in the bare substrate the incident PEs generate a large number of SEs in the dielectric at energies lower than the PEs, but larger than the material's energy gap. These SEs can leave the substrate through the surface or absorbed in the material. The total charge of the layers depends on the balance between the number of injected PEs and emitted SEs. At low acceleration voltages, the PEs do not penetrate deep into the substrate and more SEs are emitted than absorbed, which leads to a positively charged surface layer [120]. At higher voltages, the electrons penetrate deeper and leave the dielectric with reduced probability, which leads to a negative charging by the PEs. When the PE and SE penetration depths reach the insulator thickness, the SEs can be absorbed by the conducting back-gate and the dielectric can again become positively charged.

Intuitively, the generation of SEs depends on the local electron density. The CNTs can be seen as charge reservoirs (or capacitors if not connected to an electrical contact) that supply or accept electrons from the substrate, leading to an electric field determined by the surface charging and thus by the SEM acceleration voltage. Since the surface is

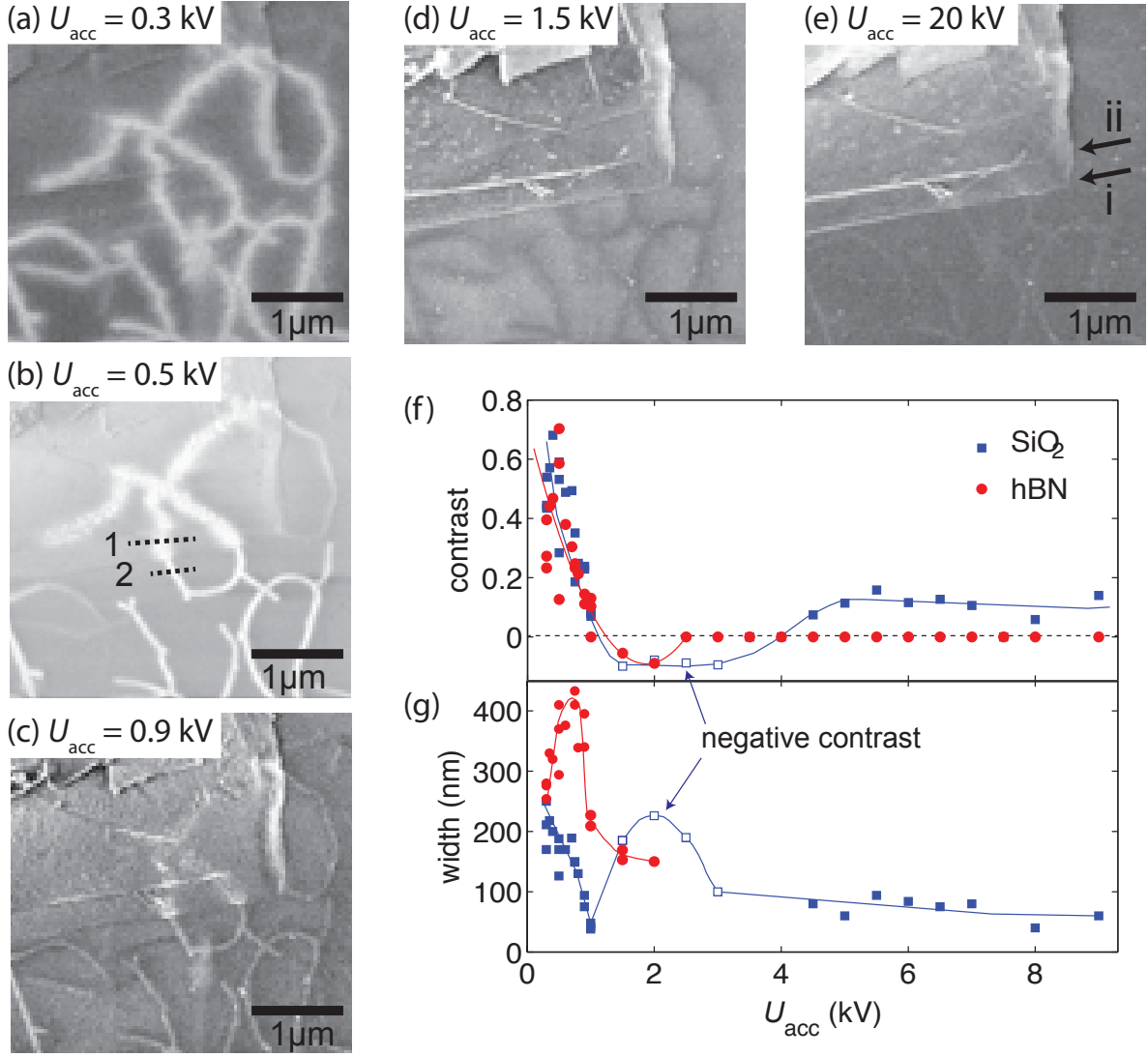


**Figure 4.1.** (a)-(e) SEM images of CNTs on an hBN flake for different SEM acceleration voltages  $U_{acc}$ . The thickness steps (i) and (ii) indicated in (e) are  $\sim 35$  nm and  $\sim 80$  nm, respectively. (f) SEM contrast and (g) apparent CNT width as a function of  $U_{acc}$  found in cross sections 1 and 2 indicated in (b). The continuous lines are guides to the eye.

insulating, the only mobile carriers are the electrons excited to the conduction band by the SEM beam, which leads to the so-called electron beam induced conductance (EBIC), well known from semiconductor device characterization. These carriers spread from the CNT due to the electric field, which depends on the material's dielectric constant (Mott-Gurney law), until they thermalize and localize in the dielectric. For positively charged substrates, this leads to a relative increase in the local electron density and an increase in the SE generation rate, while the opposite happens when the substrate is negatively charged. The difference in the apparent CNT widths on SiO<sub>2</sub> and hBN can now be understood qualitatively by noting that hBN has an anisotropic dielectric constant: the component perpendicular to the substrate plane is  $\epsilon_{perp} \approx 5$ , similar to SiO<sub>2</sub> ( $\epsilon \approx 4$ ),

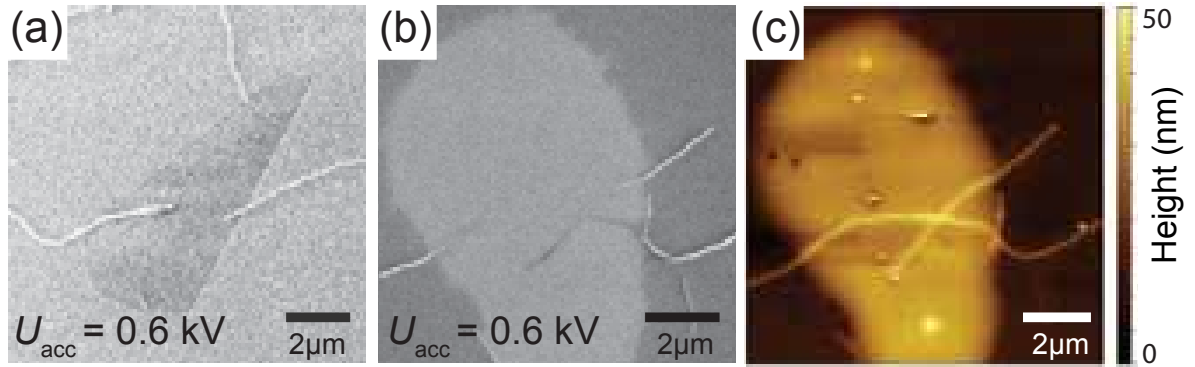


**Figure 4.2.** SEM images of CNTs on hBN. (a) Right tube:  $\sim 5.5$  nm radius, flake thickness  $\sim 6$  nm. (b) An  $\sim 8$  nm radius CNT spanning a  $\sim 30$  nm thick hBN flake. (c) AFM image corresponding to (b).

while the parallel component is  $\epsilon_{par} \approx 7$ , leading to an increased EBIC parallel to the surface compared to  $\text{SiO}_2$ . We note that for suspended CNTs or at higher acceleration voltages, other mechanisms might come into play, for example, the plasmon mediated generation of SEs [121].

### 4.3. Tunneling spectroscopy of a clean CNT QD on hBN

The structure of an hBN substrate supported CNT QD device is shown schematically in Fig. 4.3(a). We use a highly p-doped Si wafer with a thermally oxidized 300 nm thick insulation layer, which allows us to use the substrate as a back-gate. We deposit hBN flakes by mechanical exfoliation from a single crystal and achieve a moderate control over the thicknesses by adjusting the number of sequential exfoliation steps. We obtain a rough thickness estimate and fast feed-back using an optical microscope [122, 123]. Ru/Fe catalyst particles [124] are deposited on the wafer surface and on the hBN flakes by spin coating. The CNTs are grown at  $850^\circ\text{C}$  in a CVD process with methane as the source gas. Subsequently, 80 nm thick Pd contacts are fabricated by a standard electron beam lithography (EBL) using an optimized recipe for residue-free polymer removal [27].

In the device discussed here, the contact separation is  $L \approx 400$  nm on a CNT of  $r \approx 5.5$  nm radius on an hBN flake of  $\sim 6$  nm thickness. We apply a dc and an ac bias,  $V_{SD} + \delta V$ , and measure the differential conductance  $G = \delta I / \delta V$  of the device using standard lock-in techniques with an ac voltage of  $\delta V = 50 \mu\text{V}$  at a frequency of 130 Hz. The differential conductance of the device at 4.2 K (Helium bath) is plotted in Fig. 4.3(b) as a function of the back-gate voltage  $V_{BG}$  and the source-drain bias  $V_{SD}$ . Between the metal contacts, a QD forms which leads to clear Coulomb blockade diamonds and a series of resonances due to excited states. The dashed lines in the figure trace the edges of the Coulomb blockade diamonds and suggest a two-fold symmetry, as expected for clean CNT QDs due to the spin degeneracy in CNTs. The charging energy is  $E_C \approx 7.2$  meV, as indicated in Fig. 4.3(b), with a lever arm  $\alpha_{BG}$  similar to devices

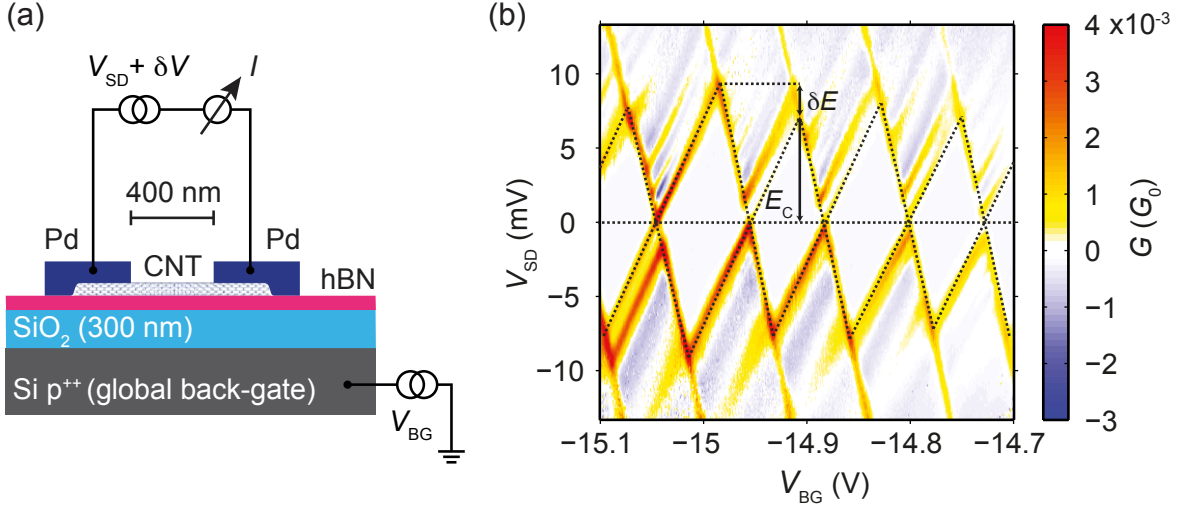


**Figure 4.3.** (a) Schematic illustration of the device structure and measurement set-up of an hBN substrate supported CNT QD device. (b) Coulomb blockade and excited states resonances in a CNT QD fabricated on top of an hBN flake ( $T = 4.2$  K).

on SiO<sub>2</sub>. From  $E_C = e^2/C_{\text{tot}}$ , we estimate the back-gate capacitance  $C_{\text{BG}} \approx \alpha_{\text{BG}} C_{\text{tot}}$ , which is in reasonable agreement with finite element method (FEM) calculations for a metallic cylinder with a length given by the contact distance [125]. This suggests that the QD confinement is determined by the metal contacts and not by defects in the CNT.

In Fig. 4.3(b), we observe up to the fifth excited state. The excited state energies  $\delta E$  are roughly equidistant and similar for all Coulomb diamonds. We find  $\delta E \approx 2.2$  meV by the difference in the addition energies of the individual Coulomb diamonds, as indicated in Fig. 4.3(b). Assuming a hard-wall confinement potential and a strong lifting of the sublattice band energies [126], the level spacing is given by  $\delta E = \hbar v_F / (2L)$ , with  $v_F \approx 8.1 \times 10^5$  m/s the Fermi velocity. This reproduces the experiment for  $L \approx 760$  nm, which is larger than the contact spacing.

We note that one finds finite-bias regions of negative differential conductance and that the ground state transitions are weaker in some Coulomb blockade diamonds than the excited state transitions. Both findings suggest that the tunnel coupling of the excited states to the leads can be stronger than of the ground state, which leads to a competition for the QD occupation by the individual transmission channels. The fact that such detailed excited state spectroscopy is possible also supports the claim that the QD are “clean” in the sense that no other electronic structures and resonances interfere with the ideal patterns. In addition, at low temperatures in vacuum, we reproducibly find a very good long term (>days) electrical stability, i.e., very few gate-dependent and no temporal charge rearrangements, comparable only to the best of our CNT QDs fabricated on SiO<sub>2</sub> substrates.

## 4.4. Electrical tunability of a dual-gated CNT QD with hBN top gate dielectric

The structure of a dual-gated CNT QD device made using hBN as an insulator for top finger gates, is schematically illustrated in Fig. 4.4. We use a heavily p-doped Si wafer that is capped by a 300 nm thick SiO<sub>2</sub> insulating layer. This allows us to use the substrate as a back-gate. We pattern the substrate with 5 nm/45 nm thick Ti/Au alignment markers and bond pads by electron beam lithography. The CNTs are stamped onto the substrate by means of mechanical stamping techniques [104], and a thin layer of Pd with a thickness of 20 nm is deposited to form the source-drain contacts. We place a freshly cleaved hBN flake on top of the CNT by employing an all-dry viscoelastic stamping technique [105]. The top-gate electrodes are fabricated on top of the flake by standard electron beam lithography. The device structure with measurement set-up is schematically shown in Fig. 4.4. The individual finger gate has a width of  $\sim 100$  nm, and the edge-to-edge distance between neighboring gates is also  $\sim 100$  nm. Figure 4.4(b) shows an SEM image of five finger gates fabricated on top of an hBN flake. These narrow finger gates are often ripped off during lift-off due to weak adhesion and thereby leading to broken top-gate electrodes as shown in Fig. 4.4(b). We speculate that hBN offers a clean surface that is not only free from dangling bonds and charge traps, but also free from contaminations that are often induced by the electron beam resist residues. However, this weak adhesion makes the realization of narrow finger gates on top of an hBN flake by standard electron beam lithography difficult and challenging.

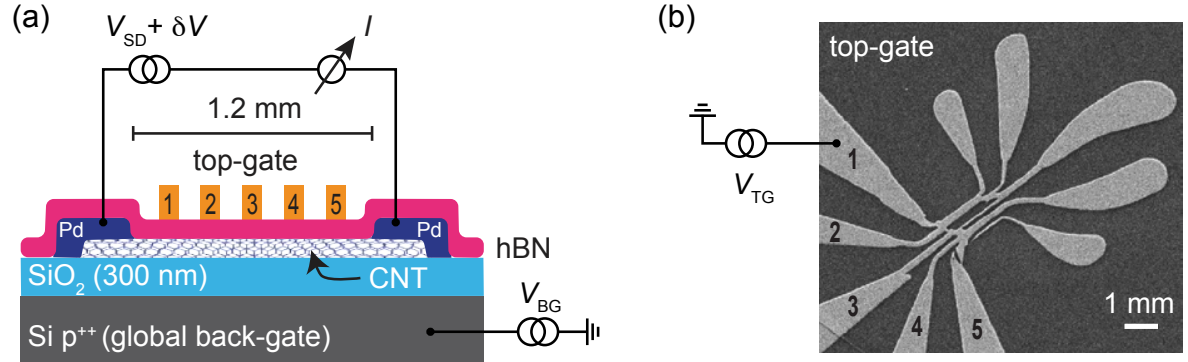


**Figure 4.4.** (a) Schematic illustration of the device structure with measurement set-up. (b) SEM image of the top-gate electrodes on an hBN flake.

In the device discussed here, the source-drain contact spacing is  $L \approx 1.2 \mu\text{m}$  under an hBN flake of  $\sim 60$  nm thick, and we label the top-gate electrodes by numbers, e.g., 1, 2, 3, 4, and 5. In Fig. 4.4(b), electrical shorts occur not only between the adjacent top-gate electrodes 1 and 2, but also between 3, 4, and 5, thereby forming two single gates with wider widths, i.e., TG<sub>12</sub> and TG<sub>345</sub>. For this work, TG<sub>345</sub> is kept grounded and will not be discussed further, while a top-gate voltage  $V_{\text{TG}}$  is applied to TG<sub>12</sub> to tune the electrostatic potential of the device.

Figure 4.5 shows the differential conductance  $G$  measured as a function of  $V_{\text{BG}}$  and  $V_{\text{SD}}$  at  $T = 240$  mK and  $V_{\text{TG}} = 0$  V. We observe Coulomb blockade diamonds and ex-

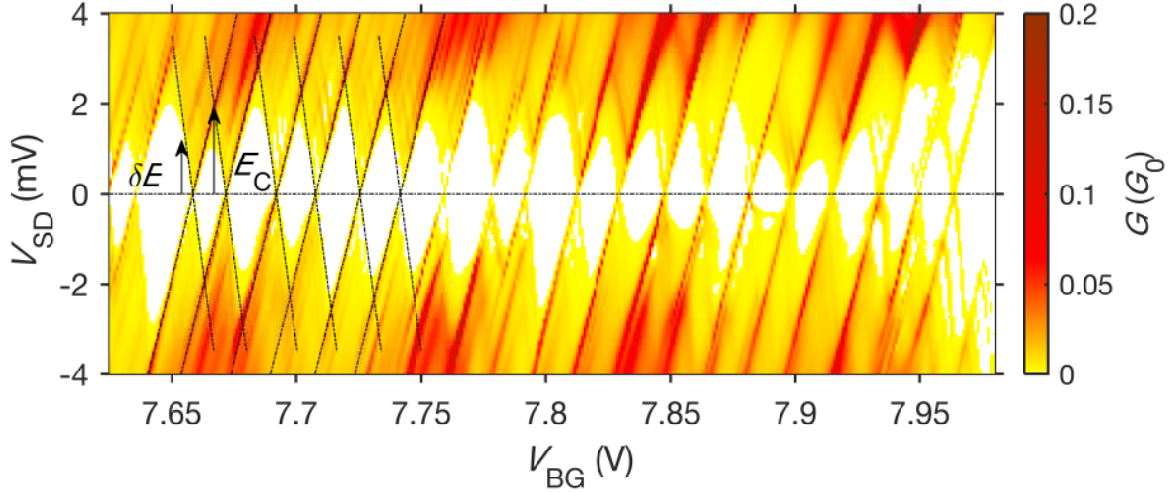


**Figure 4.5.** Coulomb blockade diamonds as a function of  $V_{\text{BG}}$  and  $V_{\text{SD}}$  at  $T = 240$  mK and  $V_{\text{TG}} = 0$  V.

cited state resonances, which indicate a single QD formed in the system. The dashed lines highlight the boundaries of the Coulomb blockade diamonds and suggest a two-fold symmetry. The expected four-fold symmetry is missing probably due to the valley degeneracy lifting through disorders or nonuniformity that are likely to present in the system. From the size of the Coulomb blockade diamonds, we can extract the charging energy and lever arm, i.e.,  $E_C \approx 1.9$  meV and  $\alpha_{\text{BG}} \approx 0.1$ , respectively, and from which we estimate a back-gate capacitance  $C_{\text{BG}} \approx 84$  aF. We obtain the excited state energy  $\delta E \approx 1.2$  meV by direct spectroscopy, as indicated in Fig. 4.5, and this number suggests a QD size of  $\sim 1.3$   $\mu\text{m}$ , in good agreement with the source-drain contact separation. This means that the QD is defined by the source-drain metal contacts and not by defects in the CNT. We deduce the tunnel coupling strength using the full-width at half-maximum (FWHM) of a zero-bias resonance, and it yields  $\Gamma \approx 450$   $\mu\text{eV}$ . Comparing to the extracted charging energy, the tunnel coupling strength is significant and thereby indicating a strong coupling to the source-drain contacts. We note that the result of forming a clean single QD with a size of  $1.3$   $\mu\text{m}$  is very promising. The fact that such a detailed transport spectroscopy of a  $\text{SiO}_2$  substrate supported CNT QD with no temporary charge rearrangements and specifically with a confinement size  $> 1$   $\mu\text{m}$  is possible supports the claim that placing hBN on top of the CNT protects the active structure from polymer contaminations, and thereby provides a disorder-free environment.

We now turn to the discussion of the electrical tunability of the device by top-gate electrodes. The use of both top-gate and back-gate electrodes allows us to control the energy levels of the QD and the electric field experienced by the CNT independently. In Fig. 4.6, we show the zero-bias differential conductance  $G$  of the device recorded as a function of  $V_{\text{BG}}$  and  $V_{\text{TG}}$  at  $T = 240$  mK. We observe Coulomb blockade resonance lines that are running parallel to each other with a close to uniform spacing, which is a characteristic behavior of single QDs. The dashed lines with different colors trace the positions of seven resonance lines that are next to each other, and we label them as

R1, R2, R3, R4, R5, R6, and R7. Each resonance line corresponds to an energy level on the QD, and its position is driven by the energy required for adding one additional electron to the QD, and this energy consists of components that are originating from both Coulomb charging and energy level quantization due to quantum confinement. This means that each resonance line shifts in position with applied  $V_{\text{BG}}$  and  $V_{\text{TG}}$ , and its slope gives the ratio between the back-gate and top-gate capacitances, e.g., for the resonance line R1, this yields  $C_{\text{BG}}/C_{\text{TG}} \approx 0.3$ .

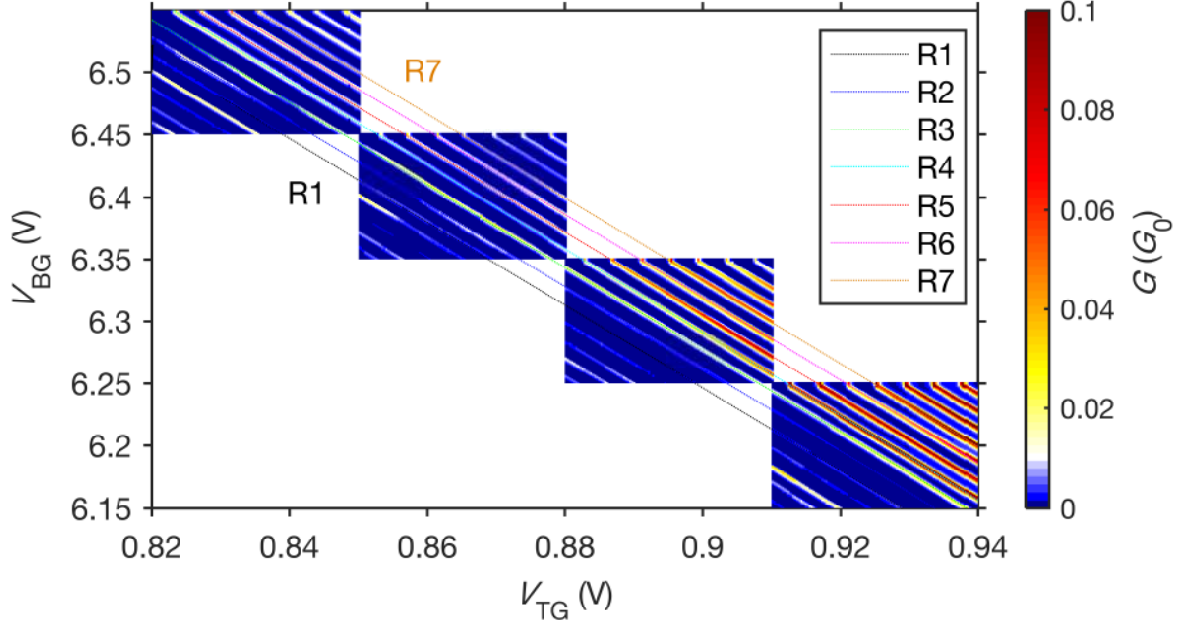


**Figure 4.6.** Zero-bias differential conductance  $G$  measured as a function of  $V_{\text{BG}}$  and  $V_{\text{TG}}$  at  $T = 240$  mK.

We note that we observe a non-monotonic modulation of the Coulomb blockade peak height along a resonance line as increasing  $V_{\text{TG}}$ . For instance, by following the resonance line R2 in Fig. 4.6, we find that the noticeable line structure at  $V_{\text{TG}} = 0.83$  V is first washed out as increasing the top-gate voltage to  $V_{\text{TG}} = 0.85$  V, and then it is well visible again at a higher voltage  $V_{\text{TG}} = 0.865$  V. This amplitude modulation can be understood by considering the strong coupling regime where the resonance line shape is given by the Breit-Wigner formula [127]:

$$G \propto \frac{4\Gamma_S\Gamma_D}{(\Gamma_S + \Gamma_D)^2} \quad (4.1)$$

The amplitude maximum of a zero-bias Coulomb blockade peak is determined by the asymmetry of  $\Gamma_S/\Gamma_D$ , which can be tuned by modifying the orbital part of an electronic wave function in the QD and thereby influencing the overlap between the QD and the contacts using both top-gate and back-gate voltages. Therefore, we ascribe the non-monotonic modulation of the resonance amplitude to the variation in the asymmetry of  $\Gamma_S/\Gamma_D$  induced by the dual-gate voltages.



## 4.5. Conclusions

In summary, we report detailed SEM imaging of CNTs on hBN that allows us to locate CNTs on hBN flakes. This is a fundamental prerequisite for a fast and reliable fabrication of standard top-down nanostructures, e.g., by electron beam lithography. We demonstrate a clean CNT QD on hBN for which we discuss the electronic structure that indicates a very good electrical device quality and stability. In addition, we report the low-temperature characteristics of a dual-gated CNT QD with hBN top-gate dielectric. We demonstrate the electrical tunability of the device by applying top-gate and back-gate voltages, and it reveals a characteristic behavior of a clean single QD with a quantum confinement size  $\sim 1.3 \mu\text{m}$ , which is a very encouraging result. We find that the gates not only tune the electrostatic potential of the QD, but also influence the tunnel coupling asymmetry of the QD and thereby giving rise to a non-monotonic modulation of the Coulomb blockade resonance amplitudes. This proof of concept paves the way to more complex devices based on hBN gate dielectrics, with more predictable and reproducible characteristics and electronic stability.



# 5 Characterization of carbon nanotube devices with hexagonal boron nitride tunnel barriers

---

A great deal of attention has been focused on tunneling transport and spectroscopy in CNT QDs, but our present knowledge of the nature of tunnel barriers is still far from sufficient. Tunnel barriers play a key role in both charge and spin transports in CNT-based quantum devices [128]. Our ability to control these tunnel barriers in terms of barrier heights and widths is essential for the realization of more advanced nano-electronic systems based on CNTs, especially in a reproducible manner. By placing metallic electrodes in contact with semiconducting CNTs, Schottky barriers can form at the interface between the CNTs and metal electrodes, but a full understanding of its formation mechanism is still lacking [54]. Other than the naturally formed Schottky barriers, bending defects or “kinks” induced by the tip of an AFM [129], and local damages induced by argon atom beam irradiation [130] have also been suggested to serve as tunnel barriers. Recently, hBN has emerged as an ideal dielectric barrier for graphene-based tunnel junctions [131, 132]. Specifically, tunneling behavior in atomically thin hBN has been observed in vertical graphene heterostructures [133–135]. We have demonstrated that thick hBN flakes can be used as clean substrates for CNT QDs [34], but the use of hBN as tunnel barriers to CNT devices has not been studied.

In this chapter, we present our experimental results from CNT devices made using CVD grown monolayer hBN films as tunnel barriers. In the first part of this chapter, we report the differential conductance measurements on a CNT device with two tunnel contacts and a global back-gate (BG) at cryogenic temperatures, for which we find two interpenetrating sets of Coulomb blockade (CB) diamonds with excited states and strong anti-crossings between specific resonances. These findings are consistent with two strongly coupled parallel QDs in a multi-wall or a tight double-stranded CNT bundle. This work has been published in a similar form in Ref.[35]. In the second part of this chapter, we focus on the CVD grown monolayer hBN film and its integration into the CNT devices as a tunnel barrier. We report that the hBN film quality degrades during the transfer process, as suggested by both optical and SEM images taken before and after the transfer process for comparisons. We place the CVD grown monolayer hBN film between the CNTs and source-drain electrodes, and the resulting devices all show hysteresis in the differential conductance versus BG characteristics at cryogenic temperatures. The zero-bias CB resonance shapes and the tunnel coupling parameters used for a best fit to the resonance shape suggest a strong coupling to the source-drain contacts, which seems to be quite contrary to our expectations.

## 5.1. Full characterization of a CNT parallel DQD

### 5.1.1. Introduction

Recently, CNTs have been used as central elements in a variety of novel electronic devices, owing to their unique electrical and mechanical properties and compatibility with various material types and experimental set-ups [1, 2, 136–139]. There are many different types of CNTs [2], for example, metallic or semiconducting CNTs. Single-wall CNTs (SWCNTs) are a single sheet of rolled up graphene, while multi-wall CNTs (MWCNTs) consist of several coaxial CNTs of different diameters [140, 141]. In contrast, CNT bundles are a set of separate non-coaxial CNTs in parallel. Long metallic SWCNTs are promising systems, for instance, to study 1D Luttinger liquids [12], or novel quasiparticles with non-Abelian statistics [142]. SWCNTs of finite length are very reliable in showing size quantization of the energy levels, shell filling effects, and CB in QDs. In comparison to QDs in SWCNTs, MWCNT QDs typically exhibit more complex electronic properties due to more available orbital states, which increase not only the number of conducting channels but also the possibility of intershell interactions [143].

Double QDs (DQDs) are versatile structures that exhibit many physically relevant phenomena [69]. DQDs in series between a source and a drain contact have been investigated regularly [144, 145], also in CNTs [146–148], for example, to investigate spin-blockade [149–151] and charge bits [152]. In parallel DQDs, CB suppresses the electronic transport only if both dots are in blockade. This allows in principle for a more detailed characterization of the individual QDs and the effects of the coupling between the QDs by first order transport processes. However, parallel DQDs are investigated less frequently [153] and are more difficult to obtain on CNTs than DQDs in series because of the close proximity between two CNTs that is required to obtain an appreciable tunnel coupling. Parallel DQDs can in principle form in MWCNTs, where separate QDs might form on different shells, or in non-overlapping parallel CNTs in a bundle, as depicted in Fig. 5.1(a) and Fig. 5.1(b), respectively. However, if the tunnel coupling is very strong, we expect that the QD states are strongly hybridized and result in the increased degeneracies and shell filling effects typical for MWCNTs [154, 155]. In contrast, for very small couplings between the concentric CNTs, two individual QD characteristics are expected. For intermediate couplings, one might expect a hybridization that retains most of the characteristics of the individual QD states, while a pronounced anti-crossing occurs when two charge states become degenerate. Recently, anti-crossings have been observed in a CNT bundle [156], where two or more QDs of very different characteristics have formed. It is difficult in CNT DQDs to gate the QDs individually, so that the DQD characteristics have to be observed in the conductance measured as a function of the bias and a global BG.

Here, we report the differential conductance of a parallel CNT DQD with strong inter-dot capacitance and inter-dot tunnel coupling. Nominally, the device consists of a single CNT with two contacts. However, we identify two sets of CB diamonds that do not block transport individually, which suggest that two QDs are contacted in parallel. We find strong and periodic anti-crossings in the gate and bias dependence, which are only possible if the QDs have similar characteristics. We discuss qualitatively the level spectrum and the involved transport processes in this device and extract the DQD

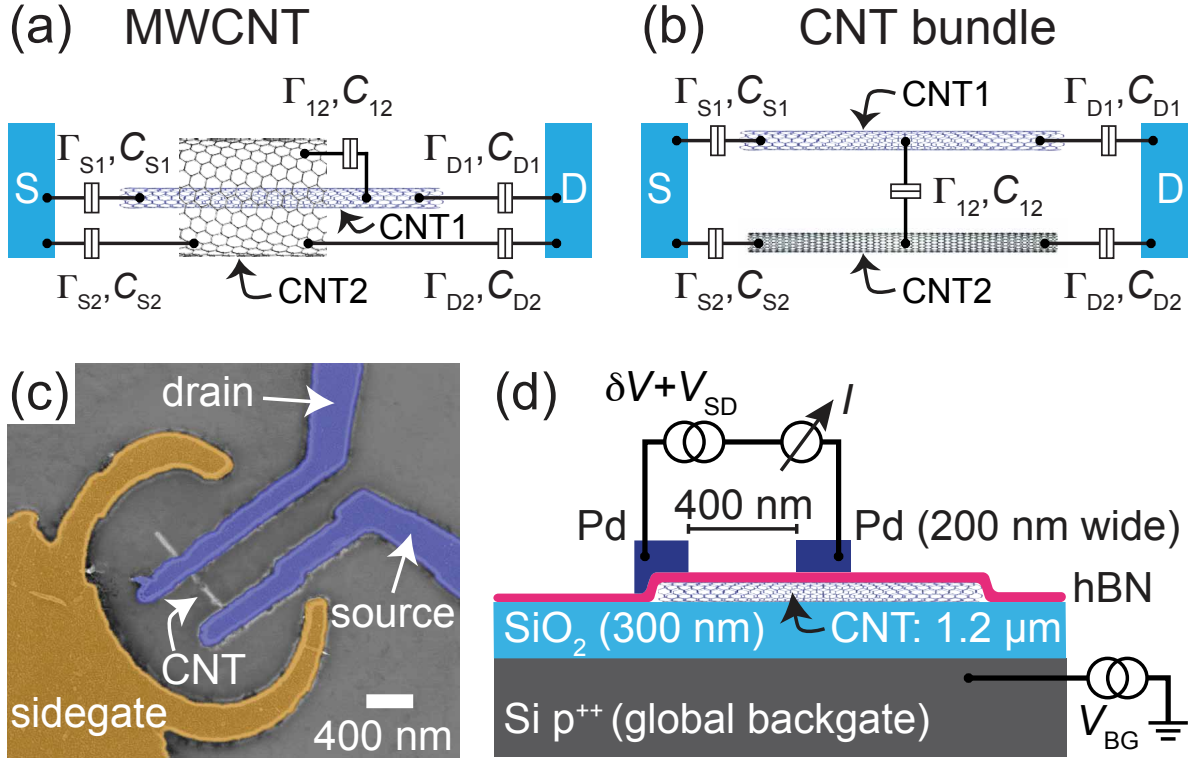


**Figure 5.1.** Schematic illustration of a parallel-coupled DQDs formed (a) in a MWCNT, or (b) in a CNT bundle. (c) False-color SEM image of a two-terminal CNT device. The CNT is connected to the source and drain electrodes shown in blue and the sidegate shown in orange. (d) Schematic device cross section illustrating the device geometry and electronic set-up.

coupling parameters. These results lead us to believe that clean and undoped QDs are formed parallel to the CNT axis, possibly on the outer and inner shells of a multi-wall CNT, or in a double-stranded CNT bundle.

### 5.1.2. Device and measurement set-up

CNTs on substrates often suffer from potential variations on the substrate or residues from the contact fabrication after the CNT growth [27, 157] and cannot be cleaned by current annealing. Here, we employ a stamping method in which CNTs are grown on a separate wafer [26, 104] and are later transferred mechanically to the device substrate. The key advantage of CNT stamping techniques is to separate the CNT growth from the fabrication of markers and bond pads [158]. A monolayer CVD grown hBN is transferred on top of the CNTs to form a tunnel barrier between the CNTs and the metallic leads. We note that by depositing the hBN layer directly onto the stamped CNTs protects the CNTs from direct exposure to the resist or solvents, which would otherwise contaminate the active structure [34, 47].

The device fabrication starts with the manufacturing of the CNT stamps. A Si substrate capped by a thermal oxide ( $\text{SiO}_2$ ) layer is patterned into an array of square mesas using electron-beam lithography. Each mesa is  $50 \mu\text{m}$  long and wide and  $4 \mu\text{m}$

high, with a spacing of  $50\ \mu\text{m}$  between neighboring squares. After spin coating of Mo/Fe catalyst particles onto the mesas, we grow CNTs at  $950\ ^\circ\text{C}$  for 10 min in a CVD process with methane as carbon precursor gas. The target substrate is a piece of a heavily p-doped Si wafer with 300 nm thick  $\text{SiO}_2$  on top, which acts as a global BG. This substrate is patterned with 5 nm/45 nm Ti/Au markers and bond pads. We then transfer the CNTs from the mesa substrate onto the target substrate using a mask aligner, by which the mesa and the target substrates are roughly aligned using the markers and pressed together. About 6 – 10 CNTs are transferred to a  $200 \times 200\ \mu\text{m}^2$  area on average. We locate the CNTs using an SEM [34]. Immediately after this step, a monolayer CVD hBN (from Graphene Supermarket) is transferred by a wet-etch process from its growth substrate (a copper foil) to the target substrate [159] with the CNTs below. Thermal annealing at  $200\ ^\circ\text{C}$  for 2 h removes the poly(methyl methacrylate) (PMMA) resist residues on top of the transferred hBN layer [114]. Suitable CNTs are then contacted by 10 nm/50 nm Cr/Pd source and drain contacts using electron-beam lithography.

An SEM image of the resulting device is shown in Fig. 5.1(c), and a schematic cross-section with details of the device geometry and the electrical measurement set-up is shown in Fig. 5.1(d). A  $1.2\ \mu\text{m}$  long CNT is contacted by 200 nm wide electrodes, separated by 400 nm. One contact (source) covers the end of the CNT, while the other (drain) does not. In this device a circular side-gate (SG) is fabricated in the same step for additional tunability. The SG voltage is kept constant for this work and will not be discussed further.

### 5.1.3. Bias spectroscopy and avoided crossings

At room temperature, the device has a resistance of  $5\ \text{M}\Omega$  for negative gate voltages (e.g.,  $V_{\text{BG}} \approx -2\ \text{V}$ ). Low-temperature transport properties are characterized in a  $^3\text{He}$  refrigerator at a base temperature of  $\sim 245\ \text{mK}$ . We apply a dc and an ac bias,  $V_{\text{SD}} + \delta V$ , to one contact (source) and measure the differential conductance  $G = \delta I / \delta V$  of the device using standard lock-in techniques with an ac voltage of  $\delta V = 40\ \mu\text{V}$  at a frequency of 328 Hz, as illustrated in Fig. 5.1(d). Figure 5.2(a) shows a colorscale plot of  $G$  as a function of  $V_{\text{BG}}$  and  $V_{\text{SD}}$ . We find a periodic pattern of strongly distorted CB diamonds, suggesting the formation of QDs in the CNT. While the weak CB diamond boundaries with positive slopes are straight, the ones with negative slopes consist of a series of avoided crossings. These lines have a larger amplitude, especially at larger bias, can be rather wide and can even occur in pairs.

To characterize the QDs formed in the device, we focus on the region pointed out by the dashed rectangle, with the corresponding data replotted in Fig. 5.2(b), while in Fig. 5.2(c) the positions of the resonances R1, R2, and R3 of Fig. 5.2(b) are plotted as solid red lines. First, we identify individual CB diamonds and ignore the avoided crossings and other effects discussed below. For this, we extrapolate the resonance position around zero bias, which results in the dashed black and blue diamonds. This two-QD pattern is shown exemplarily in Fig. 5.2(c), but also describes roughly the extended data set of Fig. 5.2(a). We therefore conclude that two QDs are formed in the system.

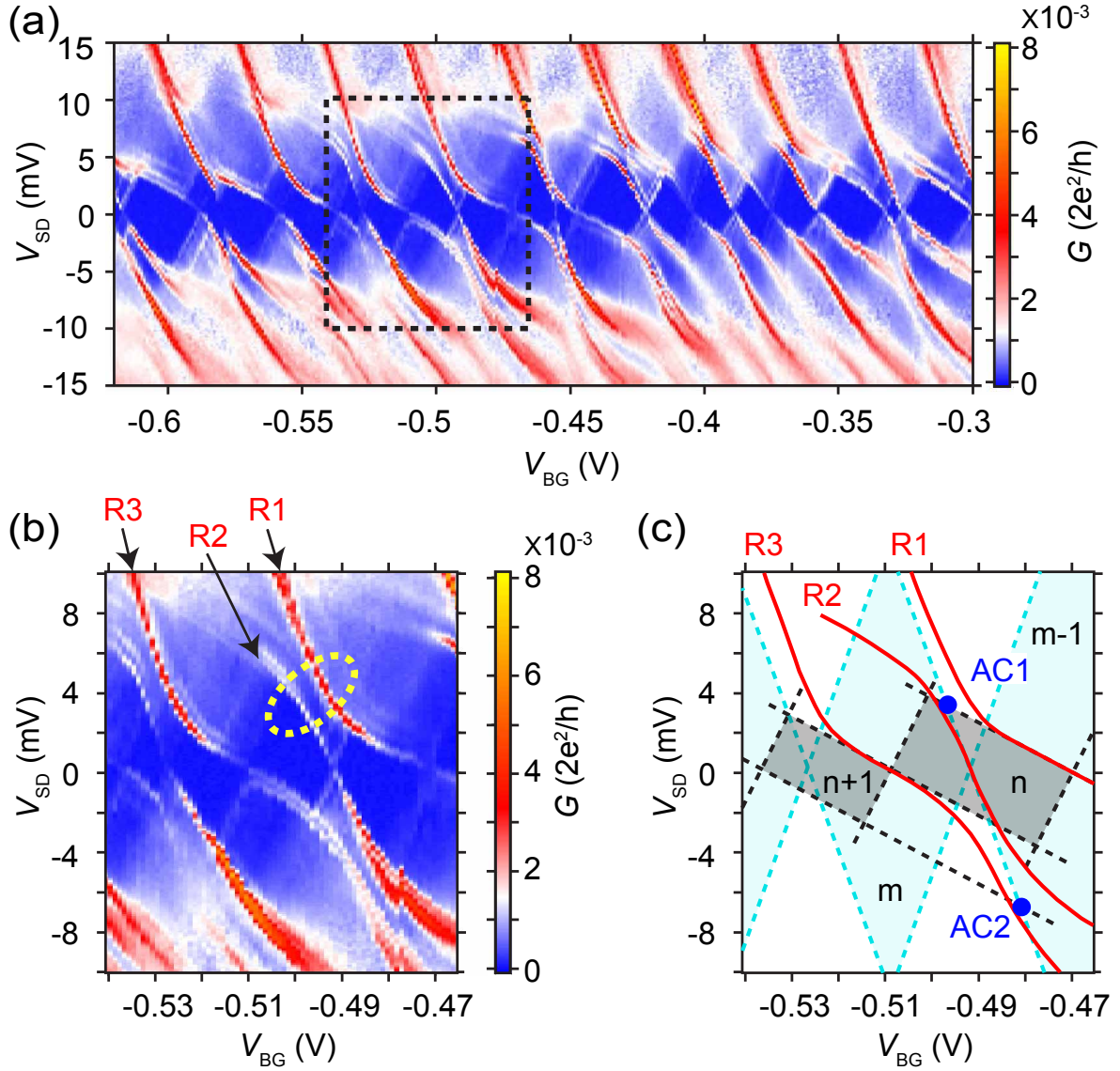


**Figure 5.2.** (a) Colorscale plot of the differential conductance  $G$  as a function of  $V_{BG}$  and  $V_{SD}$  for a fixed SG voltage  $V_{SG} = -2$  V and at  $T = 245$  mK. (b) Magnification of the region indicated in Fig. 5.2(a). Three resonances are labeled as R1, R2, and R3. The yellow-dashed ellipse highlights an avoided crossing. (c) Schematic charge stability diagram of the parallel DQDs extracted from Fig. 5.2(b). The three solid red lines correspond to the transport resonances (R1, R2, and R3) marked in Fig. 5.2(b) and the dashed lines are the extrapolated lines that separate the charge states of the individual QDs. AC1 and AC2 point out two avoided crossings, while  $n$  and  $m$  are the number of holes in the respective charge states.

From these extrapolated CB diamonds, we estimate the charging energies of the two individual QDs as  $E_{C1} \approx 10.4$  meV and  $E_{C2} \approx 3.0$  meV, which correspond to the total capacitances  $C_{tot1} \approx 15$  aF and  $C_{tot2} \approx 53$  aF, respectively. We label the QD with the larger charging energy as QD1 and the other as QD2. In the constant interaction model [66], the positive and negative slopes of an individual CB diamond are given

by  $+\frac{C_{\text{BG}}}{C_{\text{tot}}-C_{\text{S}}}$  and  $-\frac{C_{\text{BG}}}{C_{\text{S}}}$ , with  $C_{\text{tot}} = C_{\text{BG}} + C_{\text{S}} + C_{\text{D}}$ . From these expressions, we obtain the capacitances listed in Table 5.1 for the individual QDs. Here, we neglect the inter-dot capacitance, which might explain the small discrepancies in the sums from the measured  $C_{\text{tot}}$ . We find very similar values for the capacitive coupling of the drain to both QDs, for the BG to both QDs, and for the source to QD1. However,  $C_{\text{S}}$  of QD2 is about eight times larger, possibly related to the fact that this is the contact that overlaps the end of the CNT. We note that both BG capacitances are virtually identical. In addition, we can use the full-width at half-maximum of the zero-bias resonances as upper limits for the tunnel coupling strengths, yielding  $\Gamma_1 \leq 460 \mu\text{eV}$  and  $\Gamma_2 \leq 305 \mu\text{eV}$ , respectively. Figure 5.2(a) also shows excited state resonances, which run in parallel to the CB diamond boundaries. These lines are most pronounced for the resonances with negative slopes, which suggest fairly asymmetric tunnel barriers [66]. We extract the mean energy difference between these resonances as  $\delta E \approx 0.9 \text{ meV}$ . If we assume the confinement length  $L$  to be the 400 nm spacing between the source and drain electrodes, we expect a mean level spacing  $\delta E = \hbar v_{\text{F}}/2L \approx 4 \text{ meV}$  for an ideal and undoped metallic CNT, with  $\hbar$  the Plank constant and  $v_{\text{F}} = 8.1 \times 10^5 \text{ m/s}$  the Fermi velocity [160]. This expected value is a factor of four larger than the energy difference between the excited states in Fig. 5.2(a), suggesting both QDs are considerably larger than the contact spacing. Though we might overestimate the level spacing in case of a semiconducting CNT because of the flat electronic band structure close to the band gap [161], we speculate that by introducing a monolayer hBN tunnel barrier between the selected CNT and the metal contacts, it is possible that a larger QD forms on the significantly longer CNT, because the contacts are weakly coupled and do not necessarily result in electron confinement. As a result, the QD wave function can extend beyond the spacing between the source and drain contacts for weakly coupled tunnel contacts (hBN layer).

We now turn to the discussion of the avoided crossings shown, for example, in Fig. 5.2(b), where the avoided crossing AC1 is highlighted by a yellow-dashed ellipse. An avoided crossing is observed at the intersection points between the CB diamond boundaries of QD1 and QD2 with negative slopes. This can be understood easily by considering that at these points the chemical potentials (“resonances”) of both QDs would both be aligned with the electrochemical potential of the drain ( $\mu_{\text{D}} = 0$ ), which means that both QD potentials are identical and electrons (or holes) can be exchanged not only with the leads, but also between the QDs. This results in a

**Table 5.1.** Extracted parameters for QD1 and QD2

parameters	QD1 (blue lines)	QD2 (black lines)
$C_{\text{tot}}$	15.3 aF	53.3 aF
$C_{\text{BG}}$	5.0 aF	5.3 aF
$C_{\text{S}}$	8.1 aF	41.0 aF
$C_{\text{D}}$	2.6 aF	6.0 aF
$\Gamma$	460 $\mu\text{eV}$	305 $\mu\text{eV}$
$C_{12}$		$\sim 5 \text{ aF}$
$\Gamma_{12}$		$\geq 500 \mu\text{eV}$



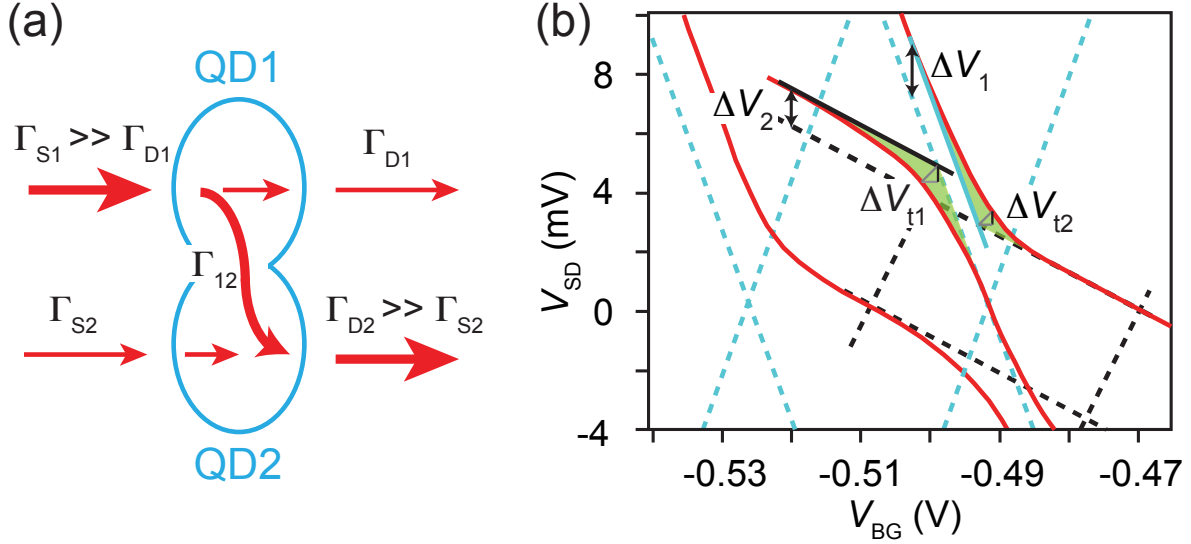


**Figure 5.3.** (a) Schematic sequential tunneling through a strongly coupled DQD. This is for a specific point AC1 (or AC2) near the avoided crossing shown in Fig. 5.2(c). (b) Replot of the charge stability diagram in Fig. 5.2(c) with the focus on the avoided crossing AC1 discussed in the text.

hybridization of the QD wave functions and an avoided crossing in their spectrum. The increased resonance amplitudes can be understood qualitatively in the sequential tunneling picture by considering the case  $\Gamma_{12} \gg \Gamma_j$ , where  $j$  stands for all the contacts. As illustrated in Fig. 5.3(a), the DQD then acts like a single QD with four leads. In addition to the paths through the individual QDs, electrons (or holes) can also tunnel into one QD and out of the other, which can result in more than the sum of the currents through the individual QDs. The total tunneling rate reads  $\Gamma = (\Gamma_{S1} + \Gamma_{S2})(\Gamma_{D1} + \Gamma_{D2})/\Gamma_{\Sigma} = (\Gamma_{S1}\Gamma_{D1} + \Gamma_{S2}\Gamma_{D2} + \Gamma_{S2}\Gamma_{D1} + \Gamma_{S1}\Gamma_{D2})/\Gamma_{\Sigma}$  with  $\Gamma_{\Sigma} \approx \Gamma_{S1} + \Gamma_{S2} + \Gamma_{D1} + \Gamma_{D2}$ . The first two terms are essentially the individual QD transmissions, which are dominated by the last two terms for the situation of very asymmetric couplings shown in Fig. 5.3(a). We would in principle expect a similar effect for the CB resonances with positive slopes (the dot potentials aligned with the source Fermi energy). However, since the two positive slopes are very similar, no such crossing is observed on this device.

To characterize the avoided crossings, we replot the positions of the three resonance curves R1, R2, and R3 in Fig. 5.3(b) and focus on the avoided crossing AC1. We now draw the asymptotes to the resonances away from AC1. Two lines are the CB diamond edges found above, but the other two are offset in bias by  $\Delta V_1$  and  $\Delta V_2$ , respectively. These offsets are in analogy with the zero-bias gate maps in more standard, separately gated DQDs in series [69]. The offsets are due to one QD capacitively sensing the charge state of the other, while the bending of the resonances, indicated as green shadings in Fig. 5.3(b), stems from the inter-dot tunnel coupling. We first extract the inter-dot capacitance  $C_{12}$  from the resonance offsets: the addition of one electron to QD  $i$  results in a change of the electrical potential in QD  $j$ ,  $\Delta\Phi_j$  (and vice versa), due to the capacitive coupling. For  $C_{12} \ll C_{\text{tot}1}, C_{\text{tot}2}$ , one finds  $\Delta\Phi_j = \frac{e^2}{C_{\text{tot}i}C_{\text{tot}j}}C_{ij}$ . This

shift in the potential has to be compensated by a change  $\Delta V_{\text{SD}}^{(j)}$  in the bias measured between the two asymptotes corresponding to QD  $j$ . For the drain resonance, one obtains  $0 = \Delta\Phi_j + e\alpha_{\text{S}j}\Delta V_{\text{SD}}$  with the source lever arm  $\alpha_{\text{S}j} = \frac{C_{\text{S}j}}{C_{\text{tot}j}}$ . From this, one directly obtains:

$$C_{ij} = -\frac{C_{\text{tot}i}C_{\text{S}j}}{e}\Delta V_{\text{SD}}^{(j)} \quad (5.1)$$

Similarly, from the the resonance condition at the source contact,  $e\Delta V_{\text{SD}}^{(j)} = \Delta\Phi_j + e\alpha_{\text{S}j}\Delta V_{\text{SD}}^{(j)}$ , one then obtains:

$$C_{ij} = \frac{1}{e}C_{\text{tot}i}(C_{\text{tot}j} - C_{\text{S}j})\Delta V_{\text{SD}}^{(j)} \quad (5.2)$$

Inserting the experimental values for the offsets  $\Delta V_{\text{SD}}^{(j)}$  and the capacitances in Table 5.1, we find consistently for both QD resonance lines at AC1 the inter-dot capacitance  $C_{12} \approx 5$  aF. Interestingly, this value varies between 5 aF and 9 aF for four neighboring avoided crossings, which might be either due to other crossings nearby (here, for example, AC2), or a deeper reason, possibly due to the QD quantum capacitance that might change with the charge and orbital states, and with the bias. The extracted value is comparable to the gate and contact capacitances, so that this value has to be taken as an approximation.

We estimate the inter-dot tunnel coupling strength by considering only the bias component of the bending,  $\Delta V_t$ , as illustrated in Fig. 5.3(b). This results in a lower limit for the tunnel coupling,  $\Gamma_{12} \geq 500 \mu\text{eV}$ . We note that we find a rather large variation ( $\sim 20\%$ ) between the extracted values for different avoided crossings, which probably originates from errors in the asymptotic lines. We point out that this value is of similar strength as the total tunnel coupling to the leads.

One might expect that with the inter-dot coupling parameters, one should be able to distinguish whether the DQD is formed on two shells of a MWCNT or on two separate CNTs in a bundle, see Fig. 5.1(a) and Fig. 5.1(b), respectively. The expressions for the capacitances of two parallel or coaxial cylinders at a distance compatible with a large inter-dot tunnel coupling (few nanometers) both suggest unphysically small CNT diameters. The reason for this is that the source and drain contacts reduce the inter-dot capacitance due to screening, which can only be accounted for numerically [34]. However, two parallel CNTs in a bundle would naturally account for the identical gate capacitances of the two QDs.

#### 5.1.4. Conclusions

In summary, we report the low-temperature differential conductance measurements on parallel DQDs, formed on two shells of a MWCNT or on two individual CNTs of a bundle. We investigate avoided crossings that result from the tunnel and capacitive couplings between the electronic charge states of different QDs. Our results enrich the fundamental understanding of quantum transport through coupled QDs formed in a parallel configuration. We demonstrate that in the sense of the simplest DQD model (large level spacing and constant interaction), transport spectroscopy can be used as a

sensitive tool to fully characterize the interactions between parallel-coupled QDs also in a two-terminal CNT device with only a single global gate.

We note that a CNT with direct clean metal contacts, e.g. Pd, often forms QDs of the size determined by the metal contact spacing [34], or, in a disordered CNT, by defects and potential fluctuations. In such a system, assuming  $\delta E = hv_F/2L$ , for a QD of  $\sim 400$  nm size, one expects a level spacing of  $\sim 4$  meV. However, by placing hBN as a tunnel barrier to the CNT, we expect to observe a larger QD, which is not confined by the metal contacts. The transport spectroscopy of our parallel DQDs reveals a level spacing of  $\delta E \approx 0.9$  meV for both dots, which suggests that both QDs are considerably larger than the contact separation. This finding is in agreement with our expectations.

We also note that by introducing hBN as a tunnel barrier to the CNT, we hope to obtain a device with a small tunnel coupling strength of  $\Gamma \leq 100 \mu\text{eV}$ . However, our parallel DQDs show tunnel coupling strengths of  $\Gamma_1 \approx 460 \mu\text{eV}$  and  $\Gamma_2 \approx 305 \mu\text{eV}$  for QD1 and QD2, respectively, and these numbers are comparable to those of conventional devices without hBN tunnel barriers. We speculate that since the hBN layer thickness is small, the main effect is to reduce the adhesion of residues on the hBN, rather than to increase the distance between the CNT and the scatterers on the surface. However, this speculation raises an important question of whether we can identify and confirm the presence of hBN tunnel barriers in the system. In the following section, we try to answer this question by studying monolayer hBN films that are CVD grown on different substrates with a focus on their quality and integration into our CNT devices.

## 5.2. Towards clean and large scale hBN

### 5.2.1. Introduction

There has been a growing interest in hBN due to its promising properties, such as high thermal conductivity [48], excellent chemical stability [162], and atomically flat and chemically inert surfaces with few or no dangling bonds and charge traps [44]. hBN has a layered structure that is similar graphite. The boron and nitrogen atoms in each layer are bounded by a strong covalent bond of  $sp^2$ , while the different layers are held together by weak Van der Waals forces. However, unlike graphite, which is essentially a gapless semiconductor, hBN is an insulator with a large band gap of  $\sim 6$  eV [45]. hBN can be integrated into electronic devices, but requires our ability to isolate and transfer it with desired number of layers. On the one hand, mechanical cleavage of hBN from single crystals produces sufficiently large flakes with different number of layers, but the atomically thin flakes are difficult to identify by optical microscopy because of the low white light contrast of  $< 1.5\%$  on a 300 nm thick  $\text{SiO}_2$  [163] substrate. On the other hand, a significant amount of effort has been made to grow large area and high quality hBN films with controllable number of layers [164, 165]. Atomically thin films can be grown on Cu foils via a CVD method and subsequently transferred onto a  $\text{SiO}_2$  [50] substrate. However, the growth of atomically thin films directly on a desired substrate, e.g.,  $\text{SiO}_2$ , has not been developed yet. In this context, realization of high quality CNT devices on  $\text{SiO}_2$  substrates with hBN as ultra thin insulating layers depends not only on the as-grown film quality but also on the transfer techniques.

We employ CVD grown monolayer hBN films as atomically thin tunnel barriers for our CNT devices. Both the films grown on Cu foils and the ones synthesized on Fe foils [51] are investigated. Depending on the growth substrates, different techniques are adopted to transfer the film from its growth substrate onto a desired substrate, i.e., SiO<sub>2</sub>. We demonstrate that the films transferred from the Fe foils show a relatively better quality than the ones from the Cu foils. We integrate the hBN films into our CNT devices as tunnel barriers and characterize the electrical transport properties of the resulting devices at cryogenic temperatures.

### 5.2.2. Challenges with hBN film quality and transfer methods

#### hBN on growth substrates

Monolayer hBN films synthesized on polycrystalline Cu foils by CVD are purchased directly from Graphene Supermarket. We receive two batches in succession and label them as “old” and “new” batches. Figure 5.4 shows the optical microscopy images taken before and after a heat treatment at 300°C for 3 minutes, and from which we can qualitatively characterize the film coverage. We find that the polycrystalline Cu foil oxidizes after the heat treatment and leads to bright colors under the optical microscope due to interference effect, as shown in Fig. 5.4(b). If the Cu foil is uniformly covered by hBN, its surface is protected from the air, and thereby oxidation can be prevented. On the contrary, our study shows that oxidation takes place all over the Cu surface and suggests a poor film coverage.

(a) before heat treatment



(b) after heat treatment

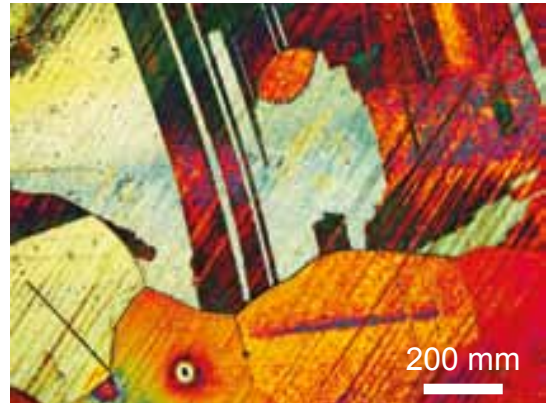


**Figure 5.4.** (a) Optical microscopy image of a CVD grown monolayer hBN film on a Cu foil before and after a heat treatment. The color contrast is enhanced for a better visibility.

Except the poor film coverage, we also find that the local film quality varies significantly from one batch to another, as confirmed by the SEM images shown in Fig. 5.5(a)-5.5(b). The sample from the “old” batch shows a large amount of particle residues, as indicated by the yellow circles in Fig. 5.5(a). We speculate that these particle residues are catalyst particles used for the CVD growth of hBN. In contrast, the sample from the “new” batch in Fig. 5.5(b) shows no particle residues and an average grain size of

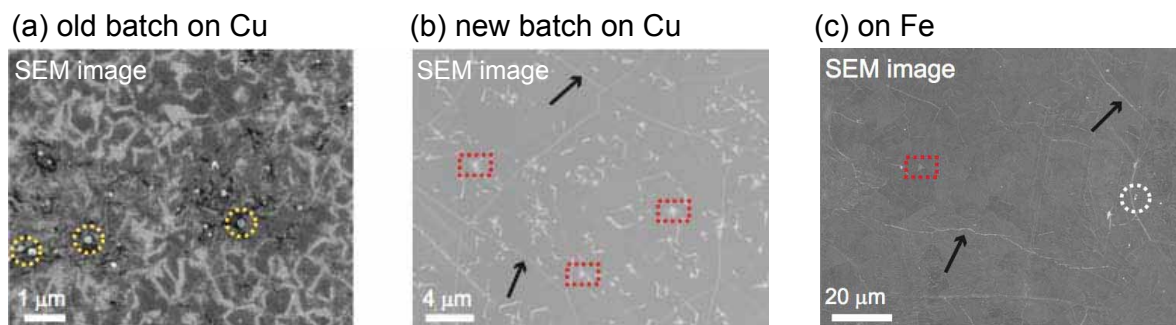


**Figure 5.5.** SEM images of hBN films on different growth substrate. (a) A sample from the old batch grown on a Cu foil. The yellow dashed circles highlight the catalyst particles. (b) A sample from the new batch grown on a Cu foil. The black arrows indicate the grain boundaries of the film. The red dashed rectangles point out the multilayer hBN islands. (c) A sample grown on an Fe foil. The white dashed circle and the black arrows highlight the catalyst particles and the grain boundaries, respectively.

$\sim 10 \mu\text{m}$ . In this figure, the bright contrast areas highlighted by the red dashed rectangles correspond to the island structures of multilayer hBN. Compared to the “old” batch, the “new” batch demonstrates a better film quality considering the number of particle residues, the average grain size, and the uniformity of the film thickness. However, we often obtain irreproducible results due to the quality variation from one sample to another. As a result, we move to hBN films that are grown on Fe foils using a new method by our collaborator (Stephan Hofmann’s research group) [51]. As shown in Fig. 5.6(a), the hBN film on an Fe foil displays a very promising quality, especially in terms of the thickness uniformity, average grain size, and most importantly the sample reproducibility.

### hBN on $\text{SiO}_2$

For films grown on Cu foils, we use a wet-etch process to remove the Cu [159], while, for the ones synthesized on Fe foils, we employ an electrochemical bubbling method to mechanically separate them from the Fe [110]. We highlight that both techniques involve PMMA as a supporting layer that is spin-coated on the film. In Fig. 5.6, we show the optical microscopy images of hBN films that are transferred onto the  $\text{SiO}_2$  substrates. In these figures, we find a number of large holes, and we speculate that a small amount of water may have been trapped between the hBN and the substrate during the transfer, and could cause holes after the removal of PMMA [166]. The AFM image in Fig. 5.6(b) suggests a film thickness up to 8 nm, which is at least 10 times larger than the value expected for a monolayer. This can be explained by considering layers of PMMA residues that may remain on the film surface due to its incomplete removal in acetone. We ascribe the enhanced optical visibility and the unexpected film thickness non-uniformity to the left over PMMA residues. We note that no matter which transfer method is chosen, the overall film quality degrades during the transfer process. This means that an improvement of our transfer techniques is required, if we want to maintain the high quality of the as-grown hBN film during its transfer onto our desired target substrates.

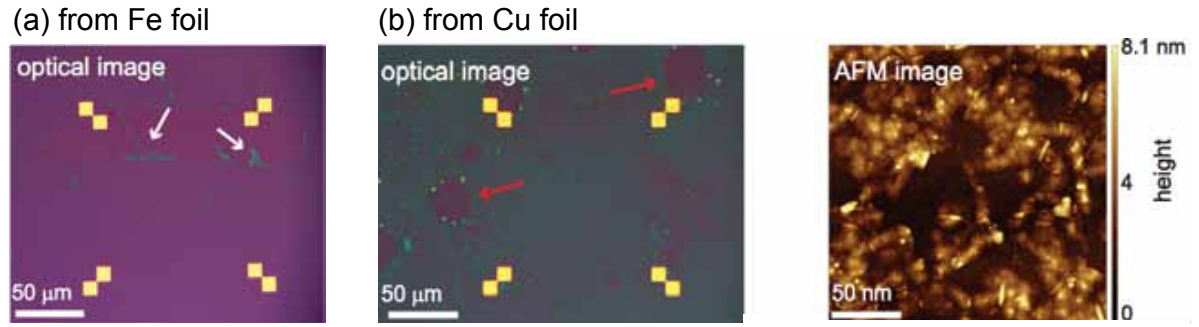


**Figure 5.6.** (a) Optical microscopy image of a CVD grown monolayer hBN film transferred from an Fe foil onto a  $\text{SiO}_2$  substrate. The white arrows indicate the boundary of the holes. (c) Optical microscopy and AFM images of CVD grown monolayer hBN films transferred from Cu foils onto  $\text{SiO}_2$  substrates. The red arrows point out the area with large holes.

### 5.2.3. Integration of monolayer hBN into CNT devices

Integration of monolayer hBN films into our CNT devices is realized by placing the film between the CNT and the source-drain contacts. We transfer the hBN film from its growth substrate onto the target substrate with CNTs below, and then deposit source-drain electrodes by electron-beam lithography. At room temperature, 20 out of 23 working devices made with films transferred from Cu foils show two-terminal resistances within the range of  $250 \text{ k}\Omega \leq R \leq 5 \text{ M}\Omega$  at  $V_{\text{BG}} = 0 \text{ V}$ . In contrast, 16 out of 21 working devices made with films transferred from Fe foils show two-terminal resistances of  $R \leq 100 \text{ k}\Omega$  at  $V_{\text{BG}} = 0 \text{ V}$ . As we have discussed earlier, compared to the monolayer hBN films transferred from the Cu foils, the ones transferred from the Fe foils show cleaner surfaces with less PMMA residues. If the interface between the CNT and the source-drain contacts is contaminated by PMMA residues, one would expect a two-terminal resistance that is higher than that of a device with clean interface. In the following section, we characterize our CNT devices with the hope to identify the hBN tunnel barriers.

#### Large hysteresis

The structure and measurement set-up of a three-terminal CNT device with tunnel contacts is shown in the inset of Fig. 5.7, where a  $1.2 \mu\text{m}$  long CNT is contacted by  $200 \text{ nm}$  wide electrodes. The distance between the left and middle contacts (inside edge to inside edge) is  $\sim 180 \text{ nm}$ , while the spacing between the middle and right electrodes (inside edge to inside edge) is  $\sim 120 \text{ nm}$ . At room temperature, the device has a resistance of  $\sim 30 \text{ k}\Omega$  between the middle and left electrodes at  $V_{\text{BG}} = 0 \text{ V}$ , while the resistance between the middle and right electrodes is  $\sim 20 \text{ k}\Omega$ . The low-temperature electrical transport properties of the device are characterized in a  $^3\text{He}/^4\text{He}$  dilution refrigerator at a base temperature of  $\sim 20 \text{ mK}$ . We apply a dc and an ac bias,  $V_{\text{SD}} + \delta V$ , to the middle electrode (source) and simultaneously measure the differential conductance  $G = \delta I / \delta V$  in the left and right electrodes (drain) using standard lock-in techniques with an ac voltage of  $\delta V = 20 \mu\text{V}$  at a frequency of  $69 \text{ Hz}$ .

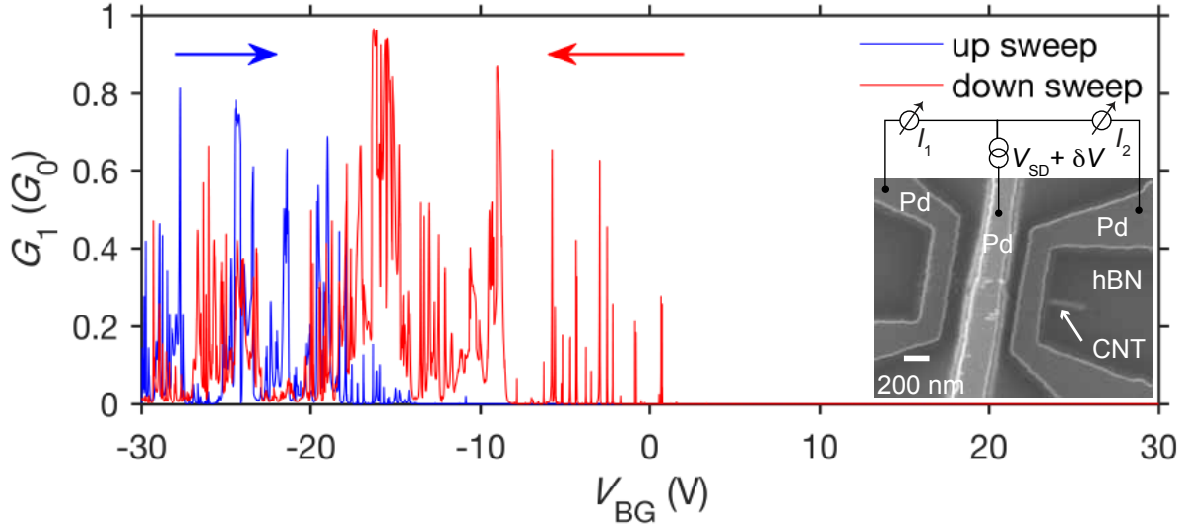


**Figure 5.7.** Zero-bias differential conductance  $G = \delta I / \delta V$  measured as a function of  $V_{BG}$  at  $T = 20$  mK. As  $V_{BG}$  is swept from negative values to positive values, and then back to negative values, a pronounced hysteresis is observed. The arrows indicate the sweeping direction. The corresponding device structure and measurement set-up is shown in the inset.

Interestingly, all of the investigated three-terminal devices with CVD grown monolayer hBN films as tunnel barriers exhibit pronounced hysteresis in their zero-bias  $G$  versus  $V_{BG}$  characteristics. We sweep  $V_{BG}$  continuously from  $-30$  V to  $+30$  V and then back to  $-30$  V. A representative example is shown in Fig. 5.7, where we record the zero-bias  $G_1 = \delta I_1 / \delta V$  as a function of  $V_{BG}$ . We observe that the up and down scans of  $V_{BG}$  lead to a significant hysteresis in terms of the threshold voltage shift. Here, we define the threshold voltage as the onset of  $G$ . In Fig. 5.7, the threshold voltages  $V_T$  for the up and down scans are  $-14$  V and  $+1$  V, respectively, and this corresponds to a relative shift of  $15$  V, which quantifies the amount of hysteresis in the system. We note that a quantitative analysis of the hysteresis requires systematic studies with controlled experimental parameters, for example, the  $V_{BG}$  sweeping range and rate, the time delay before starting each sweep, and the temperature.

A hysteresis in  $G$  versus  $V_{BG}$  characteristics can originate from various physical processes [167–169]. For instance, a variety of nanostructure devices have shown hysteresis in their transport characteristics due to charge injection into trap sites [167, 170–172]. Such a hysteresis is generally attributed to two sources: the interface traps that are located at the interface of the active structure and the dielectric, and the surface traps that are not directly in contact with the active structure but rather along the surface of the dielectric [173, 174]. Specifically, the transport characteristics of CNT field-effect transistors show hysteresis due to charge trapping by water molecules around the CNT, including the  $\text{SiO}_2$  surface-bound water [175]. The hysteretic response occurred in our devices could also be related to the charge trapping by water molecules, since our monolayer hBN film transfer process involves the use of distilled water. By transferring a monolayer hBN film directly onto a  $\text{SiO}_2$  substrate with CNTs below, we may trap few layers of water molecules between the hBN film and the  $\text{SiO}_2$  substrate. In addition,

defect states within the transferred hBN film [176–178] together with PMMA residues left on its surface [153] may offer additional trap sites around the CNT. We are aware that the SiO<sub>2</sub>/Si interface provides dangling Si bonds that can act as trap centers [179].

We now qualitatively explain the hysteretic response observed in our devices using a physical picture based on capacitive charging of surrounding dielectric by charge carriers injected out of the CNT [180]. It is suggested that due to the small radius of curvature of the CNT, the surface of the CNT experiences a much higher electric field than the SiO<sub>2</sub>/Si interface. The secondary dielectrics around the CNT, i.e. the trapped water molecules and the hBN film, reduce the threshold energy required for the charge emission from the CNT [169]. As a result, when a reasonable  $V_{BG}$  is applied, it is possible to extract charge carriers from the CNT [172, 181]. In Fig. 5.7, when the BG sweep starts at a large negative  $V_{BG}$ , holes can be injected out of the CNT and slowly trapped into the secondary dielectrics around the CNT on a time scale comparable to the scale relevant for the measurement. These trapped holes accumulate around the CNT and induce a dynamic screening of  $V_{BG}$ , thereby shifting  $V_T$  towards the negative direction of  $V_{BG}$ . Similarly, a BG sweep starts at a large positive  $V_{BG}$  may lead to the injection of electrons into the secondary dielectrics from the CNT and eventually a shift of  $V_T$  towards the positive direction of  $V_{BG}$ . Thereby, we observe a hysteresis behavior in the zero-bias  $G$  versus  $V_{BG}$  characteristic of our device, as shown in Fig. 5.7.

In addition to the hysteresis behavior, we notice that the BG sweep in Fig. 5.7 shows a complete suppression of  $G$  over a large  $V_{BG}$  range. Surprisingly, all of the characterized three-terminal devices show such a feature in their transport characteristics. We find that an onset of  $G$  occurs at a much higher positive  $V_{BG} \sim +60$  V. However, since this voltage is close to the electrical breakdown voltage of the SiO<sub>2</sub> dielectric layer of our devices, measurement data recorded at this gate voltage are considered unreliable, and we limit our study within the range of  $-30$  V  $< V_{BG} < +30$  V. In Fig. 5.7, the complete suppression of  $G$  over a large  $V_{BG}$  range seems to suggest a semiconducting CNT with a large band gap, and only the electronic transport through the valence band of the CNT is accessible. However, we note that formation of multiple QDs in series configuration can also lead to a strong suppression of  $G$  over a large  $V_{BG}$  range, because the electronic transport is suppressed if any of the QDs is in blockade. An accurate determination of the electronic transport properties of our CNT devices with monolayer hBN tunnel barriers is hindered by the presence of the hysteresis behavior. We note that we often observe certain instability in our devices, and we attribute this to small hysteresis that may present in  $V_{BG}$ . However, the reason for an enhancement of this hysteresis behavior specifically in this batch of devices is unclear. To answer this question, we proceed to device fabrication inside a glove box with controlled dry environment to minimize the possibility for trapping water molecules. As new approach comes with new challenges, we succeed in obtaining working devices with extremely low yield, and further investment in this direction is necessary.

### **Strong tunnel coupling strength**

We now turn to the shape of the zero-bias conductance peak. Analysis of the peak shape allows us to distinguish two transport regimes: the strong coupling (lifetime broadened) regime and the weak coupling (thermally broadened) regime. It also allows



us to determine the tunnel coupling parameters. In Fig. 5.8, we show the zero-bias  $G_1$  and  $G_2$  measured as a function of  $V_{\text{BG}}$  on a three-terminal device shown in the inset of Fig. 5.7. We find that the Breit-Wigner formula given by Eq. 2.10 [67] fits the observed conductance peak shape very well. In Fig. 5.8(a), we obtain a best fit with  $\Gamma_1 \approx 27.56 \mu\text{eV}$  and  $\Gamma_2 \approx 586.90 \mu\text{eV}$ , while a best fit in Fig. 5.8(b) is achieved with  $\Gamma_1 \approx 0.79 \mu\text{eV}$  and  $\Gamma_2 \approx 2091 \mu\text{eV}$ . These numbers suggest that the system is asymmetrically tunnel coupled to the source-drain contacts, and the electrical transport is in a strong coupling regime, i.e.  $\Gamma = \Gamma_1 + \Gamma_2 \gg k_{\text{B}}T$ .

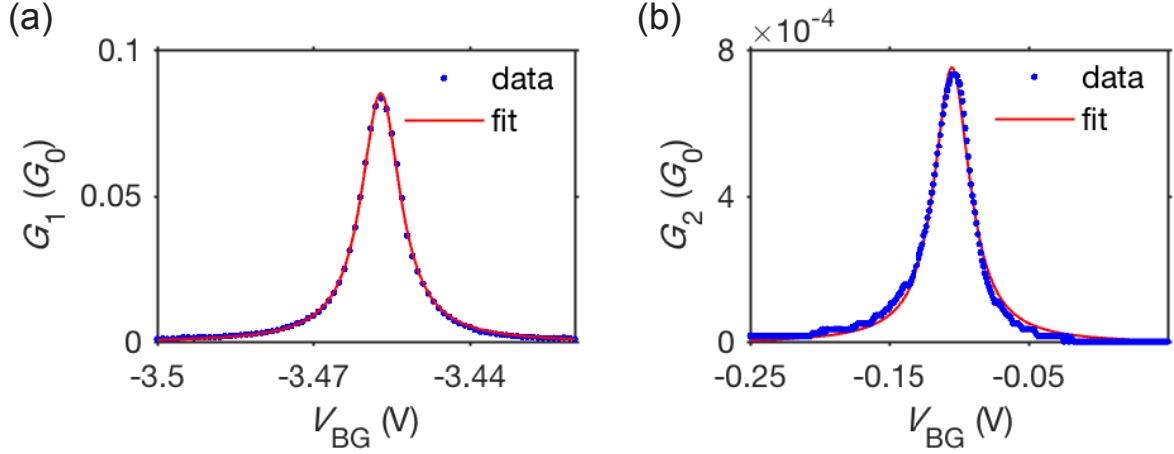


**Figure 5.8.** Zero-bias differential conductance  $G_1 = \delta I_1 / \delta V$  (a) and  $G_2 = \delta I_2 / \delta V$  (b) simultaneously measured as a function of the back-gate voltage  $V_{\text{BG}}$  at  $T = 20$  mK. The red curve represents a best fit obtained for the Breit-Wigner resonance line shape.

By introducing CVD grown monolayer hBN films as tunnel barriers between the metal leads and the CNTs, we hope to tune our devices into a weak coupling regime. In addition, we expect a system with symmetric tunnel coupling to the source-drain contacts. However, our experimental findings are in disagreement with our expectations. This disagreement may arise due to the transfer process induced damages on hBN films. Specifically, during the electrochemical bubbling transfer process the trapped hydrogen bubbles could induce large strains, thereby leading to structural damages [182]. Optical images of hBN films transferred onto the  $\text{SiO}_2$  substrates often show large wrinkles, cracks, holes, and residual particles. In the case that the hBN films are absent due to holes or cracks, we expect strong tunnel couplings to the metal leads. Our ability to transfer large scale and high quality monolayer hBN films determines the performance, yield, and the electrical stability of our devices. We are still facing challenges with our transfer techniques and the overall quality of hBN films is degrading during the transfer process. We are aware that our understanding of the coupling mechanism in CNT-metal contacts is still rather obscure due to the fact that we lack information on the nature of the tunnel barriers. The strong tunnel coupling strengths in our devices may also arise as a result of unexpected new phenomena or new type of coupling mechanisms.

#### 5.2.4. Conclusions

We report our study on CVD grown monolayer hBN films and their integration as tunnel barriers into our CNT devices. We demonstrate that the quality of the hBN films is not consistent and degrades during the transfer process regardless the choice of transfer techniques. The CNT-based three-terminal devices with hBN tunnel barriers show hysteresis in their zero-bias  $G$  versus  $V_{BG}$  characteristics at cryogenic temperatures. In addition, the tunnel coupling strengths extracted by analyzing the zero-bias conductance peak shapes suggest strong tunnel coupling to the source-drain contacts. This work serves as a preliminary research step towards the application of CVD grown monolayer hBN tunnel barriers in CNT-based devices.

# 6 Hexagonal boron nitride encapsulated carbon nanotubes with zero-dimensional contacts

---

## 6.1. Introduction

CNTs that are free from disorders have attracted extensive interest [7, 8, 11]. For example, they offer promising platforms to manipulate spin qubits [152]. In particular, ultra-clean CNTs have been investigated to study spin-orbit interaction and electron-phonon coupling [9, 137]. Although ultra-clean CNTs have high intrinsic electrical conductivity, their integration into electronic circuits is hampered by the large electrical contact resistance in practice. A good electrical coupling between the CNTs and the metal leads is hard to achieve due to hidden factors that are extremely difficult to control. So far, realization of ultra-clean CNT devices with low contact resistances has remained a challenge. Experimental studies on semiconducting and metallic CNTs suggest that the surface chemistry and the contact length have significant influence on the contact resistance [183, 184].

Recently, hBN encapsulated graphene has demonstrated high performance and long-term stability [131, 185]. For instance, ballistic transport phenomenon has been observed owing to the high quality achieved by encapsulation of graphene [185]. In comparison to the conventional devices with electrical contacts on top or at bottom [186], surprisingly low contact resistance has been attained by depositing 1D edge contacts to the encapsulated graphene, and they offer excellent contact properties [105]. Theoretical calculations on these 1D edge contacts reveal that the formation of short bonding distances, the strong overlaps of the electron orbitals, and the low and narrow interface barriers are of crucial importance for obtaining low contact resistances [187]. Up to date, hBN flakes have been used to encapsulate 2D materials beyond graphene, e.g., transition metal dichalcogenides [188]. We have demonstrated that hBN can be used as clean substrates for CNT QDs [34]. However, encapsulation of CNTs within hBN sheets is hard to achieve and has only been reported very recently [47]. The van der Waals forces between 1D CNTs and 2D hBN flakes are not sufficiently strong enough to pick up the CNTs. This means that compared to the 2D layered heterostructures, it is much more difficult to prepare hBN/CNT/hBN stacks.

In this chapter, we report that hBN encapsulated CNTs that are coupled to metal leads via 0D contacts with low contact resistances can be obtained in a reliable manner with a high-yield. The low-temperature characteristics of our devices suggest formation of either a large single QD or a parallel DQD in the CNTs. The fact that we observe well-

defined CB features for a large single QD indicates that high quality hBN encapsulated CNT devices can be realized. We hope that hBN encapsulated CNT devices with high qualities, specifically in terms of the device cleanliness and low contact resistance, offer a potential platform for exploring the ideal 1D electronic properties of CNTs.

## 6.2. Device structure and measurement set-up

The structure and measurement set-up of our hBN encapsulated CNT devices is shown schematically in Fig. 6.1. We use a highly p-doped Si wafer with thermally oxidized 300 nm thick insulation layer, which acts as a global BG. We first pattern the substrate with 5 nm/45 nm thick Cr/Au markers and bond pads and then deposit hBN flakes by mechanical exfoliation. On a separate substrate, we spin coat Mo/Fe catalyst particles and grow CNTs at 950°C by CVD with methane as the source gas. We transfer the CNTs onto the hBN flakes with the help of a PPC film, which first picks up the CNTs from the growth substrate and then places them onto the hBN flakes. We remove the PPC film in chloroform and locate the CNTs on hBN flakes by SEM imaging [34]. After a thermal annealing at 300°C for 2 h to remove the PPC residues, we place a freshly cleaved hBN flake with a thickness in the range of 20 – 60 nm on top to encapsulate the CNTs. The hBN/CNT/hBN heterostructure is assembled by aligning and bringing the hBN flake into contact with a selected CNT/hBN stack. Electrical contacts to the encapsulated CNTs are realized by exposing the hBN/CNT/hBN heterostructure to the  $\text{CHF}_3/\text{O}_2$  plasma in a reactive ion etcher with lead structures defined by electron-beam lithography and PMMA serving as an etching mask. At the end, 10 nm/60 nm thick Cr/Au is deposited to the etched ends of the CNT right after the etching to avoid contamination of the CNT-metal interfaces.

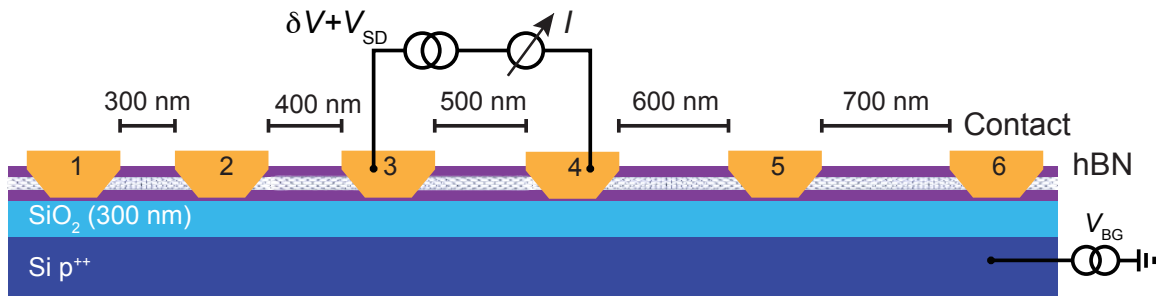


**Figure 6.1.** Schematic device cross section illustrating the device geometry and electronic measurement set-up.

## 6.3. Experimental results

### 6.3.1. Edge profile and contact material selectivity

Figure 6.2 shows the SEM image of an hBN encapsulated CNT device. In this figure, the CNT is not visible, but the metal leads are in direct contact to the etched ends of the CNT. Since we etch through the hBN/CNT/hBN heterostructure, the electrical

contact forms along the circumference of the CNT and is on the order of few nm long. In a zoom-in view of the region highlighted by a red dashed rectangle, we observe an edge profile with a width of  $\sim 80$  nm, as indicated by the blue arrow. This number is equivalent to the total thickness of the hBN/CNT/hBN heterostructure and suggests an edge profile with an angle of  $\sim 45^\circ$ . This edge profile is induced during the reactive ion etching and is most likely due to the anisotropic etching of hBN flakes. This means that the CNT segment between two neighboring metal leads has a length that is larger than the metal contact separation by design.

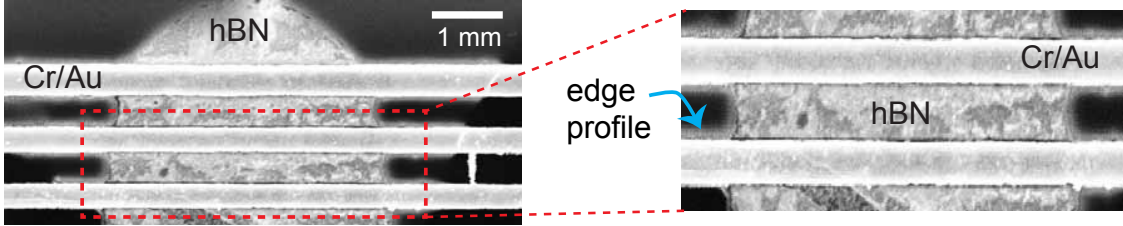


**Figure 6.2.** SEM image of an hBN encapsulated CNT device with electrical contacts.

At room temperature, the two-terminal resistance of our hBN encapsulated CNT devices is in the range of  $40 \text{ k}\Omega - 6 \text{ M}\Omega$  at  $V_{\text{BG}} = 0 \text{ V}$ . These values are lower than the ones of our conventional devices with Pd contacts on top. We have investigated five more different contact materials, i.e. MoSi, Pd, Ti/Al, Cr/Al, and Pd/Pb/In. For each contact material, we prepare an hBN/CNT/hBN heterostructure and deposit 8 electrical contacts next to each other with a spacing of 500 nm by design. We note that Pd, Cr/Al, Cr/Au, and Pd/Pb/In are deposited via electron-beam evaporation, while Ti/Al and MoSi are deposited by thermal evaporation and Ar plasma sputtering, respectively. We find that devices with Cr/Au and MoSi contacts show measurable conductances at room temperature, which indicates the formation of electrical contacts to the encapsulated CNTs. The yield for obtaining a device with a measurable conductance using Cr/Au contacts is high and close to 95%. We also find that the devices with Cr/Au contacts show two-terminal resistances of about an order of magnitude smaller than that of the devices with MoSi contacts. However, Pd, Ti/Al, and Pd/Pb/In contacts lead to devices with no measurable conductance, as summarized in Table 6.1. Among these contact materials, our choice is limited to the Cr/Au as normal metal contacts and MoSi as superconducting contacts.

**Table 6.1.** Contact material selectivity

contact material	property	measurable conductance
Cr/Au	normal metal	✓
MoSi	superconductor	✓
Pd	normal metal	×
Ti/Al	superconductor	×
Cr/Al	superconductor	×
Pd/Pb/In	superconductor	×

### 6.3.2. A large single QD

The electrical transport properties of our hBN encapsulated CNT devices with Cr/Au normal metal contacts are characterized in a  $^3\text{He}$  refrigerator at a base temperature of  $\sim 240$  mK. In the device discussed here, the source-drain contact distance is  $\sim 500$  nm by design, but the CNT segment between the contacts has an estimated length of  $\sim 580$  nm considering the edge profile of  $\sim 40$  nm at both ends of the CNT. We apply a dc and an ac bias,  $V_{\text{SD}} + \delta V$ , and measure the differential conductance  $G$  of the device with an ac voltage of  $\delta V = 40 \mu\text{V}$  at a frequency of 379 Hz. Figure 6.3 shows  $G$  recorded as a function of  $V_{\text{BG}}$  and  $V_{\text{SD}}$ , and we observe regular CB diamonds with a charging energy of  $E_C \approx 7.2$  meV and a clear level spacing of  $\delta E \approx 2.8$  meV, as indicated by the black arrows. For an ideal and undoped metallic CNT segment with a confinement length  $L = 580$  nm, we expect a mean level spacing of  $\delta E = hv_F/2L \approx 2.76$  meV, with  $h$  the Plank constant and  $v_F = 8.1 \times 10^5$  m/s the Fermi velocity [160]. This expected value is in good agreement with the excited state energy extracted from the bias spectroscopy and suggests that the QD confinement of our device is determined by the source-drain metal contacts and not by defects in the CNT.

We now focus on the coupling parameters that can be extracted from the size and shape of the CB diamonds. From the positive and negative slopes of the diamonds, we find similar values for  $C_S$  and  $C_D$ , yielding 10.4 aF and 11.5 aF, respectively. These numbers suggest a symmetric capacitive coupling. The gate capacitance is  $C_{\text{BG}} \approx 0.4$  aF with a lever arm  $\alpha_{\text{BG}}$  that is an order of magnitude smaller than that of devices on  $\text{SiO}_2$ . We are aware that hBN has an anisotropic dielectric constant with a parallel component of  $\epsilon_{\text{par}} \approx 7$ , which can lead to an increased screening parallel to the surface compared to the  $\text{SiO}_2$  substrate [189, 190]. However, this enhanced screening effect can only partially explain the decrease of lever arm. We note that we find an asymmetric tunnel coupling with an upper limit of  $\Gamma \leq 900 \mu\text{eV}$ . This indicates that our hBN/CNT/hBN device is in a strong coupling regime.

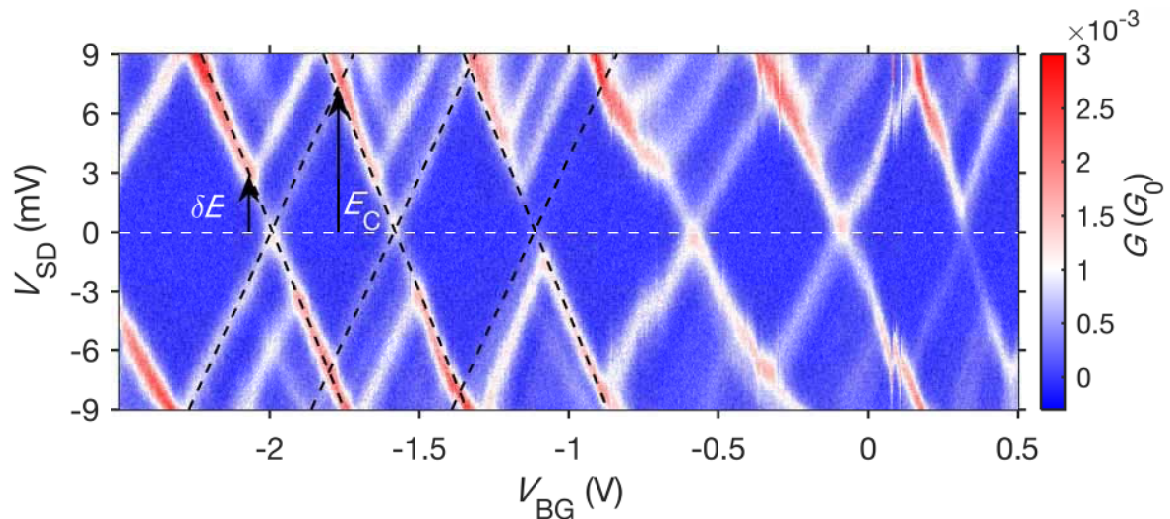


**Figure 6.3.**  $G$  versus  $V_{\text{BG}}$  and  $V_{\text{SD}}$  of an hBN encapsulated CNT device recorded at  $T = 240$  mK. The black dashed lines trace the edges of the CB diamonds

### 6.3.3. A large parallel DQD

In the device discussed here, the CNT segment between the Cr/Au contacts is  $\sim 680$  nm long. In Fig. 6.4(a),  $G$  is plotted as a function of  $V_{\text{BG}}$  and  $V_{\text{SD}}$ , and we observe QD characteristics, e.g., CB diamonds, excited state resonances, and cotunneling lines. In a zoom-in view of the region indicated by the black dashed rectangle, with the corresponding data replotted in Fig. 6.4(b), we find two sets of CB diamonds that do not block transport individually, suggesting a DQD formed in the CNT in a parallel configuration. In Fig. 6.4(b), the dashed black and red lines trace the CB diamonds of QD1 and QD2, respectively, and this DQD feature describes roughly the extended data set of Fig. 6.4(a). We estimate the charging energies of the two individual QDs as  $E_{\text{C1}} \approx 6.0$  meV and  $E_{\text{C2}} \approx 3.7$  meV, which correspond to the total capacitances  $C_{\text{tot1}} \approx 26.8$  aF and  $C_{\text{tot2}} \approx 43.8$  aF, respectively. From the cotunneling line thresholds

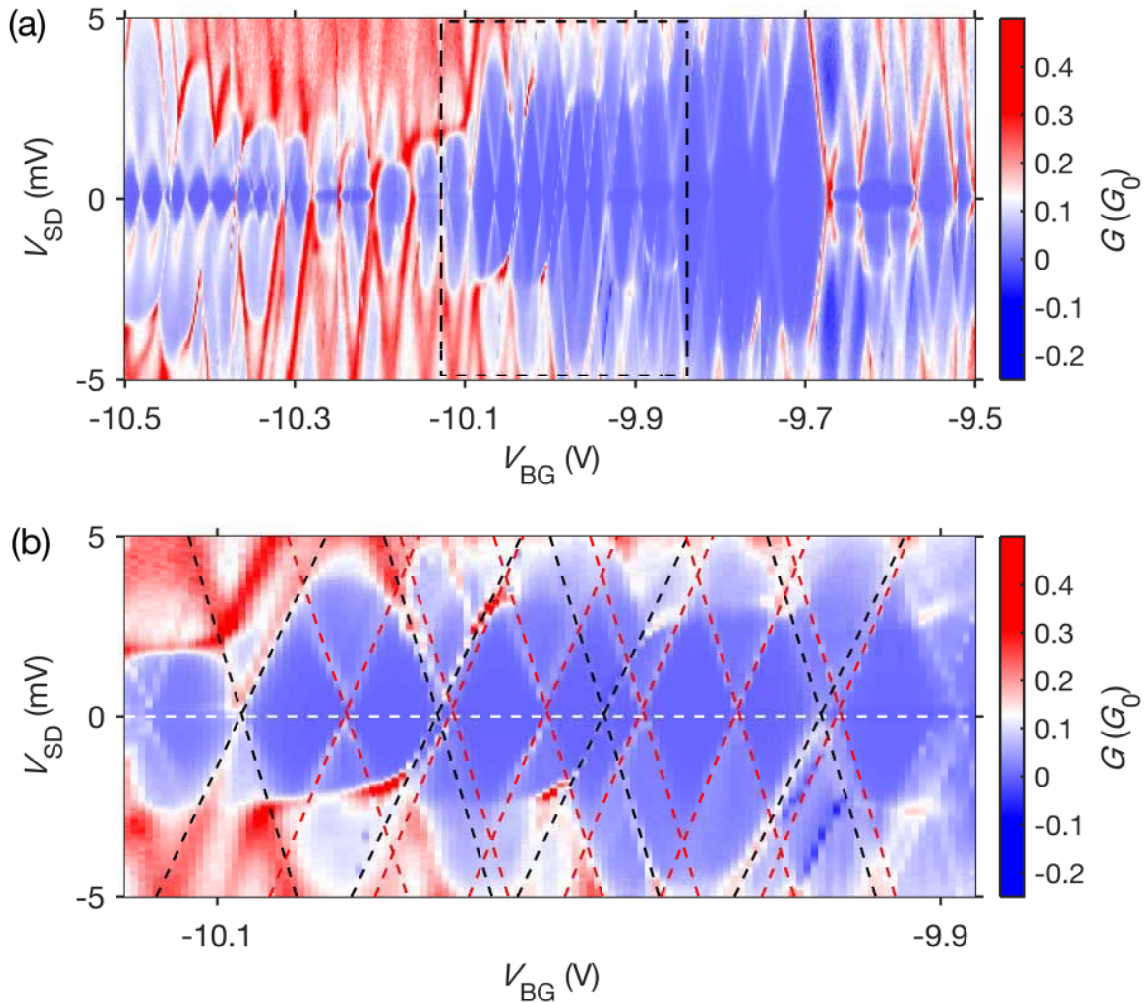


**Figure 6.4.** (a)  $G$  measured as a function of  $V_{\text{BG}}$  and  $V_{\text{SD}}$  of an hBN encapsulated CNT device. (b) High-resolution plot of the region pointed out by the black dashed rectangle. The measurement is performed at 240 mK with an ac voltage of  $\delta V = 20 \mu\text{V}$  at a frequency of 177 Hz.

**Table 6.2.** Extracted parameters for QD1 and QD2

parameters	QD1 (black lines)	QD2 (red lines)
$C_{\text{tot}}$	26.8 aF	43.8 aF
$C_{\text{BG}}$	3.5 aF	6.2 aF
$C_{\text{S}}$	10.4 aF	18.5 aF
$C_{\text{D}}$	12.9 aF	19.1 aF
$\Gamma$	130 $\mu\text{eV}$	100 $\mu\text{eV}$

of QD1, we extract a mean level spacing of  $\delta E_1 \approx 2.3 \text{ meV}$ . This number suggests a quantum confinement size of  $\sim 695 \text{ nm}$ , in good agreement with the length of the CNT segment between the metal contacts, as expected for a QD confined by the metal leads. We further extract the capacitive and tunnel coupling parameters for individual QDs and list them in Table 6.2. We notice that the capacitive coupling to the metal leads is roughly symmetric for both QDs, but  $C_{\text{S}}$  and  $C_{\text{D}}$  of QD1 are about 2 times smaller than that of QD2, as summarized in Table 6.2.

For a DQD formed on two separate CNTs in a bundle, we expect identical  $C_{\text{BG}}$  for individual QDs. However, the extracted  $C_{\text{BG}}$  for QD2 is about 2 times larger, and it is in disagreement with the expected value. If we assume the two individual QDs are formed in different shells of a MWCNT, then reduction of the capacitive coupling parameters of QD1 may arise due to screening effect [191], which is directly related to the intershell interaction. However, the intershell coupling strength is unknown for this device due to the fact that we lack clear evidences for intershell coupling in its finite bias spectroscopy. As we have discussed in the previous chapter, non-zero intershell coupling gives rise to interesting features in the transport spectroscopy, including avoided crossings [35] and a shift of the CB diamond edges. Besides, studies on double-wall CNTs reveal an eight-fold periodic CB diamond pattern [154] as a result of a strong intershell coupling induced by the mixing of orbital states of the two walls. None of these features are observed in the studied finite bias spectroscopy of the device, although two sets of CB diamonds are clearly identified, as shown in Fig. 6.4(b).

## 6.4. Conclusions

We report the fabrication and characterization of hBN encapsulated CNT QDs that are coupled to the metal leads via 0D contacts. We have succeed in fabricating 0D contacts to both ends of the CNT segment with a yield close to 95%. However, we find that the choice for contact materials is limited. The low-temperature characteristics of an hBN/CNT/hBN heterostructure show clear CB features and suggests the formation of a large single QD with a confinement size of  $\sim 580 \text{ nm}$ , which is determined by the metal contacts and not by defects in the CNT. In comparison, a second device shows the formation of a parallel DQD in the CNT. The extracted capacitive coupling parameters of individual QDs suggest that these two QDs are most likely formed in different shells of a MWCNT. We believe that by depositing 0D contacts to the etched ends of a MWCNT, there is a high probability to electrically contact multishell of the nanotube.



# 7 Induced superconductivity in end-contacted carbon nanotubes

## 7.1. Introduction

A Josephson junction, which consists of two superconductors separated by a weak link, provides an ideal platform to study a variety of macroscopic quantum phenomena in a solid state system [91, 192–196]. In particular, superconducting qubits based on Josephson junctions have been intensively studied owing to their potential applications for superconducting quantum computers [197]. In this context, the CNT-superconductor heterostructures are particularly interesting [3, 81, 92, 97, 198–202], because the CNT as an ideal 1D system offers a limited number of modes with  $\delta E$  on the scale of meV, which is comparable to the conventional superconducting energy gap,  $\Delta$ .

In this chapter, we study hBN encapsulated CNTs with 0D side contacts made of superconductor, MoSi. Depending on the tunnel coupling strength between the CNTs and the superconducting leads, our CNT-superconductor heterostructures reveal three different transport regimes. For example, in a weak coupling regime, i.e.,  $\Gamma \ll \Delta$ , the transport is dominated by CB with a large  $E_C$  and quasiparticle (QP) tunneling. In an intermediate coupling regime, i.e.,  $\Gamma \sim \Delta < \delta E, E_C$ , we identify features, such as QDs with large superconducting energy gaps, QP tunneling, resonant Andreev tunneling (AT), as well as Andreev bound states in the transport spectroscopy. In contrast, if the coupling is strong, i.e.,  $\Gamma \gg \Delta, \delta E, E_C$ , we find multiple Andreev reflections (MARs) and strong negative differential conductance (NDC). In addition, the magnetic field dependence of the critical current,  $I_C$ , shows a non-monotonic behavior. This behavior is in strike contrast to that of conventional superconductors, e.g., Al [203–205].

## 7.2. Device structure and measurement set-up

The structure and measurement set-up of our hBN encapsulated CNT devices with 0D superconducting side contacts is shown schematically in Fig. 7.1(a). The device fabrication is described in section 6.2. Here, we note that 70 nm thick superconducting contacts made of MoSi are Ar sputtered to the open ends of the etched CNT segment. We find that when MoSi is deposited on thick hBN flakes, it often breaks at the flake edges and leads to disconnected lead wires. To avoid this,  $\text{SF}_6/\text{Ar}/\text{O}_2$  plasma is employed instead of  $\text{CHF}_3/\text{O}_2$ , because it provides a higher etching rate of hBN, such that thick hBN flakes can be completely etched away in a short time. We note that by depositing 300 nm wide MoSi side contacts immediately after etching, two neighboring segments of the encapsulated CNT are connected to a single superconducting lead by side contacts,

as depicted in Fig. 7.1(a). For 70 nm thick MoSi leads, we expect a critical temperature of  $T_C \sim 7$  K and a correspondingly large critical magnetic field of  $B_C \sim 8$  T at 4 K [206].

### 7.2.1. Characteristics in an intermediate coupling regime

In the device discussed here, the source-drain contacts are placed 600 nm apart by design, but if we take into account the edge profile of  $\sim 30$  nm at each end of the tube, the encapsulated CNT segment has an estimated geometry length of  $\sim 660$  nm. At room temperature, the device has a two-terminal resistance of  $40$  k $\Omega$  at  $V_{BG} = 0$  V. The low-temperature electrical transport properties of the device are characterized in a dilution refrigerator at a base temperature of  $\sim 10$  mK. We apply a dc and an ac bias,  $V_{SD} + \delta V$ , and measure the differential conductance,  $G = \delta I / \delta V$ , by standard lock-in techniques with  $\delta V = 20$   $\mu$ V at a frequency of 177 Hz.

Figure 7.1(b) shows  $G$  of the device plotted as a function of  $V_{BG}$  and  $V_{SD}$  at  $B = 0$  T. We observe clear CB diamonds and a series of excited state resonances, which indicate the formation of a QD in the CNT segment. Tuning  $V_{BG}$  leads to a diamond feature with alternating size between small and large, which suggests a two-fold periodicity, as expected for a clean CNT QD with most likely valley degeneracy lifted. We estimate the charging energy of the dot as  $E_C \approx 4.6$  meV, with a lever arm of  $\alpha_{BG} \approx 0.11$ . The spacing between the ground and the first excited state gives an energy level spacing of  $\delta E \approx 1.8$  meV. For an ideal and undoped metallic CNT, from the confinement-induced finite level spacing, as given by  $\delta E = h v_F / 2L$ , with  $h$  being the Plank constant and  $v_F = 8.1 \times 10^5$  m/s being the Fermi velocity [160], we expect a QD size of  $L \sim 880$  nm, which is larger than the estimated length of the tube segment. This means that the QD confinement of the device is most likely determined by the metal contacts, and the encapsulated CNT segment is defect-free.

### Large superconducting gap

To characterize the QD formed in the CNT segment, we focus on the region highlighted by the black dashed rectangle in Fig. 7.1(b). The corresponding data is replotted in Fig. 7.1(c), and the resonance positions are traced as red and blue lines in Fig. 7.1(d). We first identify the CB diamonds by constructing the expected diamond structure for the case of normal leads, such that the edges of the diamonds cross at  $V_{SD} = 0$ , as represented by the gray lines in Fig. 7.1(d). However, at  $T = 10$  mK and  $B = 0$  T, the source-drain contacts are in superconducting states with a superconducting energy gap of  $\Delta$ . In this case, we expect that the onsets of the diamond edges shift in bias to a higher value of  $|V_{SD}| = 2\Delta$ . This means that the constructed diamond structure (gray lines) evolves into a “superconducting CB diamond” pattern (red lines) that is separated in bias by a transport gap of  $4\Delta \approx 2.8$  meV, as indicated by the black dashed lines in Fig. 7.1(d). Thereby, we attribute these resonances (red lines) to QP tunneling, and the tips of the diamonds mark the onset of this tunneling process. As schematically illustrated in Fig. 7.2(a), the sequential tunneling of quasiparticles through the dot can only take place, if the dot level is simultaneously aligned with the quasiparticle DOS in the superconducting leads.

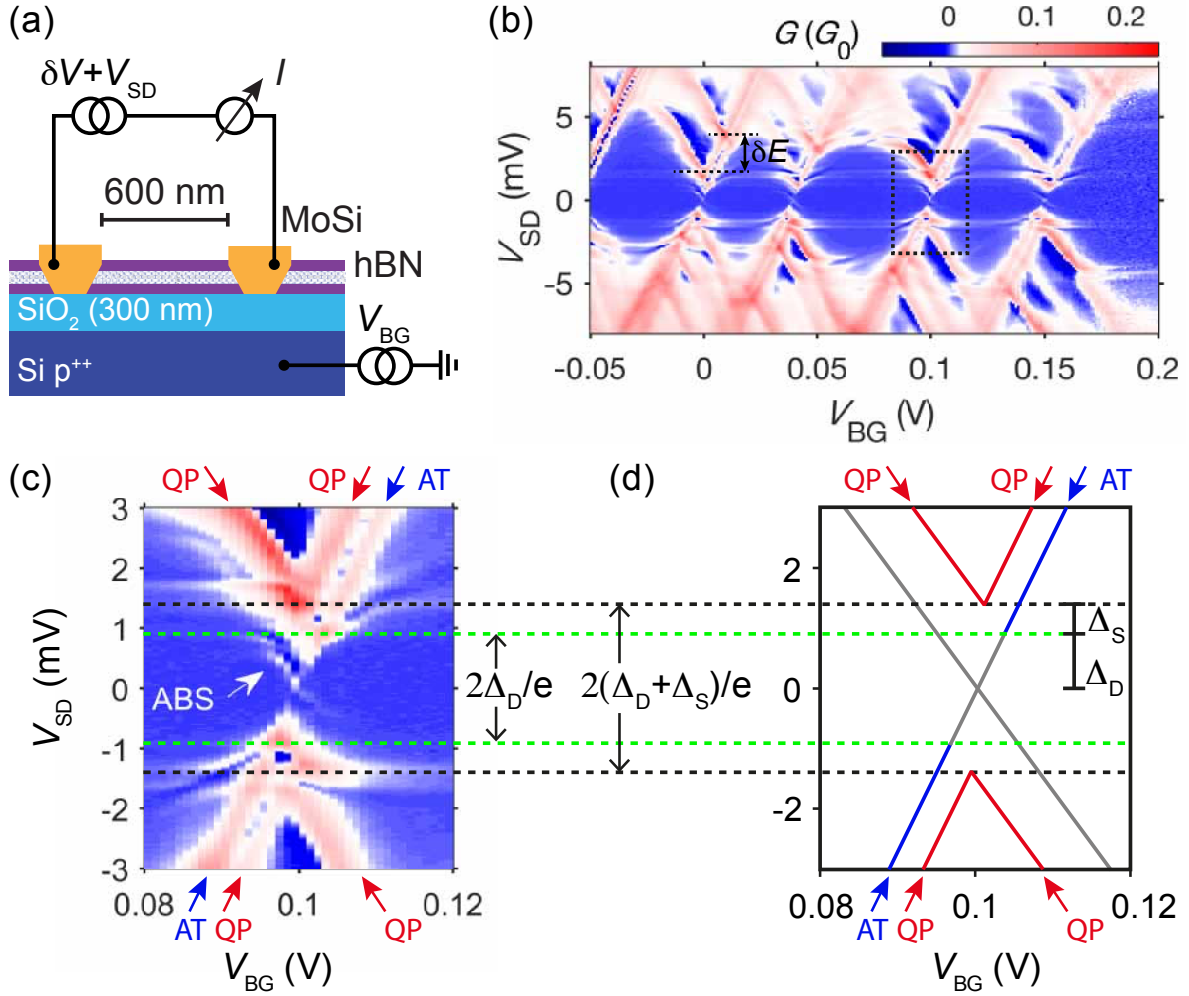


**Figure 7.1.** (a) Schematic cross section view of the device geometry and measurement set-up. (b) Colorscale plot of  $G$  as a function of  $V_{SD}$  and  $V_{BG}$  at  $T = 10$  mK and  $B = 0$  T. (c) Magnification of the region highlighted by the black dashed rectangle in Fig. 7.1(b). Two resonances are labeled as QP and AT. The black and green dashed lines mark the onset of QP and AT resonances, while the white arrow points out an Andreev bound state. (d) Schematic charge stability diagram for the QD identified in Fig. 7.1(c). The red and blue lines trace the positions of QP and AT, respectively. The gray lines represent the expected diamond edges for the case of normal leads.

The shift of the diamond edges with negative slope suggests a superconducting gap of  $|\Delta_D| = 0.9 \pm 0.1$  meV in the drain electrode, as indicated by the green dashed lines in Fig. 7.1(c). However, the shift of the diamond edges with positive slope indicates a superconducting gap of  $|\Delta_S| = 0.5 \pm 0.1$  meV in the source contact. These values lead to an asymmetry of  $|\Delta_D|/|\Delta_S| \sim 1.8$ . The fact that excited state resonances running in parallel to the superconducting CB diamond edges with negative slope are most pronounced, indicates an asymmetric tunnel coupling of the QD to the source and drain contacts. As pointed out in Ref.[207], asymmetric tunnel coupling may give rise to asymmetry in  $\Delta_S$  and  $\Delta_D$ . We note that in Fig. 7.1(c), we also observe Andreev bound states, which are labeled as ABS [199, 208].

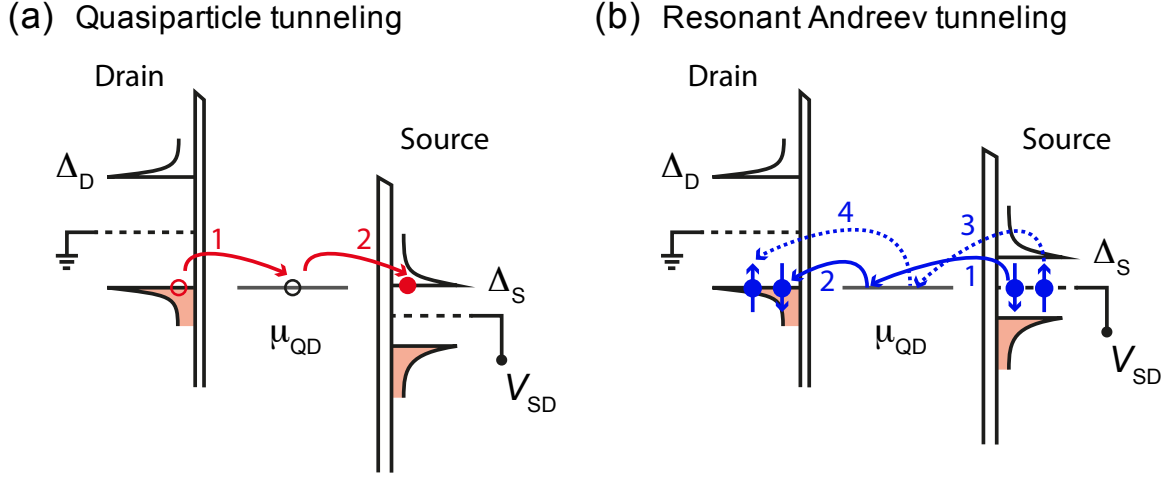


**Figure 7.2.** (a) Energy-DOS diagram for quasiparticle tunneling through a QD level that is simultaneously aligned with occupied quasiparticle states in drain and empty quasiparticle states in source. (b) Energy-DOS diagram explaining the transport mechanism for resonance Andreev tunneling through a QD level, where Cooper pairs are injected from source. In this diagram, the QD level is simultaneously aligned with occupied quasiparticle states in drain and the electrochemical potential of source.

## Resonant Andreev tunneling

We now turn to the resonance lines that are labeled as AT and replotted as blue lines in Fig. 7.1(d). The resonance line AT runs parallel to the diamond edges (red lines) with positive slope and does not cross the entire transport gap, instead, terminates at a finite bias,  $|V_{SD}| = |\Delta_D|$ , as indicated by the green dashed lines in Fig. 7.1(d). We ascribe this resonance line to resonant Andreev tunneling, which is schematically illustrated in Fig. 7.2(b) as a 4<sup>th</sup> order tunneling process. In this figure, the QD level is aligned with the electrochemical potential of the source, such that injection of Cooper pairs from the source is allowed, and the onset of this process is determined by  $|\Delta_D|$ . Similarly, if the QD level is aligned with the electrochemical potential of the drain, removal of Cooper pairs from the drain can give rise to a resonance line that runs parallel to the diamond edges with negative slope. In this case,  $|\Delta_S|$  determines the onset of this process. However, in Fig. 7.1(b), there is no clear signature of resonant AT lines with negative slope. We note that features described here are clearly visible up to  $T = 1$  K.

## Resonant tunneling model

To gain a deeper understanding, we use resonant tunneling model of a QD coupled to superconducting leads. For simplicity, we restrict our model to the case, where transport takes place through a single resonant level of the dot, which has a large charging energy of  $E_C$ . Similar to the experiment, in our model, a dc bias voltage,  $V_{SD}$ , is applied to the source electrode, while the drain electrode is kept grounded. The total current across the junction is computed as the sum of contributions from quasiparticle tunneling ( $I_{QP}$ ), Cooper pair tunneling ( $I_{CP}$ ), and resonant Andreev tunneling ( $I_{AT}$ ), i.e.,  $I = I_{QP} + I_{CP} + I_{AT}$ .

The current contribution from quasiparticle tunneling is approximated as

$$I_{\text{QP}} = \frac{-e}{h} \int_{-\infty}^{\infty} dE [D_{\text{S}}^{(\text{QP})}(E + eV_{\text{SD}}) D_{\text{D}}^{(\text{QP})}(E)] \times T_{\text{QD}}(E) \times [f_{\text{S}}(E + eV_{\text{SD}}) - f_{\text{D}}(E)]. \quad (7.1)$$

In this expression,  $f_{\text{S,D}}(E) = 1/[1 + \exp(E/k_{\text{B}}T)]$  are the Fermi distribution functions in the respective leads. The transmission probability,  $T_{\text{QD}}(E)$ , is described by a Breit-Wigner transmission function [67] as  $T_{\text{QD}}(E) = \Gamma_{\text{S}}\Gamma_{\text{D}}/[(E - E_0)^2 + (\Gamma_{\text{S}} + \Gamma_{\text{D}})^2/4]$ , with  $E_0$  being the position of the resonance. The BCS-type DOS in respective leads is expressed as

$$D_{\text{S,D}}^{(\text{QP})}(E) = \text{Re}\left[\frac{|E - \mu_{\text{S,D}} + i\gamma_{\text{S,D}}|}{\sqrt{(E - \mu_{\text{S,D}} + i\gamma_{\text{S,D}})^2 - \Delta_{\text{S,D}}^2}}\right], \quad (7.2)$$

with  $\gamma_{\text{S,D}}$  being the phenomenological Dynes parameter [209],  $\Delta_{\text{S,D}}$  being the superconducting gaps in the respective leads, and  $\mu_{\text{S,D}}$  being the electrochemical potentials of the source-drain electrodes, with  $\mu_{\text{S}} = -eV_{\text{SD}}$  and  $\mu_{\text{D}} = 0$ . We note that the phenomenological Dynes parameter,  $\gamma_{\text{S,D}}$ , is related to the finite lifetime of quasiparticles in superconducting leads. In Fig. 7.3(a), we plot the BCS-type DOS described by Eq. 7.2 as a black curve.

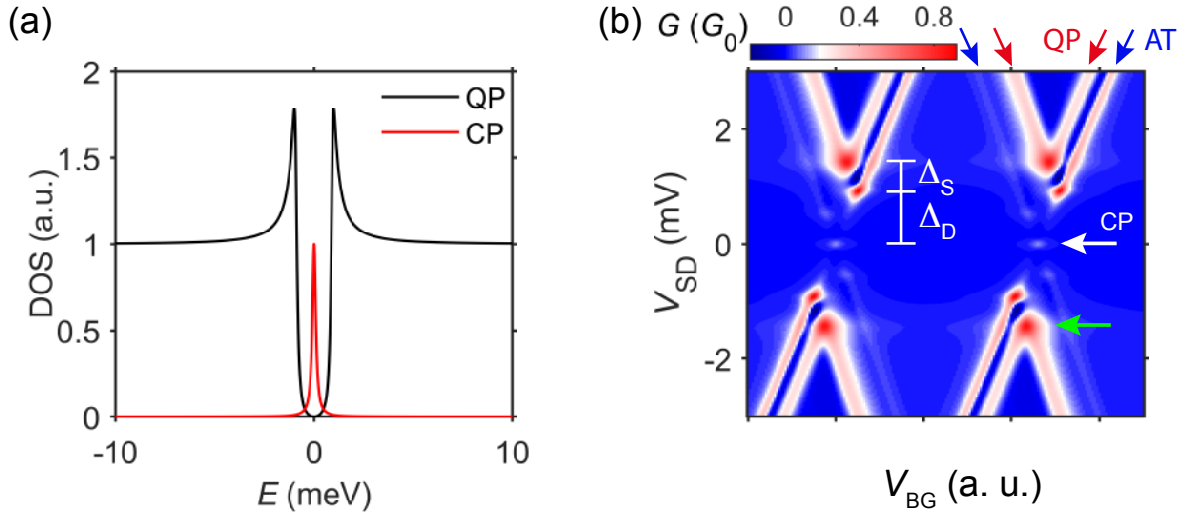


**Figure 7.3.** (a) Energy diagram of quasiparticles (black line) and Cooper pairs (red line). (b) Simulation of  $G$  as a function of  $V_{\text{SD}}$  and  $V_{\text{BG}}$  using our resonant tunneling model. This simulation is obtained for  $\Delta_{\text{S}} = 0.5 \text{ meV}$ ,  $\Delta_{\text{D}} = 0.9 \text{ meV}$ ,  $\gamma_{\text{S,D}} = 100 \mu\text{eV}$ ,  $n_{\text{S}} = 1$ ,  $n_{\text{D}} = 0.1$ ,  $w_{\text{S,D}} = 100 \mu\text{eV}$ ,  $\Gamma_{\text{S,D}} = 0.2 \text{ meV}$ ,  $E_{\text{C}} = 4.6 \text{ meV}$ ,  $\alpha_{\text{S,D}} = 0.45$ ,  $\alpha_{\text{BG}} = 0.1$ , and  $T = 10 \text{ mK}$ . Here,  $\alpha_{\text{S,D,BG}}$  are the lever arms of respective electrodes. Similar to the experiment shown in Fig. 7.1(c), resonant AT lines running parallel to the superconducting CB diamond boundaries with positive slope appear. The white arrow points out the zero-bias conductance induced by Cooper pair tunneling at  $V_{\text{SD}} = 0$ . The increase of conductance at the tip of the CB diamonds, as indicated by the green arrow, is not physical (no tunneling rates considered).

The current contribution from Cooper pair tunneling is calculated by assuming a Cooper pair density function, which has a Lorentzian line shape described as

$$D_{S,D}^{(CP)}(E) = n_{S,D} \frac{w_{S,D}^2}{(E - \mu_{S,D})^2 + w_{S,D}^2}, \quad (7.3)$$

where  $n_{S,D}$  and  $w_{S,D}$  are the density maximum and the widths of the density peak, respectively. This formula describes the red curve in Fig. 7.3(a). The current can now be calculated as

$$I_{CP} = \frac{-2e}{h} \int_{-\infty}^{\infty} dE [D_S^{(CP)}(E + eV_{SD}) D_D^{(CP)}(E)] \times T_{QD}^2(E) \times [f_S(E + eV_{SD}) - f_D(E)]. \quad (7.4)$$

The current contribution from resonant Andreev tunneling is given by

$$I_{AT} = \frac{-2e}{h} \int_{-\infty}^{\infty} dE [D_S^{(QP)}(E + eV_{SD}) D_D^{(CP)}(E) + D_D^{(QP)}(E) D_S^{(CP)}(E + eV_{SD})] \times T_{QD}^2(E) \times [f_S(E + eV_{SD}) - f_D(E)]. \quad (7.5)$$

Since the resonant Andreev tunneling process involves two electrons tunneling through the same dot level, it is treated as a 4<sup>th</sup> order process, and we expect a sharp decay of the probability amplitude away from the resonance.

Figure 7.3(b) shows  $G$  calculated in our model as a function of  $V_{SD}$  and  $V_{BG}$  for  $\Delta_S = 0.5$  meV,  $\Delta_D = 0.9$  meV,  $\Gamma_{S,D} = 0.2$  meV, and  $E_C = 4.6$  meV. We find a reasonable agreement between the experiment and our model. The QP tunneling and resonant AT lines observed in our measurement, are well reproduced by our model, as correspondingly pointed out by the red and blue arrows in Fig. 7.3(b). Our model shows that the resonant AT line runs parallel to the superconducting CB diamond edges and terminates at a finite bias. In our experiment, the resonant AT line with positive slope is well visible, but the one with negative slope is absent. This feature is captured in our

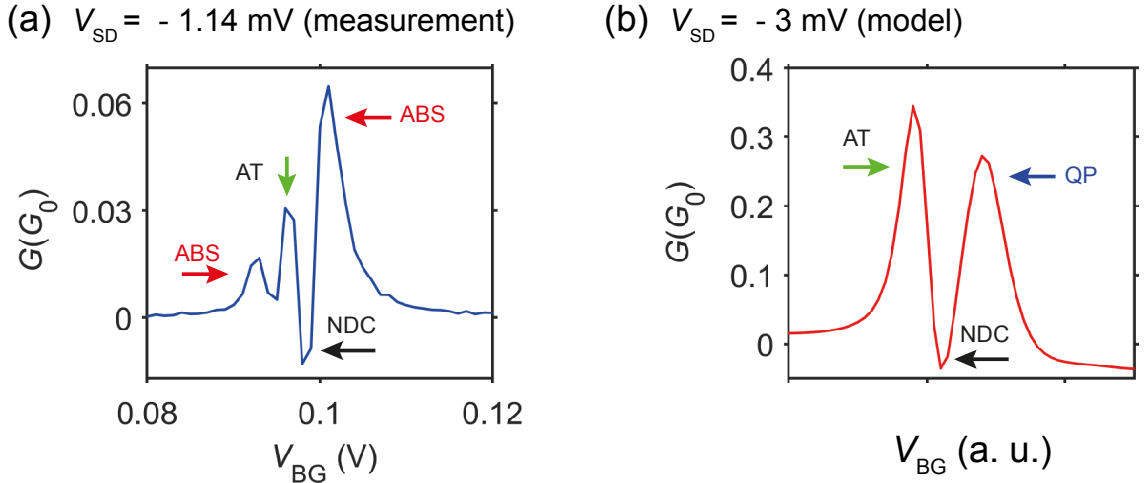


**Figure 7.4.** (a)  $G$  measured as a function as  $V_{BG}$ . (b)  $G$  calculated as a function of  $V_{BG}$ . Similar to the measurement, our model shows strong NDC dip.

model by setting  $n_S = 1$  and  $n_D = 0.1$ , such that the resonant AT lines with negative slope are strongly suppressed. In addition, the onset of AT resonance with positive slope is determined by  $\Delta_D$ , which is also in agreement with our experiment.

In Fig. 7.4(a), we show  $G$  measured as a function of  $V_{BG}$ . To compare the experiment with our model, in Fig. 7.4(b), we plot the calculated  $G$  versus  $V_{BG}$ . The experiment and our model both reveal a clear peak-dip structure with negative differential conductance (NDC). We attribute this combination of  $G$  peak and NDC dip to a BCS-type quasiparticle DOS in the superconducting leads. In particular, when the QD level is aligned with the DOS peak at the edge of the superconducting gap, the tunneling current reaches a maximum and thereby leads to a  $G$  peak. However, as the dot level moves away from the DOS peak, it decreases due to the reduction of available DOS, thereby leading to the NDC dip. This is in strike contrast to the case of a QD coupled to the normal metal leads. In such a scenario, the DOS in normal metal leads is constant. When the dot level enters the bias window, one can only observe a step-like increase of  $G$  with no NDC dip.

### 7.2.2. Characteristics in a strong coupling regime

In the device discussed here, the CNT segment between the source and drain electrodes is  $\sim 580$  nm long. In Fig. 7.5(a), we show  $G$  of the device plotted as a function of  $V_{SD}$  at  $V_{BG} = -29$  V,  $T = 20$  mK, and  $B = 0$  T. In this figure, we find several  $G$  peaks and NDC dips. The  $G$  peak marked by the red arrow is interpreted as a manifestation of the supercurrent, which is induced by the Cooper pair tunneling across the junction at  $V_{SD} = 0$  V. The  $G$  peaks at finite bias voltages are ascribed to MAR, and the peak

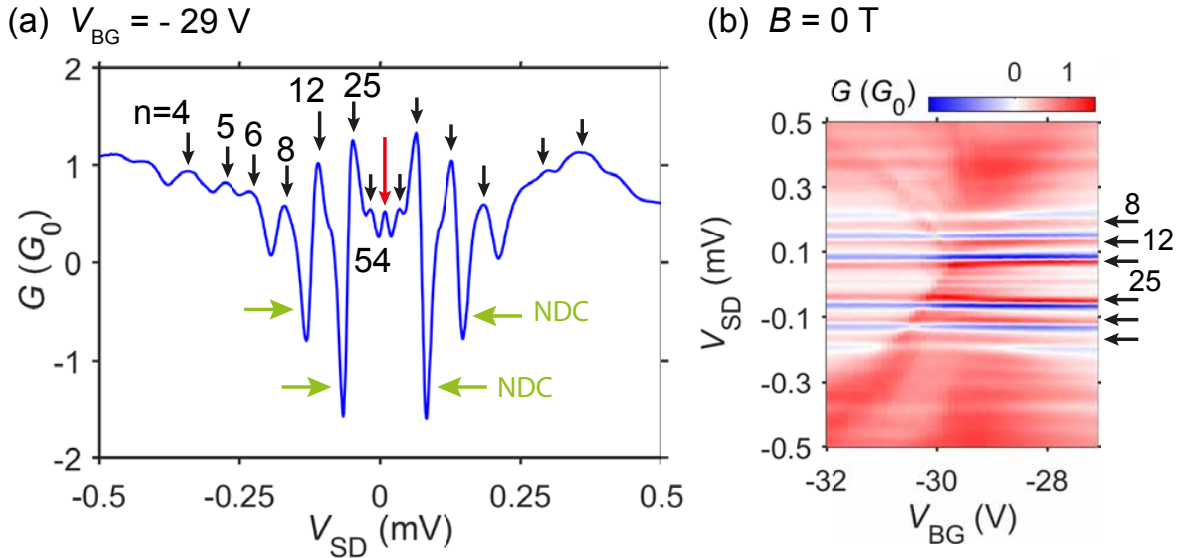


**Figure 7.5.** (a)  $G$  versus  $V_{SD}$ . The calculated MAR peak positions are indicated by the black arrows, and the corresponding values of  $n$  are given. The red and green arrows mark the supercurrent peak and the NDC dips, respectively. (b)  $G$  plotted as a function of  $V_{SD}$  and  $V_{BG}$ . The positions of the MAR peaks with  $n = 8, 12,$  and  $25,$  are pointed out by the black arrows.

positions are given by  $V_{SD} = 2\Delta/en$ , with  $n = 1, 2, 3, \dots$  being the number of Cooper pairs transferred across the junction. We set  $\Delta = 0.7 \text{ meV}$  (see previous section) and calculate the expected positions of MAR peaks. We find that the measured  $G$  peaks correspond to the MAR peaks with  $n = 4, 5, 6, 8, 12, 25$ , and  $54$ , as pointed out by the black arrows in Fig. 7.5(a), thereby suggesting high transparency of the CNT-superconductor interfaces of our device.

The gate dependence of MAR is shown in Fig. 7.5(b), where  $G$  is plotted as a function of  $V_{SD}$  and  $V_{BG}$  at  $B = 0 \text{ T}$  and  $T = 20 \text{ mK}$ . As expected, the positions of MAR peaks remain constant with respect to  $V_{BG}$ . We also notice that the positions of the NDC dips that are associated with MAR peaks with  $n = 8, 12$ , and  $25$ , are also gate independent, as shown in Fig. 7.5(b). The observed  $G$  peaks and NDC dips can now be understood by considering coherent MAR in the presence of broadened bound states [210, 211], as schematically illustrated in Fig. 7.6(a). In this picture, the electron distribution function (red curve) determines the occupation of bound states, which in turn determines the current across the junction. As shown in Fig. 7.6(a), if the energy of MAR coincide with a bound state, one obtains a large current across the junction, thereby leading to a  $G$  peak. On the other hand, with increasing  $V_{SD}$ , the current contribution from MAR decreases, because the number of allowed MAR reduces as increasing  $V_{SD}$ . However, we note that the ohmic current increases with increasing  $V_{SD}$ . As pointed out in Ref.[210], if the decrease of MAR current is stronger than the increase of ohmic current, a NDC dip appears in the  $G$  versus  $V_{SD}$  characteristic, as shown in Fig. 7.5(a).

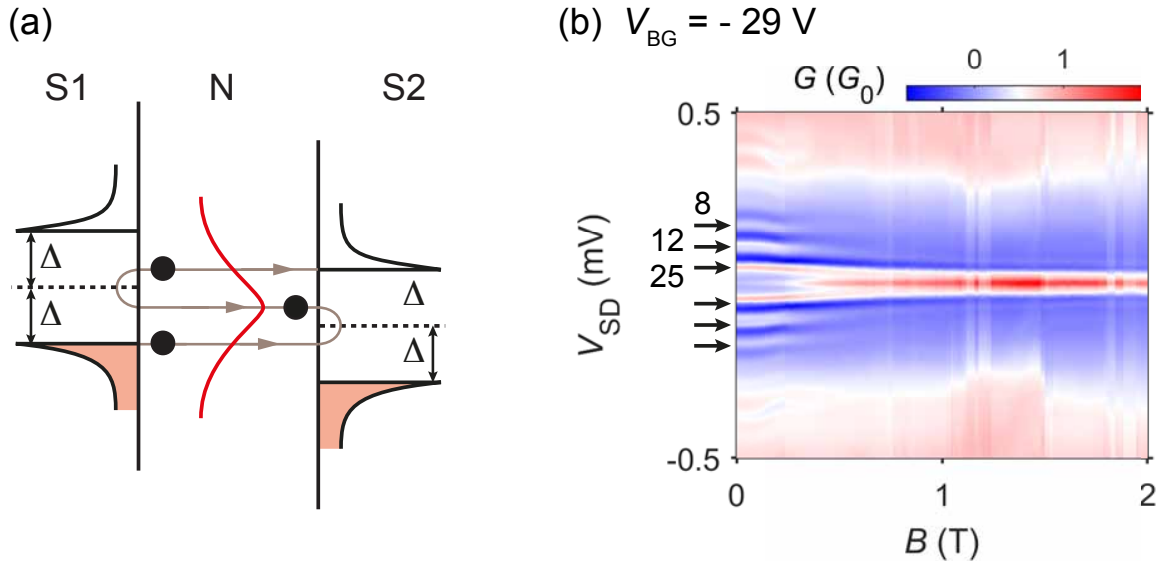


**Figure 7.6.** (a) Energy-DOS diagram, which explains the NDC dips. The width of the resonance (red curve) is on the order of  $\Delta$ . (b)  $G$  recorded as a function of  $V_{SD}$  and  $B$ . The black arrows mark the positions of MAR with  $n = 8, 12$ , and  $25$  at  $B = 0 \text{ T}$ .

The magnetic field dependence of MAR is shown in Fig. 7.6(b), where we measure  $G$  as a function of  $B$  and  $V_{SD}$  at a fixed gate voltage of  $V_{BG} = -29 \text{ V}$ . Here, the magnetic field is applied perpendicular to the substrate and the tube axis. In Fig. 7.6(b), for  $B < 0.7 \text{ T}$ , the positions of MAR resonances with  $n = 8, 12$ , and  $25$ , as pointed out by the black arrows, slowly shift to lower biases with increasing  $B$ . However, the MAR



resonances associated with  $n = 12$  and  $n = 25$  remain constant for  $B > 0.7$  T, while the one with  $n = 8$  disappears at  $B \sim 0.7$  T. In addition, as increasing  $B$ , the width and amplitude of supercurrent increase with a significant enhancement occurring at  $B \sim 300$  mT. We note that for  $B < 300$  mT, the visibility of MAR features is stronger than that of supercurrent, but for  $B > 300$  mT, the supercurrent is most pronounced. Intuitively, we speculate that there is a competition between supercurrent and MAR in magnetic field.

## Magnetic field dependence of supercurrent

So far, we have characterized the device by applying a voltage bias,  $V_{SD}$ , and then measuring the differential conductance,  $G$ . Here, we turn to the measurements, where we apply a current bias,  $I_{SD}$ , and measure the voltage drop,  $V_{JJ}$ , across the junction in a two-terminal configuration. We first discuss  $V_{JJ}$  versus  $I_{SD}$  curves measured at a large magnetic field of  $B = 1.35$  T, as shown in Fig. 7.7(a). In this figure,  $I_{SD}$  is swept back (red curve) and forth (blue curve) at a fixed gate voltage of  $V_{BG} = -15$  V, such that we observe a sharp switching feature with hysteresis. This sharp switching feature suggests a clear transition between the superconducting and normal states at a critical current of  $I_C \approx 5$  nA, as indicated by the black arrow in Fig. 7.7(a). The hysteresis behavior can now be attribute to quasiparticle heating effect [212]. The measured value of  $I_C$  is comparable to the one reported in Ref.[204] on a similar device to ours, but is much smaller than the expected theoretical value of  $I_O = 2e\Delta/\hbar \approx 340$  nA for  $\Delta = 0.7$  meV and symmetric barriers. Such a discrepancy between the measured and expected values of the critical current has been reported previously and explained by considering the electromagnetic environment of a resistively and capacitively shunted Josephson junction [201].

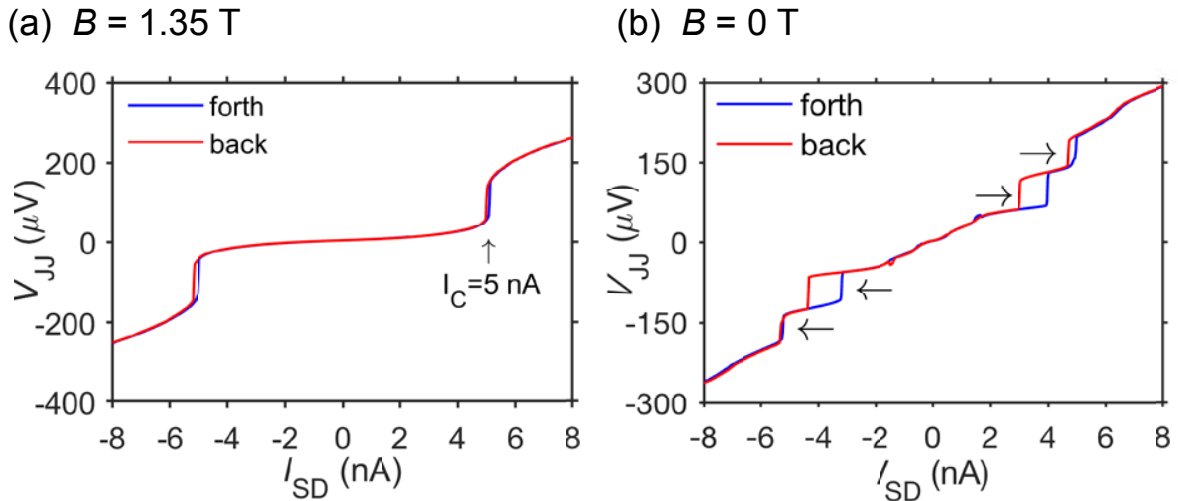


**Figure 7.7.** Back and forth curves of  $V_{JJ}$  versus  $I_{SD}$ , which are measured in a two-terminal configuration for a fixed gate voltage of  $V_{BG} = -15$  V at: (a)  $B = 1.35$  T and (b)  $B = 0$  T. The vertical arrow mark the switching feature at  $I_C = 5$  nA. The horizontal arrows point out the step-like features.

Moreover, from the slope of the curve at  $|I_{SD}| > I_C$ , we extract a normal state resistance of  $R_N \sim 25 \text{ k}\Omega$ . For  $|I_{SD}| < I_C$ , we expect an effective zero resistance, as the system remains in the superconducting state. However, in Fig. 7.7(a), the  $V_{JJ}$  versus  $I_{SD}$  curve shows a finite slope of  $\sim 2 \text{ k}\Omega$  at  $|I_{SD}| < I_C$ . To explain this non-zero resistance, we introduce a diffusive superconducting branch, where the motion of the particle in a tilted washboard potential is diffusive. In particular, for  $|I_{SD}| < I_C$ , the particle has a high chance to be thermally activated to leave one potential minimum and then retrapped in the next potential minimum due to friction. Such a motion is diffusive and can lead to a small average phase velocity, i.e., a voltage across the junction, which in turn means a finite resistance at  $|I_{SD}| < I_C$ .

We now turn to the  $V_{JJ}$  versus  $I_{SD}$  curves at zero magnetic field, i.e.,  $B = 0 \text{ T}$ , as shown in Fig. 7.7(b). In this figure, we observe step-like features that are hysteretic, as marked by the black arrows. In Ref.[210], several current-voltage curves with similar characteristics to ours are computed, and the hysteretic behavior appeared in such a curve is described by NDC instead of self-heating. Thereby, we ascribe the finite hysteretic steps observed in Fig. 7.7(b) to the NDC appeared in our voltage biased measurement, as shown in Fig. 7.5(a). We note that we extract a critical current of  $I_C \approx 0.2 \text{ nA}$  from the curve shown in Fig. 7.7(b). This extracted value of the critical current is more than 10 times smaller than the one obtained at a large magnetic field of  $B = 1.35 \text{ T}$ . This suggests an increase of supercurrent with increasing  $B$ , which is also in agreement with our finding of supercurrent enhancement in Fig. 7.6(b).

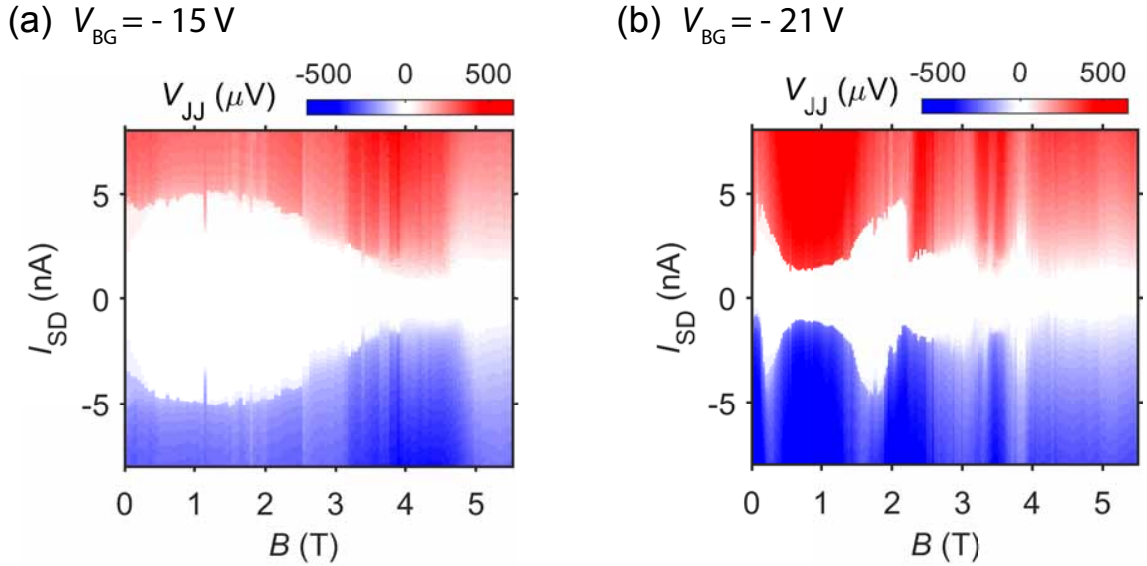


**Figure 7.8.**  $V_{JJ}$  measured as a function of  $I_{SD}$  and  $B$  at: (a)  $V_{BG} = -15 \text{ V}$  and (b)  $V_{BG} = -21 \text{ V}$ .

An overview of the magnetic field dependence of supercurrent is shown in Fig. 7.8(a), where  $V_{JJ}$  is measured as a function of  $I_{SD}$  and  $B$  at a fixed gate voltage of  $V_{BG} = -15 \text{ V}$ . The area with white color corresponds to  $V_{JJ} \approx 0 \text{ V}$ , which means that the system is in the superconducting state, and there is a supercurrent flowing across the junction. The boundary of this white colored area at  $I_{SD} > 0$  reflects the value of  $I_C$ , at which a

transition between the superconducting and normal states takes place. In Fig. 7.8(a), we find a non-monotonic modulation of  $I_C$  with  $B$ , such that with increasing  $B$ ,  $I_C$  first increases and then decreases, with a maximum of  $I_C \approx 5$  nA at  $B = 1.35$  T. Such a non-monotonic behavior is much more pronounced at a different gate voltage of  $V_{BG} = -21$  V, as shown in Fig. 7.8(b). In this figure,  $I_C$  oscillates in  $B$  with a maximum of  $I_C \approx 5$  nA appearing at two different value of  $B$ . These results suggest a clear gate dependence of  $I_C$ . We note that the supercurrent observed in these figures persists within the available magnetic field range of our cryostat, indicating a critical magnetic field of  $B_C > 8$  T at  $T = 20$  mK.

Our result in terms of the enhancement of supercurrent with magnetic field is unusual compared to the experiments reported for Josephson weak links [213, 214]. A microscopic explanation of our result is not clear, but we note that a similar observation has been reported in Ref.[215]. In their work on InAs nanowires coupled to Al leads, an increase of  $I_C$  in the presence of an external magnetic field is demonstrated and explained by considering a magnetic field-induced topological transition in the system.

### 7.2.3. Conclusions

We study induced superconductivity in hBN encapsulated CNT devices with 0D superconducting side contacts made of MoSi. In the limit of an intermediate coupling between the CNT and superconducting leads, we identify characteristic features associated with the quasiparticle tunneling, resonant Andreev tunneling, and Andreev bound states. We introduce a simple resonant tunneling model, and we find a reasonable agreement between the experiment and our model. In a strong coupling regime, we observe subharmonic gap structures with NDC. We attribute these subgap features to coherent MAR in the presence of broadened bound states. Magnetic field dependence of MAR suggests a competition between supercurrent and MAR in magnetic field. Moreover, we find non-monotonic modulation of  $I_C$  in magnetic field, with a large critical current of  $I_C \approx 5$  nA at a large magnetic field of  $B = 1.35$  T. We show that such a non-monotonic behavior of  $I_C$  is also gate tunable.



# 8 Summary and outlook

---

In this thesis, we aim to explore the ideal 1D electronic properties of CNTs by fabricating substrate-bound, disorder-free, and clean devices with outstanding quality. For this purpose, we develop a new fabrication scheme, where we introduce the 2D material hBN as clean substrates for CNT QDs, insulators for top finger gates, tunnel barriers to the CNTs, as well as to encapsulate the CNTs. The resulting hBN-CNT heterostructure devices are further studied by the low-temperature transport spectroscopy to demonstrate an improvement of the device performance.

Our CNT QDs fabricated on hBN flakes using optimized parameters exhibit clear CB diamonds with two-fold periodicity, as expected for clean CNT QDs [34]. The dual-gated CNT device with hBN as a top gate dielectric reveals a characteristic behavior of a clean single QD with a confinement size of  $\sim 1.3 \mu\text{m}$ . These hBN-CNT heterostructures show a very good long term ( $>$ days) electrical stability, i.e., very few gate-dependent and no tempera charge rearrangements, comparable to the best of our CNT QDs fabricated on standard Si/SiO<sub>2</sub> substrates. The fact that a clean single QD with a confinement size of  $1.3 \mu\text{m}$  can be realized is very promising. These findings demonstrate that an improved device quality can be achieved by simply introducing hBN into the system. Our results paves the way to more complex devices based on hBN substrates and gate dielectrics, with more predictable and reproducible characteristics and electronic stability.

For the CNT devices with atomically thin monolayer hBN as tunnel barriers, we use transport spectroscopy to characterize the interactions between parallel-coupled double QDs also in a two-terminal CNT device with only a single global gate [35]. We investigate the avoided crossings resulted from the tunnel and capacitive couplings between the electronic charge states of different QDs. Our results enrich the fundamental understanding of quantum transport through coupled QDs formed in a parallel configuration. The transport spectroscopy reveals a level spacing of  $\delta E \approx 0.9 \text{ meV}$  for both dots, which suggests dot sizes that are considerably larger than the source-drain contact separation. We speculate that the QD wave function can extend beyond the spacing between the source and drain contacts for weakly coupled tunnel contacts (hBN layer). However, the parallel QDs show estimated tunnel coupling strengths that are comparable to those of conventional devices without hBN tunnel barriers. Further investments in this direction suggest that the overall quality of the monolayer hBN films is not consistent and degrades during the transfer process regardless the choice of the transfer techniques. In addition, three-terminal CNT devices with hBN tunnel barriers show hysteresis in their transport characteristics at low temperatures. These results indicate that advancement of current transfer techniques is necessary and plays an essential role for the potential application of atomically thin hBN tunnel barriers in CNT-based heterostructures. Our

work offers a preliminary research step in this perspective.

For the hBN encapsulated CNT devices, we succeed in fabricating 0D side contacts to the ends of the CNT segments with a yield close to 95%. The low-temperature characteristics of the resulting devices demonstrate that clean QDs with confinement sizes determined only by the metal contacts and not by defects in the CNTs can be achieved. We found that 0D side contacts to the ends of the CNT segments offer an ideal approach to electrically contact the multi-shell of a multi-wall CNT with high probability. These results have motivated us to fabricate 0D superconducting side contacts to the hBN encapsulated CNTs, and we have succeeded with MoSi. This has allowed us to investigate the induced superconductivity in end-contacted CNTs. In a device with an intermediate coupling strength, we identify resonant Andreev tunneling through a QD. For a device with a strong coupling to the superconducting leads, we observe subharmonic gap structures with strong NDC dips. We explain these features in terms of coherent MAR in the presence of bound states. Moreover, we study the magnetic field dependence of the supercurrent, and we observe a non-monotonic modulation of  $I_C$  in  $B$ , but a microscopic explanation of this behavior is still not clear.

To understand the magnetic field dependence of the supercurrent, we start to work on superconducting quantum interference devices (SQUID), which consist of hBN encapsulated CNTs with 0D side contacts made of MoSi. As reported in Ref.[216], such a system allows us to study the current-phase relation across the QDs that are coupled to the superconducting leads. In addition, for future work, it is beneficial to integrate atomically thin hBN tunnel barriers and top finger gates into such a system.

# Bibliography

- [1] M. M. Shulaker, G. Hills, N. Patil, H. Wei, H.-Y. Chen, H.-S. P. Wong, and S. Mitra, *Nature* **501**, 526 (2013).
- [2] E. A. Laird, F. Kuemmeth, G. Steele, K. Grove-Rasmussen, J. Nygård, K. Flensberg, and L. P. Kouwenhoven, *Reviews of Modern Physics* **87**, 703 (2015).
- [3] J. Schindele, A. Baumgartner, R. Maurand, M. Weiss, and C. Schönenberger, *Physical Review B* **89**, 045422 (2014).
- [4] W. Liang, M. Bockrath, D. Bozovic, J. H. Hafner, M. Tinkham, and H. Park, *Nature* **411**, 665 (2001).
- [5] C. S. Peça, L. Balents, and K. J. Wiese, *Physical Review B* **68**, 205423 (2003).
- [6] G. A. Steele, G. Gotz, and L. P. Kouwenhoven, *Nature Nanotechnology* **4**, 363 (2009).
- [7] M. Jung, J. Schindele, S. Nau, M. Weiss, A. Baumgartner, and C. Schönenberger, *Nano Letters* **13**, 4522 (2013).
- [8] J. Waissman, M. Honig, S. Pecker, A. Benyamini, A. Hamo, and S. Ilani, *Nature Nanotechnology* **8**, 569 (2013).
- [9] F. Kuemmeth, S. Ilani, D. C. Ralph, and P. L. McEuen, *Nature* **452**, 448 (2008).
- [10] G. A. Steele, F. Pei, E. A. Laird, J. M. Jol, H. B. Meerwaldt, and L. P. Kouwenhoven, *Nature Communication* **4**, 1573 (2013).
- [11] F. Pei, E. A. Laird, G. A. Steele, and L. P. Kouwenhoven, *Nature Nanotechnology* **7**, 630 (2012).
- [12] M. Bockrath, D. H. Cobden, J. Lu, A. G. Rinzler, R. E. Smalley, L. Balents, and P. L. McEuen, *Nature* **397**, 598 (1999).
- [13] V. V. Deshpande and M. Bockrath, *Nature Physics* **4**, 314 (2008).
- [14] S. Pecker, F. Kuemmeth, A. Secchi, M. Rontani, D. C. Ralph, P. L. McEuen, and S. Ilani, *Nature Physics* **9**, 576 (2013).
- [15] J. Cao, Q. Wang, and H. Dai, *Nature Materials* **4**, 745 (2005).
- [16] T. Hertel, R. Martel, and P. Avouris, *The Journal of Physical Chemistry B* **102**, 910 (1998).
- [17] J. Samm, J. Gramich, A. Baumgartner, M. Weiss, and C. Schönenberger, *Journal of Applied Physics* **115**, 174309 (2014).

- [18] D. S. Macintyre, O. Ignatova, S. Thoms, and I. G. Thayne, *Journal of Vacuum Science & Technology B: Microelectronics and Nanometer Structures Processing, Measurement, and Phenomena* **27**, 2597 (2009).
- [19] P. L. McEuen, M. Bockrath, D. H. Cobden, Y.-G. Yoon, and S. G. Louie, *Physical Review Letters* **83**, 5098 (1999).
- [20] M. Bockrath, W. Liang, D. Bozovic, J. H. Hafner, C. M. Lieber, M. Tinkham, and H. Park, *Science* **291**, 283 (2001).
- [21] M. T. Woodside and P. L. McEuen, *Science* **296**, 1098 (2002).
- [22] J. Cao, Q. Wang, D. Wang, and H. Dai, *Small* **1**, 1613 (2005).
- [23] N. R. Franklin, Q. Wang, T. W. Tomblor, A. Javey, M. Shim, and H. Dai, *Applied Physics Letters* **81**, 913 (2002).
- [24] C. Wu, Chung, C. H. Liu, and Z. Zhong, *Nano Letters* **10**, 1032 (2010).
- [25] J. Weissman, M. Honig, S. Pecker, A. Benyamini, A. Hamo, and S. Ilani, *Nature Nanotechnology* **8**, 569 (2013).
- [26] J. J. Viennot, J. Palomo, and T. Kontos, *Applied Physics Letters* **104**, 113108 (2014).
- [27] J. Samm, J. Gramich, A. Baumgartner, M. Weiss, and C. Schönenberger, *Journal of Applied Physics* **115**, 174309 (2014).
- [28] J. Xue, J. Sanchez-Yamagishi, D. Bulmash, P. Jacquod, A. Deshpande, K. Watanabe, T. Taniguchi, P. Jarillo-Herrero, and B. J. LeRoy, *Nature Materials* **10**, 282 (2011).
- [29] S. Engels, A. Epping, C. Volk, S. Korte, B. Voigtländer, K. Watanabe, T. Taniguchi, S. Trellenkamp, and C. Stampfer, *Applied Physics Letters* **103**, 073113 (2013).
- [30] C. R. Dean, A. F. Young, I. Meric, C. Lee, L. Wang, S. Sorgenfrei, K. Watanabe, T. Taniguchi, P. Kim, K. L. Shepard, and J. Hone, *Nature Nanotechnology* **5**, 722 (2010).
- [31] J. S. Ross, P. Klement, A. M. Jones, N. J. Ghimire, J. Yan, D. G. Mandrus, T. Taniguchi, K. Watanabe, K. Kitamura, W. Yao, D. H. Cobden, and X. Xu, *Nature Nanotechnology* **9**, 268 (2014).
- [32] L. Britnell, R. V. Gorbachev, A. K. Geim, L. A. Ponomarenko, A. Mischenko, M. T. Greenaway, T. M. Fromhold, K. S. Novoselov, and L. Eaves, *Nature Communications* **4**, 1794 (2013).
- [33] L. Wang, I. Meric, P. Y. Huang, Q. Gao, Y. Gao, H. Tran, T. Taniguchi, K. Watanabe, L. M. Campos, D. A. Muller, J. Guo, P. Kim, J. Hone, K. L. Shepard, and C. R. Dean, *Science* **342**, 614 (2013).
- [34] A. Baumgartner, G. Abulizi, K. Watanabe, T. Taniguchi, J. Gramich, and C. Schönenberger, *Applied Physics Letters* **105**, 023111 (2014).
- [35] G. Abulizi, A. Baumgartner, and C. Schönenberger, *Physica Status Solidi B* **253**, 2428 (2016).



- 
- [36] E. A. Laird, F. Kuemmeth, G. A. Steele, K. Grove-Rasmussen, J. Nygård, K. Flensberg, and L. P. Kouwenhoven, *Reviews of Modern Physics* **87**, 703 (2015).
- [37] P. R. Wallace, *Phys. Rev.* **71**, 622 (1947).
- [38] A. H. Castro Neto, F. Guinea, N. M. R. Peres, K. S. Novoselov, and A. K. Geim, *Rev. Mod. Phys.* **81**, 109 (2009).
- [39] O. V. Kharissova and B. I. Kharisov, *RSC Adv.* **4**, 30807 (2014).
- [40] J.-C. Charlier, X. Blase, and S. Roche, *Rev. Mod. Phys.* **79**, 677 (2007).
- [41] N. Ooi, A. Rairkar, L. Lindsley, and J. B. Adams, *Journal of Physics: Condensed Matter* **18**, 97 (2006).
- [42] H. Zeng, C. Zhi, Z. Zhang, X. Wei, X. Wang, W. Guo, Y. Bando, and D. Golberg, *Nano Letters* **10**, 5049 (2010).
- [43] O. Hod, *Journal of Chemical Theory and Computation* **8**, 1360 (2012).
- [44] D. R., Y. F., MericI., LeeC., WangL., SorgenfreiS., WatanabeK., TaniguchiT., KimP., S. L., and HoneJ., .
- [45] K. Watanabe, T. Taniguchi, and H. Kanda, *Nature Materials* **3**, 404 (2004).
- [46] A. F. Young, C. R. Dean, I. Meric, S. Sorgenfrei, H. Ren, K. Watanabe, T. Taniguchi, J. Hone, K. L. Shepard, and P. Kim, *Phys. Rev. B* **85**, 235458 (2012).
- [47] J.-W. Huang, C. Pan, S. Tran, B. Cheng, K. Watanabe, T. Taniguchi, C. N. Lau, and M. Bockrath, *Nano Letters* **15**, 6836 (2015).
- [48] I. Jo, M. T. Pettes, J. Kim, K. Watanabe, T. Taniguchi, Z. Yao, and L. Shi, *Nano Letters* **13**, 550 (2013).
- [49] K. S. Novoselov, A. K. Geim, S. V. Morozov, D. Jiang, Y. Zhang, S. V. Dubonos, I. V. Grigorieva, and A. A. Firsov, *Science* **306**, 666 (2004).
- [50] K. K. Kim, A. Hsu, X. Jia, S. M. Kim, Y. Shi, M. Hofmann, D. Nezich, J. F. Rodriguez-Nieva, M. Dresselhaus, T. Palacios, and J. Kong, *Nano Letters* **12**, 161 (2012).
- [51] S. Caneva, R. S. Weatherup, B. C. Bayer, R. Blume, A. Cabrero-Vilatela, P. Braeuninger-Weimer, M.-B. Martin, R. Wang, C. Baehtz, R. Schloegl, J. C. Meyer, and S. Hofmann, *Nano Letters* **16**, 1250 (2016).
- [52] G. Lu, T. Wu, P. Yang, Y. Yang, Z. Jin, W. Chen, S. Jia, H. Wang, G. Zhang, J. Sun, P. M. Ajayan, J. Lou, X. Xie, and M. Jiang, *Advanced Science* **4**, 1700076 (2017), 1700076.
- [53] S. Ilani and P. L. McEuen, *Annual Review of Condensed Matter Physics* **1**, 1 (2010).
- [54] J. Svensson and E. E. B. Campbell, *Journal of Applied Physics* **110**, 111101 (2011).
- [55] W. Monch, *Reports on Progress in Physics* **53**, 221 (1990).

- [56] S. Heinze, J. Tersoff, R. Martel, V. Derycke, J. Appenzeller, and P. Avouris, *Phys. Rev. Lett.* **89**, 106801 (2002).
- [57] W. Kim, A. Javey, R. Tu, J. Cao, Q. Wang, and H. Dai, *Applied Physics Letters* **87**, 1 (2005).
- [58] A. Javey, J. Guo, Q. Wang, M. Lundstrom, and H. Dai, *Nature* **424**, 654 (2003).
- [59] Z. Chen, J. Appenzeller, J. Knoch, Y.-m. Lin, and P. Avouris, *Nano Letters* **5**, 1497 (2005).
- [60] S. Lee, S.-J. Kahng, and Y. Kuk, *Chemical Physics Letters* **500**, 82 (2010).
- [61] V. Vitale, A. Curioni, and W. Andreoni, *Journal of the American Chemical Society* **130**, 5848 (2008).
- [62] X. Cui, M. Freitag, R. Martel, L. Brus, and P. Avouris, *Nano Letters* **3**, 783 (2003).
- [63] K. Grove-Rasmussen, H. Jørgensen, and P. Lindelof, *Physica E: Low-dimensional Systems and Nanostructures* **40**, 92 (2007).
- [64] J. Nygard, D. Cobden, M. Bockrath, P. McEuen, and P. Lindelof, *Applied Physics A* **69**, 297 (1999).
- [65] R. Hanson, L. P. Kouwenhoven, J. R. Petta, S. Tarucha, and L. M. K. Vandersypen, *Rev. Mod. Phys.* **79**, 1217 (2007).
- [66] L. P. Kouwenhoven, D. G. Austing, and S. Tarucha, *Reports on Progress in Physics* **64**, 701 (2001).
- [67] C. W. J. Beenakker, *Phys. Rev. B* **44**, 1646 (1991).
- [68] S. De Franceschi, S. Sasaki, J. M. Elzerman, W. G. van der Wiel, S. Tarucha, and L. P. Kouwenhoven, *Phys. Rev. Lett.* **86**, 878 (2001).
- [69] W. G. van der Wiel, S. De Franceschi, J. M. Elzerman, T. Fujisawa, S. Tarucha, and L. P. Kouwenhoven, *Reviews of Modern Physics* **75**, 1 (2002).
- [70] K. H. Onnes, *Leiden Commun* **124c** (1991).
- [71] W. Meissner and R. Ochsenfeld, *Naturwissenschaften* **21**, 787 (1933).
- [72] F. London and H. London, *Proceedings of the Royal Society of London A: Mathematical, Physical and Engineering Sciences* **149**, 71 (1935).
- [73] J. Bardeen, L. N. Cooper, and J. R. Schrieffer, *Phys. Rev.* **108**, 1175 (1957).
- [74] L. N. Cooper, *Phys. Rev.* **104**, 1189 (1956).
- [75] M. Tinkham, *Introduction to superconductivity*, 2nd ed. (Dover, 2004) .
- [76] B. Pannetier and H. Courtois, *Journal of Low Temperature Physics* **118**, 599 (2000).
- [77] A. F. Andreev, *Soviet Physics JETP* **19**, 1228 (1964).

- 
- [78] G. E. Blonder, M. Tinkham, and T. M. Klapwijk, *Phys. Rev. B* **25**, 4515 (1982).
- [79] P. Recher, E. V. Sukhorukov, and D. Loss, *Phys. Rev. B* **63**, 165314 (2001).
- [80] G. Falci, D. Feinberg, and F. W. J. Hekking, *EPL (Europhysics Letters)* **54**, 255 (2001).
- [81] J. Schindele, A. Baumgartner, and C. Schönenberger, *Phys. Rev. Lett.* **109**, 157002 (2012).
- [82] J. C. Cuevas, A. Martín-Rodero, and A. L. Yeyati, *Phys. Rev. B* **54**, 7366 (1996).
- [83] M. Octavio, M. Tinkham, G. E. Blonder, and T. M. Klapwijk, *Phys. Rev. B* **27**, 6739 (1983).
- [84] T. Klapwijk, G. Blonder, and M. Tinkham, *Physica B+C* **109**, 1657 (1982).
- [85] E. V. Bezuglyi, E. N. Bratus', V. S. Shumeiko, G. Wendin, and H. Takayanagi, *Phys. Rev. B* **62**, 14439 (2000).
- [86] A. Bardas and D. V. Averin, *Phys. Rev. B* **56**, R8518 (1997).
- [87] A. V. Zaitsev and D. V. Averin, *Phys. Rev. Lett.* **80**, 3602 (1998).
- [88] P. Samuelsson, G. Johansson, A. Ingeman, V. S. Shumeiko, and G. Wendin, *Phys. Rev. B* **65**, 180514 (2002).
- [89] T. T. Heikkilä, *The Physics of Nanoelectronics: Transport and Fluctuation Phenomena at Low Temperatures* (Oxford University Press, New York, 1964) .
- [90] L. Bretheau, J. I.-J. Wang, R. Pisoni, K. Watanabe, T. Taniguchi, and P. Jarillo-Herrero, *Nature Physics* **13**, 756 (2017).
- [91] B. Josephson, *Physics Letters* **1**, 251 (1962).
- [92] M. Gaass, S. Pfaller, T. Geiger, A. Donarini, M. Grifoni, A. K. Hüttel, and C. Strunk, *Phys. Rev. B* **89**, 241405 (2014).
- [93] A. L. Yeyati, J. C. Cuevas, A. López-Dávalos, and A. Martín-Rodero, *Phys. Rev. B* **55**, R6137 (1997).
- [94] F. Deon, V. Pellegrini, F. Giazotto, G. Biasiol, L. Sorba, and F. Beltram, *Applied Physics Letters* **98**, 132101 (2011).
- [95] C. B. Whan and T. P. Orlando, *Phys. Rev. B* **54**, R5255 (1996).
- [96] C. W. J. Beenakker, *Phys. Rev. B* **46**, 12841 (1992).
- [97] J. Gramich, A. Baumgartner, and C. Schönenberger, *Phys. Rev. Lett.* **115**, 216801 (2015).
- [98] J. Kong, H. T. Soh, A. M. Cassell, C. F. Quate, and H. Dai, *Nature* **395**, 878 (1998).
- [99] J. Furer, *Ph.D. thesis, University of Basel* (2006).

- [100] X. Li, X. Tu, S. Zaric, K. Welsher, W. S. Seo, W. Zhao, and H. Dai, *Journal of the American Chemical Society* **129**, 15770 (2007).
- [101] M. Altissimo, *Biomicrofluidics* **4**, 026503 (2010).
- [102] A. S. Gangnaik, Y. M. Georgiev, and J. D. Holmes, *Chemistry of Materials* **29**, 1898 (2017).
- [103] J. W. Suk, A. Kitt, C. W. Magnuson, Y. Hao, S. Ahmed, J. An, A. K. Swan, B. B. Goldberg, and R. S. Ruoff, *ACS Nano* **5**, 6916 (2011).
- [104] T. Hasler, M. Jung, V. Ranjan, G. Puebla-Hellmann, A. Wallraff, and C. Schönenberger, *Physical Review Applied* **4**, 054002 (2015).
- [105] L. Wang, I. Meric, P. Y. Huang, Q. Gao, Y. Gao, H. Tran, T. Taniguchi, K. Watanabe, L. M. Campos, D. A. Muller, J. Guo, P. Kim, J. Hone, K. L. Shepard, and C. R. Dean, *Science* **342**, 614 (2013).
- [106] D. Mann, A. Javey, J. Kong, Q. Wang, and H. Dai, *Nano Letters* **3**, 1541 (2003).
- [107] A. Banerjee, L. J. Baker, A. Doye, M. Nord, R. M. Heath, K. Erotokritou, D. Bosworth, Z. H. Barber, I. MacLaren, and R. H. Hadfield, *Superconductor Science and Technology* **30**, 084010 (2017).
- [108] D. Bosworth, S.-L. Sahonta, R. H. Hadfield, and Z. H. Barber, *American Institute of Physics Advances* **5**, 087106 (2015).
- [109] A. Edelstein, S. Ovshinsky, H. Sadate-Akhavi, and J. Wood, *Solid State Communications* **41**, 139 (1982).
- [110] L. Gao, W. Ren, H. Xu, L. Jin, Z. Wang, T. Ma, L.-P. Ma, Z. Zhang, Q. Fu, L.-M. Peng, X. Bao, and H.-M. Cheng, *Nature Communications* **3**, 699 (2012).
- [111] M. Ishigami, J. H. Chen, W. G. Cullen, M. S. Fuhrer, and E. D. Williams, *Nano Letters* **7**, 1643 (2007).
- [112] A. Nourbakhsh, M. Cantoro, A. Klekachev, F. Clemente, B. Sorée, M. H. van der Veen, T. Vosch, A. Stesmans, B. Sels, and S. De Gendt, *The Journal of Physical Chemistry C* **114**, 6894 (2010).
- [113] Z. Cheng, Q. Zhou, C. Wang, Q. Li, C. Wang, and Y. Fang, *Nano Letters* **11**, 767 (2011).
- [114] J.-N. Longchamp, C. Escher, and H.-W. Fink, *Journal of Vacuum Science & Technology B, Nanotechnology and Microelectronics: Materials, Processing, Measurement, and Phenomena* **31**, 020605 (2013).
- [115] C. Enss and S. Hunklinger, (Springer, 2005).
- [116] H. Bluhm and K. A. Moler, *Review of Scientific Instruments* **79**, 014703 (2008).
- [117] H. Aurich, Ph.D. thesis, University of Basel (2012).

- 
- [118] Y. Homma, S. Suzuki, Y. Kobayashi, and M. Nagase, *Applied Physics Letters* **84**, 1750 (2004).
- [119] R. Y. Zhang, Y. Wei, L. A. Nagahara, I. Amlani, and R. K. Tsui, *Nanotechnology* **17**, 272 (2006).
- [120] I. A. Glavatskikh, V. S. Kortov, and H.-J. Fitting, *Journal of Applied Physics* **89**, 440 (2001).
- [121] Yu. A. Kasumov, I. I. Khodos, M. Kociak, and A. Yu. Kasumov, *Applied Physics Letters* **89**, 013120 (2006).
- [122] D. Golla, K. Chattrakun, K. Watanabe, T. Taniguchi, B. J. LeRoy, and A. Sandhu, *Applied Physics Letters* **102**, 161906 (2013).
- [123] R. V. Gorbachev, I. Riaz, R. R. Nair, R. Jalil, L. Britnell, B. D. Belle, E. W. Hill, K. S. Novoselov, K. Watanabe, T. Taniguchi, A. K. Geim, and P. Blake, *Small* **7**, 465 (2011).
- [124] X. Li, X. Tu, S. Zaric, K. Welsher, W. S. Seo, W. Zhao, and H. Dai, *Journal of the American Chemical Society* **129**, 15770 (2007).
- [125] For CNT QDs, the source and drain capacitances can usually not be neglected and the often used formulas for a cylinder capacitor cannot be applied directly.
- [126] J. Nygård, D. H. Cobden, M. Bockrath, P. L. McEuen, and P. E. Lindelof, *Applied Physics A* **69**, 297 (1999).
- [127] T. Ihn, *Oxford University Press* (2010).
- [128] C. Morgan, M. Misiorny, D. Metten, S. Heedt, T. Schäpers, C. M. Schneider, and C. Meyer, *Phys. Rev. Applied* **5**, 054010 (2016).
- [129] H. W. C. Postma, M. de Jonge, Z. Yao, and C. Dekker, *Physical Review B* **62**, R10653 (2000).
- [130] H. Tomizawa, T. Yamaguchi, S. Akita, and K. Ishibashi, *Journal of Applied Physics* **118**, 044306 (2015).
- [131] M. Gurram, S. Omar, S. Zihlmann, P. Makk, C. Schönenberger, and B. J. van Wees, *Phys. Rev. B* **93**, 115441 (2016).
- [132] W. Fu, P. Makk, R. Maurand, M. Bräuninger, and C. Schönenberger, *Journal of Applied Physics* **116**, 074306 (2014).
- [133] L. Britnell, R. V. Gorbachev, R. Jalil, B. D. Belle, F. Schedin, M. I. Katsnelson, L. Eaves, S. V. Morozov, A. S. Mayorov, N. M. R. Peres, A. H. Castro Neto, J. Leist, A. K. Geim, L. A. Ponomarenko, and K. S. Novoselov, *Nano Letters* **12**, 1707 (2012).
- [134] F. Amet, J. R. Williams, A. G. F. Garcia, M. Yankowitz, K. Watanabe, T. Taniguchi, and D. Goldhaber-Gordon, *Physical Review B* **85**, 073405 (2012).
- [135] G.-H. Lee, Y.-J. Yu, C. Lee, C. Dean, K. L. Shepard, P. Kim, and J. Hone, *Applied Physics Letters* **99**, 243114 (2011).

- [136] J. Gramich, A. Baumgartner, and C. Schönenberger, *Physical Review Letters* **115**, 216801 (2015).
- [137] A. Benyamini, A. Hamo, S. V. Kusminskiy, F. von Oppen, and S. Ilani, *Nature Physics* **10**, 151 (2014).
- [138] H. Aurich, A. Baumgartner, F. Freitag, A. Eichler, J. Trbovic, and C. Schönenberger, *Applied Physics Letters* **97**, 153116 (2010).
- [139] S. Sahoo, T. Kontos, J. Furer, C. Hoffmann, M. Gräber, A. Cottet, and C. Schönenberger, *Nature Physics* **1**, 99 (2005).
- [140] C. Schönenberger, A. Bachtold, C. Strunk, J.-P. Salvetat, and L. Forró, *Applied Physics A* **69**, 283 (1999).
- [141] L. Langer, V. Bayot, E. Grivei, J.-P. Issi, J. P. Heremans, C. H. Olk, L. Stockman, C. Van Haesendonck, and Y. Bruynseraede, *Physical Review Letters* **76**, 479 (1996).
- [142] J. Klinovaja and D. Loss, *Physical Review Letters* **110**, 126402 (2013).
- [143] Y. Miyamoto, S. Saito, and D. Tománek, *Physical Review B* **65**, 041402 (2001).
- [144] A. K. Hüttel, S. Ludwig, H. Lorenz, K. Eberl, and J. P. Kotthaus, *Physica E: Low-dimensional Systems and Nanostructures* **34**, 488 (2006).
- [145] T. H. Oosterkamp, T. Fujisawa, W. G. van der Wiel, K. Ishibashi, R. V. Hijman, S. Tarucha, and L. P. Kouwenhoven, *Nature* **395**, 873 (1998).
- [146] M. Jung, J. Schindele, S. Nau, M. Weiss, A. Baumgartner, and C. Schönenberger, *Nano Letters* **13**, 4522 (2013).
- [147] M. R. Gräber, W. A. Coish, C. Hoffmann, M. Weiss, J. Furer, S. Oberholzer, D. Loss, and C. Schönenberger, *Physical Review B* **74**, 075427 (2006).
- [148] S. Sapmaz, C. Meyer, P. Beliczynski, P. Jarillo-Herrero, and L. P. Kouwenhoven, *Nano Letters* **6**, 1350 (2006).
- [149] M. R. Buitelaar, J. Fransson, A. L. Cantone, C. G. Smith, D. Anderson, G. A. C. Jones, A. Ardavan, A. N. Khlobystov, A. A. R. Watt, K. Porfyrakis, and G. A. D. Briggs, *Physical Review B* **77**, 245439 (2008).
- [150] H. W. Liu, T. Fujisawa, Y. Ono, H. Inokawa, A. Fujiwara, K. Takashina, and Y. Hirayama, *Physical Review B* **77**, 073310 (2008).
- [151] A. C. Johnson, J. R. Petta, C. M. Marcus, M. P. Hanson, and A. C. Gossard, *Physical Review B* **72**, 165308 (2005).
- [152] E. A. Laird, F. Pei, and L. P. Kouwenhoven, *Nature Nanotechnology* **8**, 565 (2013).
- [153] L.-J. Wang, G.-P. Guo, D. Wei, G. Cao, T. Tu, M. Xiao, G.-C. Guo, and A. M. Chang, *Applied Physics Letters* **99**, 112117 (2011).
- [154] S. Datta, S. Wang, C. Tilmaciu, E. Flahaut, L. Marty, M. Grifoni, and W. Wernsdorfer, *Physical Review B* **84**, 035408 (2011).

- 
- [155] S. Moon, W. Song, J. S. Lee, N. Kim, J. Kim, S.-G. Lee, and M.-S. Choi, *Physical Review Letters* **99**, 176804 (2007).
- [156] K. Goß, M. Leijnse, S. Smerat, M. R. Wegewijs, C. M. Schneider, and C. Meyer, *Physical Review B* **87**, 035424 (2013).
- [157] S.-H. Kang, G. Kim, and Y.-K. Kwon, *Physical Chemistry Chemical Physics* **17**, 5072 (2015).
- [158] J. Gramich, A. Baumgartner, M. Muoth, C. Hierold, and C. Schönenberger, *physica status solidi (b)* **252**, 2496 (2015).
- [159] X. Li, W. Cai, J. An, S. Kim, J. Nah, D. Yang, R. Piner, A. Velamakanni, I. Jung, E. Tutuc, S. K. Banerjee, L. Colombo, and R. S. Ruoff, *Science* **324**, 1312 (2009).
- [160] S. G. Lemay, J. W. Janssen, M. van den Hout, M. Mooij, M. J. Bronikowski, P. A. Willis, R. E. Smalley, L. P. Kouwenhoven, and C. Dekker, *Nature* **412**, 617 (2001).
- [161] J. Cao, Q. Wang, and H. Dai, *Nature Materials* **4**, 745 (2005).
- [162] F. Mahvash, S. Eissa, T. Bordjiba, A. C. Tavares, T. Szkopek, and M. Siaj, *Scientific Reports* **7**, 1 (2017).
- [163] R. V. Gorbachev, I. Riaz, R. R. Nair, R. Jalil, L. Britnell, B. D. Belle, E. W. Hill, K. S. Novoselov, K. Watanabe, T. Taniguchi, A. K. Geim, and P. Blake, *Small* **7**, 465 (2011).
- [164] L. Song, L. Ci, H. Lu, P. B. Sorokin, C. Jin, J. Ni, A. G. Kvashnin, D. G. Kvashnin, J. Lou, B. I. Yakobson, and P. M. Ajayan, *Nano Letters* **10**, 3209 (2010).
- [165] Y. Shi, C. Hamsen, X. Jia, K. K. Kim, A. Reina, M. Hofmann, A. L. Hsu, K. Zhang, H. Li, Z.-Y. Juang, M. S. Dresselhaus, L.-J. Li, and J. Kong, *Nano Letters* **10**, 4134 (2010).
- [166] Y. Chen, X.-L. Gong, and J.-G. Gai, *Advanced Science* **3**, 1500343 (2016).
- [167] H. G. Ong, J. W. Cheah, L. Chen, H. TangTang, Y. Xu, B. Li, H. Zhang, L.-J. Li, and J. Wang, *Applied Physics Letters* **93**, 093509 (2008).
- [168] A. Robert-Peillard and S. V. Rotkin, *IEEE Trans. Nanotechnol.* **4**, 284 (2005).
- [169] M. S. Fuhrer, B. M. Kim, T. Dürkop, and T. Brintlinger, *Nano Letters* **2**, 755 (2002).
- [170] H. Wang, Y. Wu, C. Cong, J. Shang, and T. Yu, *ACS Nano* **4**, 7221 (2010).
- [171] S. Yuan, Q. Zhang, D. Shimamoto, H. Muramatsu, T. Hayashi, Y. A. Kim, and M. Endo, *Applied Physics Letters* **91**, 143118 (2007).
- [172] A. Vijayaraghavan, S. Kar, C. Soldano, S. Talapatra, O. Nalamasu, and P. M. Ajayan, *Applied Physics Letters* **89**, 162108 (2006).
- [173] R. S. Park, G. Hills, J. Sohn, S. Mitra, M. M. Shulaker, and H.-S. P. Wong, *ACS Nano* **11**, 4785 (2017).

- [174] S. H. Jin, A. E. Islam, T.-i. Kim, J.-h. Kim, M. A. Alam, and J. A. Rogers, *Advanced Functional Materials* **22**, 2276 (2012).
- [175] W. Kim, A. Javey, O. Vermesh, Q. Wang, Y. Li, and H. Dai, *Nano Letters* **3**, 193 (2003).
- [176] U. Chandni, K. Watanabe, T. Taniguchi, and J. P. Eisenstein, *Nano Letters* **15**, 7329 (2015).
- [177] L. Ju, J. V. Jr, E. Huang, S. Kahn, C. Nosiola, H.-Z. Tsai, W. Yang, T. Taniguchi, K. Watanabe, Y. Zhang, G. Zhang, A. Z. M. Crommie, and F. Wang, *Nature Nanotechnology* **9**, 348 (2014).
- [178] C. Attacalite, M. Bockstedte, A. Marini, A. Rubio, and L. Wirtz, *Physical Review B* **83**, 144115 (2011).
- [179] Y. Roh, K. Kim, and D. Jung, *Japanese Journal of Applied Physics* **36**, L1681 (1997).
- [180] S. Kar, A. Vijayaraghavan, C. Soldano, S. Talapatra, R. Vajtai, O. Nalamasu, and P. M. Ajayan, *Applied Physics Letters* **89**, 132118 (2006).
- [181] M. Zdrojek, T. Mélin, C. Boyaval, D. Stiévenard, B. Jouault, M. Wozniak, A. Huczko, W. Gebicki, and L. Adamowicz, *Applied Physics Letters* **86**, 213114 (2005).
- [182] X. Liang, B. A. Sperling, I. Calizo, G. Cheng, C. A. Hacker, Q. Zhang, Y. Obeng, K. Yan, H. Peng, Q. Li, X. Zhu, H. Yuan, A. R. Hight Walker, Z. Liu, L.-m. Peng, and C. A. Richter, *ACS Nano* **5**, 9144 (2011).
- [183] S. C. Lim, J. H. Jang, D. J. Bae, G. H. Han, S. Lee, I.-S. Yeo, and Y. H. Lee, *Applied Physics Letters* **95**, 264103 (2009).
- [184] C. Lan, D. N. Zakharov, and R. G. Reifengerger, *Applied Physics Letters* **92**, 213112 (2008).
- [185] A. V. Kretinin, Y. Cao, J. S. Tu, G. L. Yu, R. Jalil, K. S. Novoselov, S. J. Haigh, A. Gholinia, A. Mishchenko, M. Lozada, T. Georgiou, C. R. Woods, F. Withers, P. Blake, G. Eda, A. Wirsig, C. Hucho, K. Watanabe, T. Taniguchi, A. K. Geim, and R. V. Gorbachev, *Nano Letters* **14**, 3270 (2014).
- [186] T. Chu and Z. Chen, *ACS Nano* **8**, 3584 (2014).
- [187] Q. Gao and J. Guo, *APL Materials* **2**, 056105 (2014).
- [188] G.-H. Lee, X. Cui, Y. D. Kim, G. Arefe, X. Zhang, C.-H. Lee, F. Ye, K. Watanabe, T. Taniguchi, P. Kim, and J. Hone, *ACS Nano* **9**, 7019 (2015).
- [189] L. Wang, Y. Pu, A. K. Soh, Y. Shi, and S. Liu, *AIP Advances* **6**, 125126 (2016).
- [190] L. H. Li, E. J. G. Santos, T. Xing, E. Cappelluti, R. Roldán, Y. Chen, K. Watanabe, and T. Taniguchi, *Nano Letters* **15**, 218 (2015).
- [191] Y. Tomio, H. Suzuura, and T. Ando, *Physical Review B* **85**, 085411 (2012).
- [192] P. W. Anderson and J. M. Rowell, *Phys. Rev. Lett.* **10**, 230 (1963).



- 
- [193] D. B. Szombati, S. Nadj-Perge, D. Car, S. R. Plissard, E. P. A. M. Bakkers, and L. P. Kouwenhoven, *Nature Physics* **12**, 568 (2016).
- [194] V. E. Calado, S. Goswami, G. Nanda, M. Diez, A. R. Akhmerov, K. Watanabe, T. Taniguchi, T. M. Klapwijk, and L. M. K. Vandersypen, *Nature Physics* **10**, 761 (2015).
- [195] T. Schäpers, V. A. Guzenko, R. P. Müller, A. A. Golubov, A. Brinkman, G. Crecelius, A. Kaluza, and H. Lüth, *Phys. Rev. B* **67**, 014522 (2003).
- [196] C. Ryu, P. W. Blackburn, A. A. Blinova, and M. G. Boshier, *Phys. Rev. Lett.* **111**, 205301 (2013).
- [197] J. Clarke and F. K. Wilhelm, *Nature* **453**, 1031 (2008).
- [198] J. Gramich, A. Baumgartner, and C. Schönenberger, *Applied Physics Letters* **108**, 172604 (2016).
- [199] J.-D. Pillet, C. H. L. Quay, P. Morfin, C. Bena, A. L. Yeyati, and P. Joyez, *Nature Physics* **6**, 965 (2010).
- [200] E. Pallecchi, M. Gaaß, D. A. Ryndyk, and C. Strunk, *Applied Physics Letters* **93**, 072501 (2008).
- [201] P. Jarillo-Herrero, J. A. van Dam, and L. P. Kouwenhoven, *Nature* **439**, 953 (2006).
- [202] A. Y. Kasumov, R. Deblock, M. Kociak, B. Reulet, H. Bouchiat, I. I. Khodos, Y. B. Gorbatov, V. T. Volkov, C. Journet, and M. Burghard, *Science* **284**, 1508 (1999).
- [203] H. A. Nilsson, P. Samuelsson, P. Caroff, and H. Q. Xu, *Nano Letters* **12**, 228 (2012).
- [204] H. I. Jørgensen, K. Grove-Rasmussen, K. Flensberg, and P. E. Lindelof, *Phys. Rev. B* **79**, 155441 (2009).
- [205] M. Takeda and K. Nishigaki, “Magnetic field dependence of critical current density of nbti thin films as a parameter of angle,” in *Advances in Superconductivity XI: Proceedings of the 11th International Symposium on Superconductivity (ISS '98), November 16 – 19, 1998, Fukuoka*, edited by N. Koshizuka and S. Tajima (Springer Japan, Tokyo, 1999) p. 533.
- [206] S. Kubo, *Journal of Applied Physics* **63**, 2033 (1988).
- [207] Y.-J. Doh, S. D. Franceschi, E. P. A. M. Bakkers, and L. P. Kouwenhoven, *Nano Letters* **8**, 4098 (2008).
- [208] J.-D. Pillet, P. Joyez, R. Žitko, and M. F. Goffman, *Phys. Rev. B* **88**, 045101 (2013).
- [209] R. C. Dynes, V. Narayanamurti, and J. P. Garno, *Phys. Rev. Lett.* **41**, 1509 (1978).
- [210] D. M. Gokhfeld, *Superconductor Science and Technology* **20**, 62 (2007).
- [211] A. Ingerman, G. Johansson, V. S. Shumeiko, and G. Wendin, *Phys. Rev. B* **64**, 144504 (2001).

- [212] H. Courtois, M. Meschke, J. T. Peltonen, and J. P. Pekola, *Phys. Rev. Lett.* **101**, 067002 (2008).
- [213] J. Paajaste, M. Amado, S. Roddaro, F. S. Bergeret, D. Ercolani, L. Sorba, and F. Giazotto, *Nano Letters* **15**, 1803 (2015).
- [214] S. Abay, H. Nilsson, F. Wu, H. Xu, C. Wilson, and P. Delsing, *Nano Letters* **12**, 5622 (2012).
- [215] J. Tiira, E. Strambini, M. Amado, S. Roddaro, P. San-Jose, R. Aguado, F. S. Bergeret, D. Ercolani, L. Sorba, and F. Giazotto, *Nature Communications* **8**, 14984 (2017).
- [216] J.-P. Cleuziou, W. Wernsdorfer, V. Bouchiat, T. Ondarçuhu, and M. Monthieux, *Nature Physics* **1**, 53 (2006).
- [217] J. Gramich, A. Baumgartner, and C. Schönenberger, *Applied Physics Letters* **108**, 172604 (2016).
- [218] Y. Cohen, Y. Ronen, J.-H. Kang, M. Heiblum, D. Feinberg, R. Mélin, and H. Shtrikman, [arXiv:1606.08436](https://arxiv.org/abs/1606.08436) (2016).

# A Fabrication recipes

---

## Wafer characteristics

- Wafer type 1 :
  - Heavily boron-doped Si wafer
  - Resistivity: 0.3-0.5  $\Omega\text{cm}$
  - 300 nm thick thermally grown  $\text{SiO}_2$  on top
- Wafer type 2 :
  - Heavily boron-doped Si wafer
  - Resistivity: 0.002-0.005  $\Omega\text{cm}$
  - 400 nm thick thermally grown  $\text{SiO}_2$  to top
- Wafer type 3 :
  - Heavily boron-doped Si wafer
  - Resistivity: 15-25  $\Omega\text{cm}$
  - 200 nm thick low-pressure CVD grown  $\text{Si}_3\text{N}_4$  on top
- Wafer type 4 :
  - Undoped Si wafer
  - Resistivity  $> 5000 \Omega\text{cm}$
  - 170 nm thick thermally grown  $\text{SiO}_2$  on top

## Catalyst solution

- Preparation of stock solutions:
  - 30 mg of  $\text{Al}_2\text{O}_3$  solved in 20 ml IPA and sonicated for 2 h.
  - 93 mg of  $\text{Fe}(\text{NO}_3)_3 \cdot 9\text{H}_2\text{O}$  solved in 20 ml IPA and sonicated for 2 h.
  - 48 mg of  $\text{RuCl}_3 \cdot \text{H}_2\text{O}$  solved in 20 ml IPA and sonicated for 2 h for Ru/Fe catalyst or 27 mg of  $\text{MoO}_2\text{Cl}_2$  solved in 20 ml IPA and sonicated for 2 h for Mo/Fe catalyst.

- Preparation of diluted catalyst solution (here, dilution ratio of 1:12):
    - Mix 0.5 ml of each stock solution and add 18.5 ml IPA, then sonicate for 3 h.
- The CNT density on a growth substrate ( $\text{SiO}_2$ ) can be effectively tuned by changing the amount of IPA. We achieve desired densities by adding 38-75 ml IPA.

### **CNT growth**

- Sonicate catalyst solution for 4 h in pulsed high power sonicator with 100% power, 0.5 s pulse duration, and 0.5 s pause to break up catalysts clusters.
- Spin coat 1-2 droplets of catalyst solution on a growth substrate with 4000 rpm for 40 s.
- Place the growth substrate in the middle of a quartz tube of CVD reactor.
- Check the leak tightness and set the flow rate for Ar,  $\text{CH}_4$  and  $\text{H}_2$  to 1500 sccm (105 l/h at the flow meter), 1000 sccm (45 l/h at the flow meter), 500 sccm (8 l/h at the flow meter), respectively.
- Heat up the furnace to 850°C for Ru/Fe catalyst or 950°C for Mo/Fe catalyst under Ar and  $\text{H}_2$  flow.
- Start the growth by replacing Ar flow with  $\text{CH}_4$  and stay for 10 min.
- Stop the growth by replacing  $\text{CH}_4$  flow with Ar flow and switching off the furnace heating, cool down the system under Ar and  $\text{H}_2$  flow.
- Switch off all gas flow at  $T < 250^\circ\text{C}$  and take out the growth substrate.

### **Alignment markers and Pd contacts**

- Spin coat 300 nm thick ZEP resist with 4000 rpm for 40 s, bake at 180°C for 3 min.
- Electron-beam lithography: 20 kV and 68  $\mu\text{C}/\text{cm}^2$ .
- Develop in n-amyl acetate for 1 min, stop the development in 9:1 mixture of MIBK and IPA for 10 s, rinse in IPA for 20 s.
- Evaporate 5 nm/45 nm thick Ti/Au for alignment markers or 80 nm Pd for electrical contacts, lift-off in NMP at 70°C for 30 min, rinse in IPA at 45°C for 10 min.

### **CNT stamp**

- Spin coat 1.1  $\mu\text{m}$  thick PMMA with 4000 rpm for 40 s, bake at 180°C for 10 min.
- Spin coat 1  $\mu\text{m}$  thick HSQ with 6000 rpm for 60 s, bake at 90°C for 5 min.
- Electron-beam lithography: 20 kV and 200  $\mu\text{C}/\text{cm}^2$ .
- Develop in TMAH (25% solution) for 25 s, stop the development in DI water.

- 
- PMMA removal with O<sub>2</sub> plasma etching in RIE: 16 sccm, 250 mTorr, and 100 W.
  - SiO<sub>2</sub> removal with HF etching
  - Si etching with SF<sub>6</sub>/O<sub>2</sub> plasma in RIE: 50 sccm of SF<sub>6</sub>, 5 sccm of O<sub>2</sub>, 75 mTorr, and 100 W
  - PMMA removal in acetone and IPA at 45°C.
  - Cut the wafer into small pieces of 2 × 2 mm<sup>2</sup> size per piece.
  - CNT growth with Mo/Fe catalyst at 950°C for 10 min in a CVD reactor.

### **hBN etching**

- hBN etching with SF<sub>6</sub>/Ar/O<sub>2</sub> plasma in RIE: 20 sccm of SF<sub>6</sub>, 5 sccm of Ar, 5 sccm of O<sub>2</sub>, 25 mTorr, and 50 W.
- hBN etching with CHF<sub>3</sub>/O<sub>2</sub> plasma in RIE: 40 sccm of CHF<sub>3</sub>, 4 sccm of O<sub>2</sub>, 60 mTorr, and 60 W.

### **Re markers**

- Electron-beam lithography with 300 nm thick PMMA: 20 kV and 240 μC/cm<sup>2</sup>.
- Anisotropic reactive ion etching of SiO<sub>2</sub> in ICP: 30 sccm of CF<sub>4</sub>, 50 W of ICP, and 45 W of RF.
- Re sputtering with Ar plasma: 40 sccm of Ar, 4 mTorr, and 50 W.
- Lift-off in acetone for 5 min.

### **MoSi sputtering**

- Mo and Si co-sputtering with Ar plasma: 20 sccm of Ar, 2 mTorr, 120 W of Si, and 55 W of Mo with stage rotation on.



# B Additional data to Chapter 5

---

## Finite bias spectroscopy

In the device discussed here, a  $9\ \mu\text{m}$  long CNT is contacted by  $200\ \text{nm}$  wide electrodes that are separated by  $300\ \text{nm}$ . At room temperature, the device has a two-terminal resistance of  $4\ \text{M}\Omega$  at  $V_{\text{BG}} = 0\ \text{V}$ . The low-temperature electrical transport properties are characterized in a  $^3\text{He}$  refrigerator at a base temperature of  $\sim 240\ \text{mK}$ , and we apply an ac voltage of  $\delta V = 25\ \mu\text{V}$  at a frequency of  $287.7\ \text{Hz}$ . We measure  $G$  as a function of  $V_{\text{BG}}$  and  $V_{\text{SD}}$ , and a resulting colorscale plot is shown in Fig. B.1. In this figure, we find strongly distorted CB diamonds, which indicate the formation of QDs in the CNT. We repeat the same analysis presented in the first part of chapter 5, and we find two sets of CB diamonds, as indicated by the dashed blue and black lines in Fig. B.1. This suggests the presence of two QDs in parallel configuration. We estimate the charging energies of individual QDs as  $E_{\text{C1}} \approx 10.3\ \text{meV}$  and  $E_{\text{C2}} \approx 3.4\ \text{meV}$ . The extracted capacitances of each QD are listed in Table B.1. We find very similar values for  $C_{\text{S}}$  and  $C_{\text{D}}$  of individual QDs, indicating a symmetric capacitive coupling of each QD to the source-drain contacts. However,  $C_{\text{S}}$  and  $C_{\text{D}}$  of QD2 is about 5 times larger than that of QD1. We note that both BG capacitances are roughly similar. In addition, we obtain upper limits for the tunneling coupling strengths, which yield  $\Gamma_1 \leq 130\ \mu\text{eV}$  and  $\Gamma_2 \leq 100\ \mu\text{eV}$ . We also observe excited state resonances with level spacings of  $\delta E_1 \approx 0.45\ \text{meV}$  and  $\delta E_2 \approx 0.35\ \text{meV}$ . If we assume  $\delta E = \hbar v_{\text{F}}/2L$ , we get estimated QD sizes of  $L_1 \approx 3.6\ \mu\text{m}$  and  $L_2 \approx 4.6\ \mu\text{m}$ , which are significantly larger than the source-drain contact spacing. This finding suggests that the QD confinement is determined not by the source-drain contacts but most likely by the end of the CNT or by very few potential fluctuations, in good agreement with our exceptions.

We now turn to the shape of the CB diamonds. The edges of the CB diamonds are not straight lines but have curvatures, as indicated by the green arrows in Fig. B.1, and we find avoided crossings at the intersection points, i.e., AC1, AC2, AC3, and AC4. We understand that a hybridization of the QD wave functions in an interacting parallel DQD system can give rise to an avoided crossing in their spectrum and the bending of the resonances stems from the inter-dot tunnel coupling, as discussed in the first part of chapter 5. Here, we don't intend to repeat the details of our discussions. Instead, we focus on extracting the inter-dot coupling parameters, i.e.,  $\Delta V_{\text{t1}}$  and  $C_{12}$ . We obtain a lower limit for the tunnel coupling  $\Gamma_{12} > 565\ \mu\text{eV}$  and an inter-dot capacitance  $C_{12} \approx 0.6\ \text{aF}$ , as summarized in Table B.1.

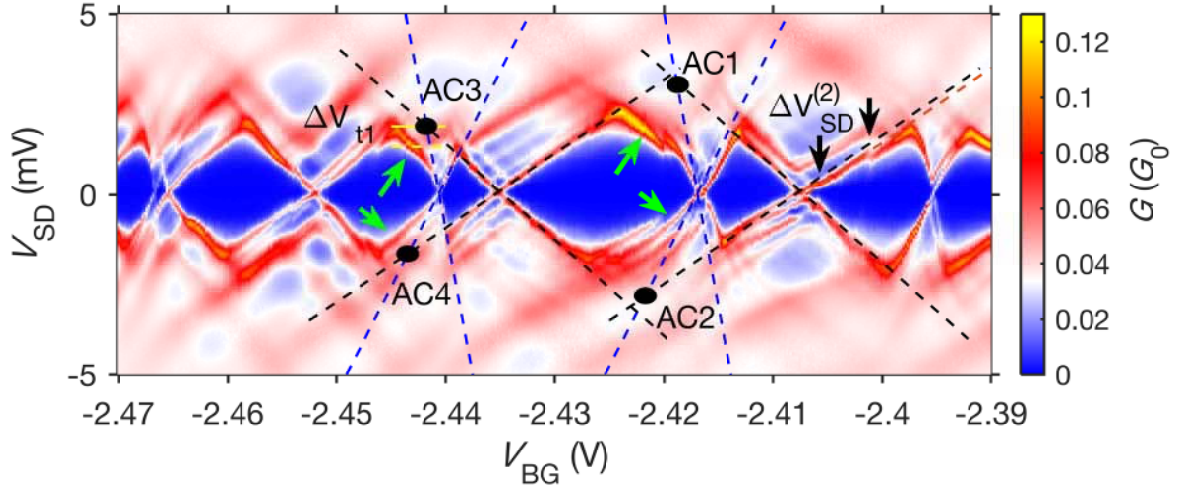


**Figure B.1.** Differential conductance  $G$  measured as a function of  $V_{BG}$  and  $V_{SD}$  at  $T = 240$  mK. Blue and black diamonds correspond to QD1 and QD2, respectively. AC1, AC2, AC3, and AC4 point out four avoided crossings. The black arrows indicate the shift of the diamond edge.  $\Delta V_{t1}$  and  $\Delta V_{SD}^{(2)}$  reflect the inter-dot couplings.

**Table B.1.** Extracted parameters for QD1 and QD2

parameters	QD1 (blue lines)	QD2 (black lines)
$C_{tot}$	15.6 aF	46.5 aF
$C_{BG}$	6.8 aF	5.8 aF
$C_S$	4.2 aF	18.2 aF
$C_D$	4.6 aF	22.5 aF
$\Gamma$	130 $\mu$ eV	100 $\mu$ eV
$C_{12}$		$\sim 0.6$ aF
$\Gamma_{12}$		$> 565$ $\mu$ eV

## Conclusion

In chapter 5, we have presented the low-temperature transport characteristics of a two-terminal device made with hBN film that is from the “old batch” delivered by Graphene Supermarket. In comparison, the device with similar structure but made with hBN film provided by our collaborator is discussed above. The hBN films provided by our collaborator generally show better qualities than the ones purchased from Graphene Supermarket. One would expect to see difference in their electronic transport characteristics. However, their low-temperature transport characteristics are surprisingly similar, i.e. parallel DQD with strong inter-dot coupling. These two devices have similar geometries by design, but the selected CNTs have different lengths. To some extent, this suggests that our experimental results are reproducible from one batch to another. However, we still lack control over the number of QDs formed in the system, and there is no conclusive evidence that can prove the presence of hBN tunnel barriers in the system. In contrast, a clean single QD with large confinement size could offer an ideal platform for precise characterization and identification of hBN tunnel barriers.



# C Additional data to Chapter 7

## Temperature dependence

Figure C.1 shows the differential conductance  $G$  measured as a function of  $V_{SD}$  and  $V_{BG}$  at three different temperatures. The quasiparticle tunneling, resonant Andreev tunneling, and Andreev bound states are clearly visible up to  $T = 1$  K. At  $T = 4.4$  K, additional lines that are running parallel to the CB diamond edges with negative slope appear. We ascribe these resonance lines to thermally activated quasiparticle transport. We note that a similar feature has been reported previously in Refs.[92, 217].

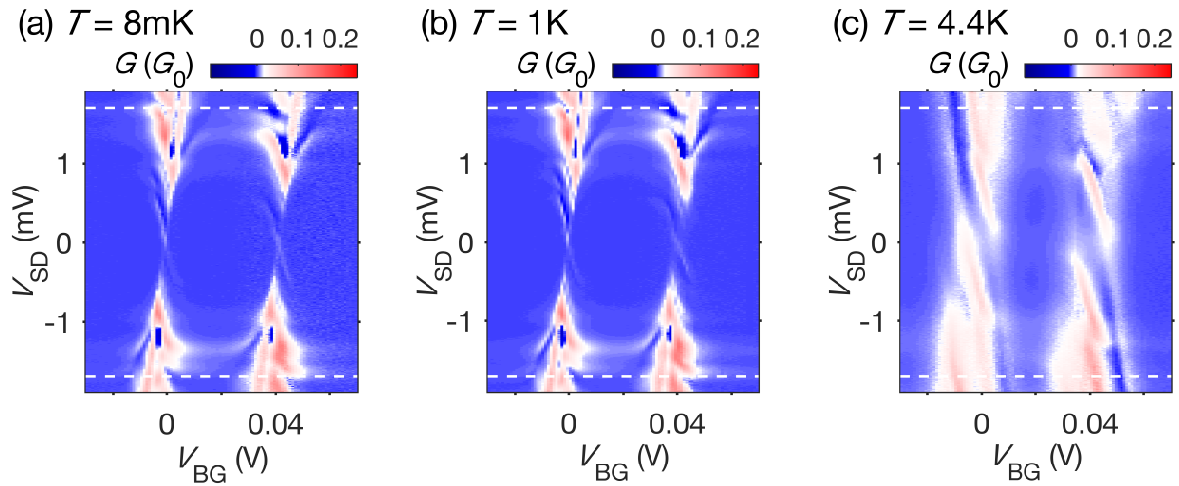


**Figure C.1.** The differential conductance  $G$  plotted as a function of  $V_{SD}$  and  $V_{BG}$  at different temperatures: (a)  $T = 8$  mK, (b)  $T = 1$  K, and (c)  $T = 4.4$  K. The white dashed lines in these figures mark the onset of quasiparticle tunneling at  $V_{SD} \approx 1.4$  meV.

## Magnetic field dependence

Figure C.2 shows  $G$  measured as a function of  $B$  and  $V_{SD}$  at  $T = 20$  mK. The resonance at  $V_{SD} = 0$  V corresponds to the supercurrent due to Cooper pair tunneling across the junction. The resonances at finite bias voltages are ascribed to the MAR features. In Fig. C.2(a), the positions of these MAR features remain roughly constant in  $B$ . We note that in this figure, we observe an enhancement of the supercurrent with increasing  $B$  from 0 T to 2 T. In Fig. C.2(b), the MAR resonance at  $V_{SD} \sim 0.5$  mV starts to shift to a lower bias voltage at  $B \sim 6$  T. This result suggests that the critical field of the superconducting MoSi is most likely above 8 T, i.e.,  $B_C > 8$  T at  $T = 20$  mK.

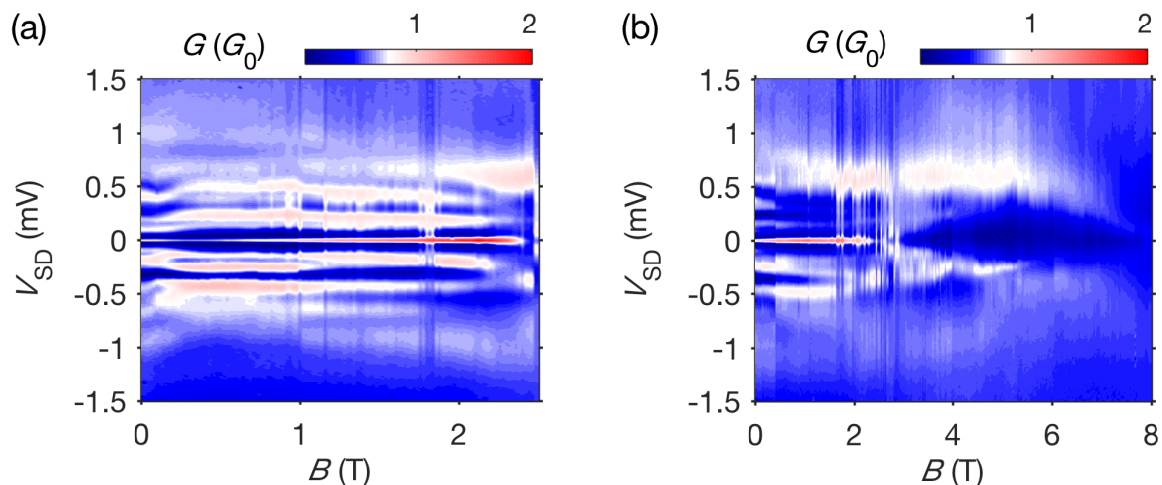


**Figure C.2.**  $G$  measured as a function of  $B$  and  $V_{SD}$  at  $T = 20$  mK. (a)  $B$  is swept from 0 T to 2 T. (b)  $B$  is swept from 0 T to 8 T.

## Local and nonlocal measurements

The device discussed here has a structure similar to the one shown in Fig. 6.1. Here, the measurement is performed by applying a voltage bias,  $V_{SD}$ , to the contact 2, and measuring  $G$  at the contact 3. The corresponding result is shown in Fig. C.3(a). The voltage drop,  $V_{JJ}$ , across the contacts 4 and 5 is measured simultaneously, and the resulting plot is shown in Fig. C.3(b). We note that we keep the contact 6 grounded, and for this device, the contact 1 is broken. Figure. C.3 shows that while driving the local junction (contact 2 and 3), a voltage drop,  $V_{JJ}$ , across the nonlocal junction (contact 4 and 5) appears and oscillates in bias from a positive value to a negative value. The magnetic field dependence of  $V_{JJ}$ , which is shown in Fig. C.3(b), reveals a similar behavior to that of the resonances shown in Fig. C.3(a). We make an initial attempt to interpret our results by assuming that the Josephson radiation emitted by the local junction (contact 2 and 3) can be absorbed by the resonator formed in the superconducting leads of the nonlocal junction (contact 4 and 5) and subsequently can drive this nonlocal junction.

## Three-terminal measurements

We now turn to the three-terminal measurement, where voltage biases  $V_1$  and  $V_2$  are applied to the contacts 2 and 4, respectively, and the differential conductance  $G_1$  and  $G_2$  are simultaneously measured. For this measurement, the contact 3 is kept grounded. Such a measurement is performed to measure the nonlocal supercurrent of quartets as reported in Ref.[218]. In Fig. C.4, we observe horizontal and vertical resonances, and some interesting features with broad resonances appearing at certain bias window. We don't have an interpretation for these observations.

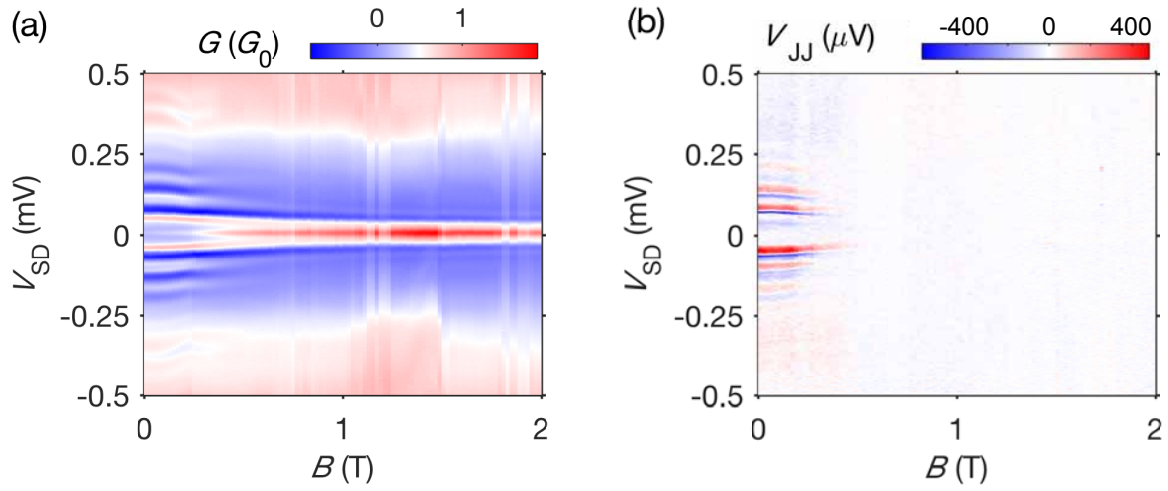


**Figure C.3.** (a) Local measurement of  $G$  as a function of  $V_{SD}$  and  $B$  at  $V_{BG} = -29.5$  V and  $T = 20$  mK. (b) Nonlocal measurement of  $V_{JJ}$  as a function of  $V_{SD}$  and  $B$ .

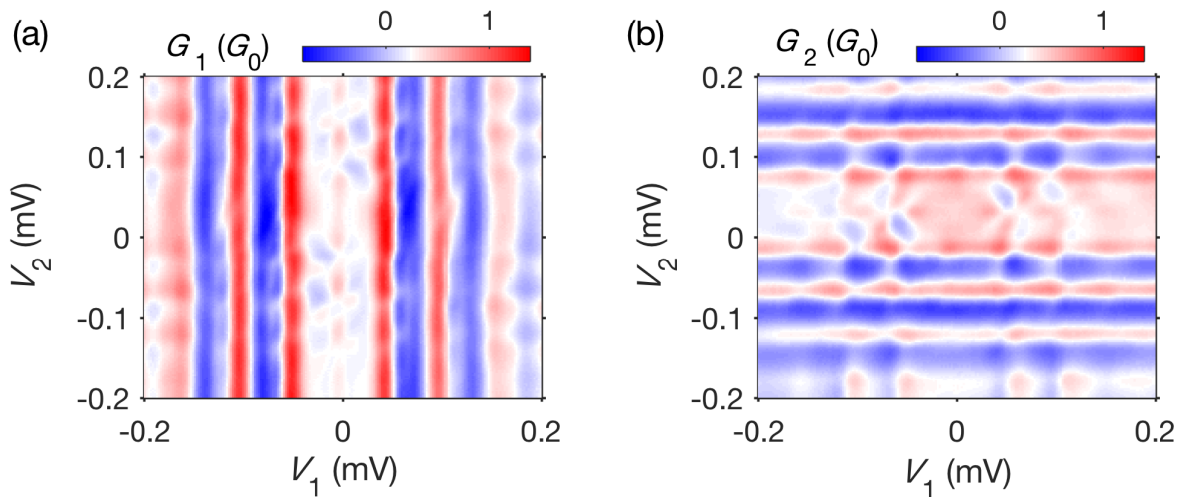


**Figure C.4.** Differential conductance (a)  $G_1$  and (b)  $G_2$  versus  $V_1$  and  $V_2$  at  $V_{BG} = -5$  V and  $T = 20$  mK.



# Curriculum Vitae

Gulibusitan Abulizi

Born on 18 September 1986 in Aksu (China)

## Education

- 2013–2017      **Doctor of Philosophy in Experimental Physics at University of Basel**
- PhD thesis in the group of Prof. C. Schönberger  
“Quantum transport in hexagonal boron nitride-carbon nanotube heterostructures”
- 2011–2013      **Master of Science in Nanotechnology at University of Twente**
- Master thesis in the group of Prof. Wilfred G. van der Wiel  
“Coherent electron transport through molecular bridges”
  - Internship in the group of Prof. İsmet İnönü Kaya (Sabanci University, Turkey) and Prof. Wilfred G. van der Wiel  
“Fabrication of suspended graphene nanoelectronic devices”
- 2010–2011      **Master of Science in Materials Science and Engineering at King Abdullah University of Science and Technology**
- Internship in the group of Prof. Ryan O’Hayre (Colorado School of Mines, United States) and Prof. Iman Roqan  
“Design and fabrication of solid-state ionic field effect transistors”
- 2006–2010      **Bachelor of Engineering in Poly-materials and Engineering at South China University of Technology**
- Bachelor thesis in the group of Prof. Jianqin Zhao  
“Flexible PPO cable materials”
  - Project work in the group of Prof. Yingjun Wang  
“Self-assembly construction of biological activity of scaffolds for cartilage tissue engineering”
  - Minor in Finance
- 2002–2006      **Shenzhen Songgang Middle School**

## Professional Activities

- 4/2018–present     *Postdoctoral researcher at University of Basel, Switzerland*
- 8/2016–present     *Ad hoc reviewer, Physica Status Solidi B: Basic Solid State Physics*
- 2/2014–present     *Teaching assistant for physics at University of Basel, Switzerland*
- 9/2012–1/2013     *Research intern at Sabanci University, Turkey*
- 7/2011–9/2011     *Visiting scholar at Colorado School of Mines, United States*
- 9/2009–4/2010     *Research intern at South China University of Technology, China*

## Scholarships and Awards

- 2015–2016     *Nano image award, Swiss Nanoscience Institute*
- 2012     *Erasmus placement scholarship, University of Twente*
- 2011–2012     *University scholarship, University of Twente*
- 2010     *Fellowship, King Abdullah University of Science and Technology*
- 2007–2009     *Scholarship for top student, South China University of Technology*
- 2007     *National scholarship, Ministry of Education of China*

# Publications

## Publications

- **Full characterization of a carbon nanotube parallel double quantum dot**  
G. Abulizi, A. Baumgartner, and C. Schönenberger, *Physica Status Solidi B* **253**, 2428 (2016).
- **Geometric reduction of dynamical nonlocality in nanoscale quantum circuits**  
E. Strambini\*, K. S. Makarenko\*, G. Abulizi, M. P. de Jong, and W. G. van der Wiel, *Nature Scientific Reports* **6**, 18827 (2016).
- **Carbon nanotube quantum dots on hexagonal boron nitride**  
A. Baumgartner, G. Abulizi, K. Watanabe, T. Taniguchi, J. Gramich, and C. Schönenberger, *Applied Physics Letters* **105**, 023111 (2014).
- **Large-field supercurrents through hexagonal boron nitride encapsulated carbon nanotube quantum dots with zero-dimensional contacts**  
G. Abulizi, A. Baumgartner, K. Watanabe, T. Taniguchi, and C. Schönenberger, in preparation.

\* Equal contribution

## Talks

- *Carbon nanotube quantum dots on hexagonal boron nitride*  
Talk at the 9<sup>th</sup> International Nanoscience Student Conference, Basel, Switzerland, 12 August 2015.
- *Zero-dimensional side contacts to hBN encapsulated carbon nanotubes*  
Talk at the Mesoscopic Transport and Quantum Conference 2017, Espoo, Finland, 07 August 2017.
- *Carbon nanotube-boron nitride heterostructures*  
Talk at the Research Seminar Quantum Science and Technologies HS2017, Basel, Switzerland, 21 November 2017.

## Poster Contributions

- *Electron transport in carbon nanotube devices with engineered tunnel barriers and superconductor/normal metal contacts*  
G. Abulizi, J. Gramich, A. Baumgartner, and C. Schönenberger  
Poster at the Swiss NanoConvention, Basel, Switzerland, 30 June 2016.
- *Hexagonal boron nitride as tunnel barrier, clean substrate, and gate insulator*  
G. Abulizi, A. Baumgartner, S. Caneva, S. Hofmann, K. Watanabe, T. Taniguchi, and C. Schönenberger  
Poster at the International Winterschool on Electronic Properties of Novel Materials, Kirchberg, Austria, 15 February 2016.
- *Quantum transport experiments in carbon nanotubes and semiconducting nanowires*  
G. Abulizi, A. Baumgartner, S. Caneva, S. Hofmann, K. Watanabe, T. Taniguchi, C. Jünger, S. Baba, J. Nygård, S. Tarucha, and C. Schönenberger  
Poster at the 6<sup>th</sup> NCCR QSIT General Meeting, Arosa, Switzerland, 3 February 2016.
- *Carbon nanotube quantum dots noise measurements and boron nitride substrate*  
G. Abulizi, A. Baumgartner, K. Watanabe, T. Taniguchi, J. Gramich, T. Hasler, M. C. Harabula, V. Ranjan, M. Jung, and C. Schönenberger  
Poster at the 5<sup>th</sup> NCCR QSIT Winter School, Arosa, Switzerland, 5 January 2015.
- *Carbon nanotube quantum dots on hexagonal boron nitride*  
G. Abulizi, A. Baumgartner, K. Watanabe, T. Taniguchi, J. Gramich, and C. Schönenberger  
Poster at the conference “Condensed Matter in Paris 2014”, Paris, France, 25 August 2014.



# Acknowledgements

There are many people who have been very helpful and supportive throughout my PhD in Quantum- and Nanoelectronics Group at University of Basel. I am grateful to meet so many outstanding scientists, colleagues, and friends here in Basel and at scientific conferences. I cannot possibly acknowledge them all, but I still would like to express my sincere appreciation to them in this section.

Firstly, I would like to express my deepest gratitude towards my thesis advisor Prof. Christian Schönenberger for offering me this great opportunity to work on exciting scientific projects as a member of his research group. His endless energy and enthusiasm for nanoscale science, his full commitment to various research projects with excellent scientific minds, his sharp sense of observation and troubleshooting skills, and his openness to new ideas and appreciation for his students' efforts, have inspired me to remain engaged and motivated to overcome challenges and obstacles in our research. I sincerely appreciate the given freedom to explore and develop new ideas in “block course” projects. It has been a real pleasure to be a part of his research team.

I also would like to thank Prof. Kasper Grove-Rasmussen and Dr. Carola Meyer for joining the defense committee. I sincerely appreciate for your effort to read this thesis and attend my defense.

Secondly, I am truly grateful to Dr. Andreas Baumgartner for his constant supervision and guidance throughout this PhD project. I would like to thank him for sharing his knowledge and experience in nanofabrication and low-temperature transport experiments on a day-to-day basis. I greatly appreciate his huge support in the laboratory, and his time for many fruitful discussions. I sincerely appreciate his enthusiasm for new findings, his openness to my comments and research questions, and his willingness to give me useful advice on practical skills needed for presenting our research in scientific writing, posters, and talks.

I would like to acknowledge Andreas Baumgartner, Gergő Fülöp, Raphaëlle Delagrè, Frederick Thomas, and Arunav Bordoloi for proofreading (parts of) this thesis and their valuable comments and suggestions. I also would like to acknowledge our collaborators for their tremendous support and effort. Sabina Caneva, Ruizhi Wang, and Prof. Stephan Hofmann from University of Cambridge constantly provided us with monolayer hexagonal boron nitride with excellent quality. Natascha Hedrich, Brendan Shields, and Prof. Patrick Maletinsky from Quantum-sensing Lab carried out scanning-probe measurements on carbon nanotubes.

Next, I am grateful to Thomas Hasler for introducing me to the carbon nanotube stamping technique. I also would like to thank Simon Zihlmann, Kishan Thodkar, and Wangyang Fu for sharing their knowledge and expertise in hexagonal boron nitride transferring techniques. A special thanks goes to Thilo Glatzel from Nanolino Lab for letting us carry out the transfer process in their glove box. It was a pleasure

to supervise Noemí Contreras Pereda's bachelor thesis project on suspended carbon nanotube devices. The work done together with Clemens Spinnler, Claudio Alter, and Marco Zutter during my supervision of the block course project boosted my motivation and creativity to develop zero-dimensional side contacts to hexagonal boron nitride encapsulated carbon nanotubes.

I am very thankful to all current and former members of the Quantum- and Nanoelectronics Group for their countless technical support and fruitful scientific discussions. I mention them here: Anton Vladyka, Arunav Bordoloi, Christian Jünger, Clevin Handschin, Cornelia Nef, David Indolese, Jan Overbeck, Jens Schindele, Jörg Gramich, Julia Samm, Lujun Wang, Maria El Abbassi, Masoud Baghernejad, Mathias Wipf, Matthias Bräuninger, Michel Calame, Mihai-Cezar Harabula, Minkyung Jung, Gabor Fabian, Oliver Braun, Péter Makk, Peter Rickhaus, Ralph Stoop, Roy Haller, Samuel d'Hollosy, Stefan Nau, Toni Fröhlich, and Vishal Ranjan. I am glad to take part in so many adventure type group excursions with them. Learning how to ski in Arosa, climbing via Ferrate to the Tierberglühütte, and canoeing from Mühlau via Bremgarten to Sulz and camping overnight, are among the most amazing and beautiful experiences and memories in my life.

I also would like to thank Barbara Kammermann and Astrid Kalt for taking care of all administrative issues, Dominik Sifrig for constantly providing us liquid helium and nitrogen, Daniel Sacker for taking care of the carbon nanotube growth setup for us, Heinz Breitenstein for supplying the whole group with pressurized helium and nitrogen gas bottles, and Peter Reimann for refilling the chromium target for us. I sincerely appreciate your excellent and professional services, which made this work possible.

Last but not the least, I am deeply grateful for the love and support of my family: Abliz Yüsüf, Gülayım Memitimin, Gülistan Abliz, and Anargül Abliz. On a personal note, I would like to dedicate this thesis to my family.